Large Scale Lattice-Boltzmann Simulations

Computational Methods and Applications

ACADEMISCH PROEFSCHRIFT

ter verkrijging van de graad van doctor
aan de Universiteit van Amsterdam
op gezag van de Rector Magnificus
prof.dr J. J. M. Franse
ten overstaan van een door het college voor promoties ingestelde
commissie, in het openbaar te verdedigen in de Aula der Universiteit
op donderdag 16 december 1999, te 13.00 uur

door

Bhagwatpersad Drona Kandhai

geboren te Paramaribo (Suriname)

Promotor: prof. dr P.M.A. Sloot (Universiteit van Amsterdam)

Co-Promotor: dr. ir A.G. Hoekstra (Universiteit van Amsterdam)

Commissie: prof. dr D. Frenkel (Universiteit van Amsterdam)
prof. dr P. Iedema (Universiteit van Amsterdam)
dr B. Chopard (University of Geneva)
prof. dr P. Hemker (Universiteit van Amsterdam)
prof. dr ir H. Bal (Vrije Universiteit Amsterdam)

Faculteit: Wiskunde, Informatica, Natuurkunde en Sterrenkunde

The work that is described in this thesis was financially supported by:

- Universiteit van Amsterdam
- Nederlandse organisatie voor Wetenschappelijk Onderzoek (NWO), under the Massively Parallel Computing program (Portable Parallel Simulation of Crystal Nucleation and Growth project)
- Los Alamos National Laboratory (LANL)
- Power Computing & Communications UvA B.V.

ISBN 9057760371

Printed at PrintPartners Ipskamp, Enschede, The Netherlands

Voor mijn ouders

Contents

Part I

Introduction

Chapter 1

Computer simulations in fluid dynamics

1.1 Fluid dynamics

A wide variety of applications stemming from the natural sciences and engineering are strongly related with the motion of fluids. Some typical examples are, the atmospheric circulation processes, flow of blood through complex capillary vessels, ground water pollution, compressible flow around an airfoil, and numerous other interesting problems which are of great relevance for the industrial and academic community [1, 2, 3, 4, 5]. A good understanding of the dynamics of fluids is therefore extremely useful in improving several industrial processes and designs, e.g. the wing of an airplane, and may contribute significantly to our knowledge of many fundamental scientific problems, e.g. the impact of hydrodynamics on the morphology of biological growth forms [6].
Although the basic equations for describing the motion of fluids, the so-called Navier-Stokes equations, are known since 1823 [3, 7] a general solution to flow phenomena does still not exist. The extreme complex flow-patterns that may arise are poorly understood. Moreover, a generic approach is hampered by the fact that the equations are often hard to solve [3, 7]. Fluid dynamics is therefore commonly studied by different research areas from their own perspectives and within well-defined restrictions, e.g. incompressible versus compressible flow, creeping versus turbulent flow, single- versus multi-phase flow, Newtonian versus non-Newtonian flow.
A review of the history of fluid dynamics clearly shows that the following approaches are commonly taken in studying these phenomena:

- Experimental measurements.

For many physical systems, it is known that experimental observations elucidate much of their complexities. A well known example in fluid dynamics, is the behavior of fluid flow around a circular cylinder. For increasing Reynolds number * the flow patterns are gradually changing from purely laminar and sym-

*The Reynolds number, Re, is defined as the ratio, $\frac{LV}{\nu}$, where L and V are characteristic length metric flow to the formation of wakes behind the cylinder and symmetry breaking. After some critical value of the Reynolds number the flow becomes fully turbulent [4, 5, 7]. Similar behavior is observed in flow along a channel. For small Reynolds numbers the velocity profile is known to be parabolic (Poiseuille flow). As the Reynolds number is increased, the velocity profile flattens and the flow becomes fully turbulent beyond some critical Reynolds number [4, 5]. Experiments have indeed contributed significantly to our understanding and knowledge of flow phenomena. Also many relations which are regularly used in engineering applications, for example the drag coefficients for a sphere as a function of the Reynolds number, have been obtained from experimental data [5]. However, the observations are in general only valid for a specific experimental configuration and the experiments may be quite sophisticated and expensive to perform in the case of complex flow applications. Moreover, some phenomena can not be easily observed on the laboratory scale due to the different space and time scales that are present in the dynamics;

- Theoretical methods.

Simplified closure models of the governing equations for a particular flow regime are solved by mathematical methods under the assumption of strict boundary and initial conditions [3]. In principle this approach is preferred because it gives us at least the *hope* to find a somewhat general solution for a class of flow problems. Unfortunately theoreticians have not been able to solve the general behavior of even one of the 'simplest' flow problems, namely flow around a spherical obstacle. In the limit of low Reynolds numbers, the so-called creeping flow regime or Stokes flow, an analytical solution is known to exist, but for moderate to high Reynolds numbers there is no analytical solution known so far [3, 4, 7]. Even low Reynolds number flow in non-trivial geometries is hard to solve by theoretical methods, e.g. fluid flow in a disordered array of cylinders. In general, fluid flow problems are hard to solve analytically due to the nonlinearity of the macroscopic equations and the nature of the (complex) flow boundaries;

- Numerical simulations.

An alternative approach to get insight in flow phenomena is by means of numerical simulations, a research field known as computational fluid dynamics (CFD) [8, 9]. One of the famous examples of this approach is weather forecasting and climate modeling. The objective here is to predict the future state of the atmosphere from knowledge of its present state. In 1922 L.F. Richardson showed that the macroscopic equations for describing the atmospheric circulation processes can be approximated by a set of algebraic difference equations at a finite number of points in space [10, 11]. In CFD this process is known as the discretization of a continuum model. At that time high speed computers were not available and Richardson estimated that a work force of 64.000 people would be required to describe in real time the weather on a global basis. He

and velocity scales and ν is the kinematic viscosity of the fluid. For an incompressible flow in a given geometrical shape of the boundaries, the Reynolds number is the only control parameter.

performed an example forecast by hand using two grid points, but the results were very discouraging. After this failure, numerical prediction was not again attempted for many years. Later, the development of digital computers after the World War II, made the enormous computation power required in a numerical forecast feasible. But due to numerical instability there were still problems with Richardson's equations [11]. Around 1950 J.F. Charney simplified the dynamical equations using several assumptions and derived the so-called quasi-geostrophic model [11]. This model was used to perform the first numerical forecast. Nowadays, with the development of more powerful computers and more sophisticated modeling techniques it is possible to simulate models which are quite similar to Richardson formulation.
The last example clearly illustrates that the success of numerical simulations depends on refinements on the level of the *physical model*, the *numerical schemes* and the available *computational resources*. More specifically stated, in the physical model the different processes are commonly represented by macroscopic equations in which many phenomena are ignored. The numerical schemes have a finite accuracy and are often conditionally stable. And finally the resolution of the grids depends on the available computational resources. Numerical simulations as an intermediate approach for studying fluid dynamics can be useful for problems which are intractable by theoretical methods and are difficult, dangerous and expensive to be observed in real experiments. Also some studies focus on a forecast of a phenomenon and must be performed before the real physical processes actually take place. However, a numerical simulation is only an approximation of a simplified model of the real phenomena and it should be emphasized that the simulation results must be interpreted with extreme care. It is therefore very important to rigorously validate the simulations by a thorough comparison with analytically tractable problems and experimental measurements.
In summary, theoretical and experimental approaches may be extremely valuable as a validation of numerical simulations. Moreover, numerical simulations can be used to some extend, to develop new theory and to replace some experiments which are tedious, expensive or even impossible to mimic at the laboratory scale. It is thus evident that all methods have their own favorable approaches and also their limitations.
In this thesis we focus on numerical simulations of fluid flows. We study an alternative computational approach in fluid dynamics that is based on kinetic theory. In the next section, we first briefly discuss the traditional approach that is still widely used in CFD. Then we introduce the main ideas of the mesoscopic particle based models that we use and finally we motivate the outline of the research described in this thesis.

1.2 Computational fluid dynamics

In this thesis we restrict ourselves to single component/phase, incompressible, isothermal and Newtonian fluid flows. Although this is a major simplification of the general formulation of hydrodynamics, there are still many realistic applications in this flow regime and the nature of these flows may also be extremely complicated. Traditionally, the macroscopic behavior of fluid flow is modeled by means of the Navier-Stokes equations [1, 2, 3, 4, 5]. The main assumption is that at a macroscopic scale, the behavior of fluid motion is not directly influenced by the detailed molecular interactions, but depends on the average motion of many microscopic particles, the so-called continuum limit assumption. Fluid motion can therefore be described by average physical quantities like velocity, pressure, temperature and density. The flow of an incompressible fluid in a given geometry can be described by the classical Navier-Stokes equations [1, 2, 3, 4, 5]

$$\nabla \cdot \mathbf{v} = 0 \tag{1.1}$$

$$\frac{\partial \mathbf{v}}{\partial t} + (\mathbf{v} \cdot \nabla)\mathbf{v} = -\frac{1}{\rho}\nabla p + \nu \nabla^2 \mathbf{v} + \mathbf{f}, \tag{1.2}$$

where ρ is the fluid density, $\mathbf{v}$ is the velocity, p is the pressure, ν is the kinematic viscosity and $\mathbf{f}$ is a body force, e.g. the gravity force. The velocity and the pressure are functions of space and time. Eq. 1.1 expresses the conservation of mass. It states that the in- and outflow of mass in a fluid element are balanced. Eq. 1.2 is the Navier-Stokes equation for incompressible fluids which expresses the conservation of momentum. This equation describes the velocity changes in time, due to convection $(\mathbf{v} \cdot \nabla)\mathbf{v}$, spatial variations in pressure ∇p, and viscous forces $\nu \nabla^2 \mathbf{v}$.

The next step in CFD is to discretize the continuum equations. There are many ways to accomplish this goal, namely by means of finite-difference, finite-volume, finite-element or spectral methods. Each of these strategies have their own philosophy for obtaining a set of discrete algebraic equations (more details can be found in e.g. Ref [8]). Finally, the evolution of the flow field is computed by solving the discrete equations constrained by well-defined initial and boundary conditions via an appropriate numerical algorithm. It is important to notice that the different schemes mentioned above, have a number of aspects in common, namely

- spatial dependence. Most simulations are performed on a grid or mesh. To update a certain nodal point information of neighboring points is required;
- temporal dependence. To evolve the flow variables in time, the results may be needed of the current and previous time step(s) (explicit schemes) and in some methods also information of the future state (implicit schemes);
- convergence. As the resolution of the grid or mesh is refined, it is expected that the discrete approximation should converge to the continuum equations.

From this brief description, it is obvious that the traditional approaches in CFD contain the following steps:

- First, the macroscopic balance equations are derived (physical modeling phase);
- Next, the continuum equations and the flow geometry are discretized and a numerical scheme is chosen to solve the discrete model (numerical approximation phase)
- And finally the actual implementation and execution on a computational platform (sometimes including code parallelization) is performed (mapping phase).

One major objection of the traditional CFD approach is that the physical modeling, the numerical approximation and the mapping phases are often completely separate steps. As a consequence this approach may have some drawbacks regarding for example the flexibility to deal with arbitrary geometries, complex flows and code parallelization. In the next section we introduce the basic concepts of a particle based model as an alternative tool for CFD. In this model the physical modeling and the numerical approximation phases are combined. The intuitive microscopic view of fluid flow, *c.f.* particles are moving and interacting, is still present in this model. As a result it possesses some unique advantages, e.g. flexibility to deal with complex boundary conditions, it can be extended relatively easy to deal with complex flows in some cases and it preserves the spatial and temporal locality and thus is ideal for parallel processing. Some of these nice features will become clear in the remainder of this thesis.

1.3 Lattice Gas hydrodynamics

> *"We have noticed in nature that the behavior of a fluid depends very little on the nature of the individual particles in that fluid. For example, the flow of sand is very similar to the flow of water or the flow of a pile of ball bearings. We have therefore taken advantage of this fact to invent a type of imaginary particle that is especially simple for us to simulate. This particle is a perfect ball bearing that can move at a single speed in one of six directions. The flow of these particles on a large enough scale is very similar to the flow of natural fluids"*, Richard Feynman (Quoted by Rothman and Zaleski in Ref. [12]).

More then 10 years ago, a complete different strategy of modeling fluid dynamics has been proposed, based on cellular automata principles [13]. The main idea of these so called Lattice Gas Automata (LGA) is that fluid flow can be characterized by the average motion of particles on a regular lattice. A nice introduction about LGA is given by Rothman and Zaleski in their recently published book[12].
"In 1986, Uriel Frisch, Brosl Hasslacher, and Yves Pomeau announced a striking discovery. They showed that the molecular, or atomistic, motion within fluids - an extraordinarily complicated affair involving on the order of 10^{24} *real-valued*

degrees of freedom - need not be nearly so detailed as real molecular dynamics in order to give rise to realistic fluid dynamics. Instead, a fluid may be constructed from fictitious particles, each with the same mass and moving with the same speed, and differing only in their velocities. Moreover, the velocities themselves are restricted to a finite set."

The main difference between LGA and the traditional numerical approaches is that in LGA the physical evolution rules are discrete while in the latter the discretization is performed on the level of the macroscopic flow equations. In both cases however, the same physical conservation laws are valid.
Lattice Gases can be viewed as mesoscopic models which occupy a position between the full molecular dynamics and macroscopic descriptions by means of partial differential equations. Basically, particles move synchronously along the bonds of a lattice (propagation step) and interact locally, constraint to conservation of mass and momentum (collision phase). This update mechanism is illustrated in Figure 1.1.
The first LGA was the so-called HPP model on a square lattice [14, 15]. The main problem with this model is that the hydrodynamic behavior is not isotropic and the method satisfies some unphysical conservation laws, the so-called spurious invariants. Later, it was realized that the connectivity of the lattice is the main reason for these unphysical effects and in a next development, the so-called FHP model (see Figure 1.1) based on a hexagonal lattice, these problems were eliminated.

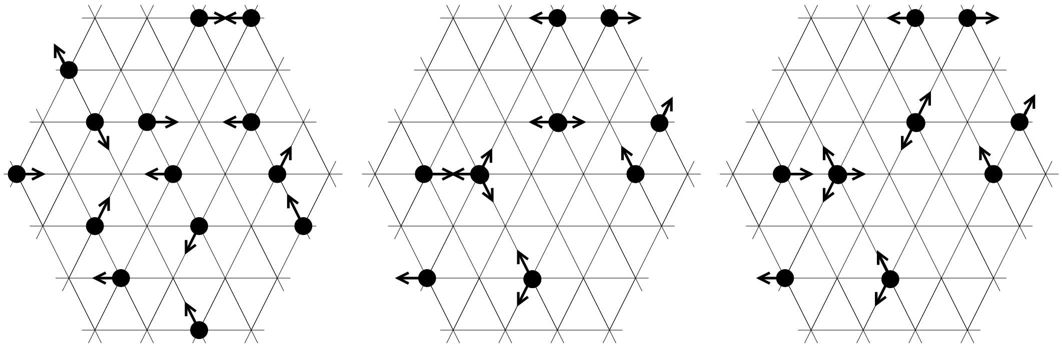

(a) initial lattice (b) streaming (c) collision handling

Figure 1.1: Update mechanism of a FHP LGA. Arrows denote a particle and its moving direction. In Figures a to c the propagation (streaming) and collision phases are shown for some initial configuration.

The FHP model evolves according to the following dynamical rule,

$$n_i(\mathbf{x}+\mathbf{c}_i, t+1) = n_i(\mathbf{x}, t) + \omega_i(\mathbf{n}(\mathbf{x}, t)) \qquad i = 1\ldots 6 \tag{1.3}$$

where $n_i(\mathbf{x}, t)$ is a boolean variable representing the presence/absence of a particle with velocity $\mathbf{c}_i$ (unity in the FHP model) at site $\mathbf{x}$ at time t and $\omega_i(\mathbf{n}(\mathbf{x}, t))$

is the output state of the collision operator along link i (the input state is denoted by $\mathbf{n}(\mathbf{x},t)$). An example of the collision operator that is used in Figure 1.1 is shown in figure 1.2. Notice that in the collision operator only those configu-

Figure 1.2: Collision rules of the FHP LGA. Arrows denote a particle and its moving direction. When multiple post collision states are possible a random selection is made. The collision rules satisfy mass and momentum conservation.

rations are allowed that satisfy conservation of mass and momentum. For instance, when two particles enter the same site with opposite velocities, both of them are deflected by 60 degrees such that the net momentum in the post collision state remains zero and when multiple post collision states are possible a random selection is made. It can be demonstrated that these microscopic rules simulate the following macroscopic equations [12, 16],

$$\frac{\partial \mathbf{v}}{\partial t} = -(g(\rho)\mathbf{v}\cdot\nabla)\mathbf{v} - \frac{1}{\rho}\nabla p + \nu\nabla^2\mathbf{v} \tag{1.4}$$

where ρ is the average number of particles per cell and $g(\rho)$ is a function of ρ. For the FHP model $g(\rho) = \frac{\rho-3}{\rho-6}$ [16]. Eq. 1.4 is clearly similar to the Navier-Stokes equations for incompressible fluids, except for the fact that there is a $g(\rho)$ function in front of the convection term. This artifact is known as non-Galilean invariance[†] of LGA. Also in LGA, the density and the velocity are coupled. More specifically stated, flow domains with constant pressure p and a relatively high velocity $\mathbf{v}$ have a higher density ρ than regions with a lower velocity. This is not consistent with the physical behavior of incompressible fluids in which generally very small density fluctuations are present. However, for low velocities or low Mach numbers[‡] $g(\rho)$ can be assumed constant and in Eq. 1.4 the time t, the viscosity ν, and the pressure p can be renormalized $(t' = g(\rho)t, \nu' = \frac{\nu}{g(\rho)}, p' = \frac{p}{g(\rho)})$ and the Navier-Stokes equation for incompressible fluids can be recovered.
In summary, a lattice gas automaton is a mesoscopic method for simulation of fluid flow at a macroscopic scale, based on the following observations:

- the macro-dynamics of a fluid is a result of the collective behavior of many particles in the system and details of the microscopic interactions are not essential;

[†] A system is Galilean invariant if the equations do not change when it is observed from a frame of reference that is moving with a constant velocity

[‡] The Mach number, is defined as the ratio, $\frac{V}{C_s}$, with V the characteristic velocity and C_s the speed of sound.

- changes in molecular interactions affect transport properties such as viscosity, but they do not alter the basic form of the macroscopic equations as long as the basic conservation laws and necessary symmetries are satisfied.

As a consequence of this mesoscopic particle based approach and the inherent spatial and temporal locality, the lattice gas approach possesses some unique advantages with respect to standard numerical methods:

- boundary conditions are easy to implement and the method is especially suitable for simulating fluid flow in complex geometries;
- the model is ideal for massively parallel computing because the updating of a node involves only its nearest neighbors;
- the code is extremely simple compared to that of state-of-the-art numerical methods;
- hydrodynamics is modeled in a very intuitive way and in some flow regimes, the method can be easily extended to simulate complex fluids, e.g. multi-component fluids.

1.4 Research motivation and outline

In the previous sections, we described the relevance of hydrodynamics and the different approaches that are regularly used in this field to solve the related problems. The computational fluid dynamics approach is discussed in some more detail. We discussed the basic idea of the traditional numerical modeling strategies in CFD and also introduced the main philosophy of the particle based LGA as an alternative approach in CFD.

> *The general interest of our research group is in making phenomena from nature tractable for simulation using state-of-the-art parallel processing technology.*

In this thesis we consider the potentials for particle based models in CFD. We study the successor of the LGA, the so-called Lattice-Boltzmann models (see chapter 2). Special interest for particle based models is mainly due to the intrinsic locality of their update rules which makes them suitable for efficient simulation on high performance computers. Moreover, a mesoscopic approach to model the macroscopic physics is attractive, because the physics is modeled in an intuitive and natural way.
We approach our research from three different perspectives. Before motivating why in our opinion this approach might be fruitful we first present the different perspectives:

- *Numerical modeling*

Experts in numerical simulations are often interested in new models to effectively study for instance physical systems. The LGA and its successor, the Lattice-Boltzmann method, are relatively new methods for studying fluid dynamics by means of computer simulations. However, these models are based on basic principles of kinetic theory and therefore have a complete different development compared to the standard approaches used by numerical mathematicians and engineers.
Although many promising simulations have been performed based on LGA ideas, examples of its use to simulate realistic applications which are of industrial relevance are still very limited. One of the reasons for this is that due to the simplicity of the method, researchers are often not convinced by its effectiveness in studying complex flow problems. Moreover, as illustrated in the previous sections, LGA models are different from traditional numerical approaches because the physical model and its numerical approximation (including the discretization process) are combined in one cycle. Its understanding and application thus requires knowledge of kinetic theory and fluid dynamics. Finally, LBM simulations have been often used to simulate complex flow behavior at a qualitative level and not many detailed, and thus convincing, validations with experiments and traditional CFD simulations have been published.
In this thesis, we report on rigorous and original studies of lattice-Boltzmann simulations concerning flow in complex geometries and we compare our results in detail with experimental data and other numerical models (see chapter 6). The objective is to get insight in the performance of these particle based models for simulating flow in complex geometries from both a computational point of view and by taking into account the accuracy of the simulation results.
Moreover, we address various important computational aspects that have appeared to be serious shortcomings of LBM. More specifically stated, in chapter 3 we present comparative studies of several boundary conditions and regularly used 3D models. A new technique, to reduce the number of time-steps that are required in lattice-Boltzmann simulations to reach a steady state, is discussed in chapter 4. Extensions of the standard lattice-Boltzmann algorithm from uniform to nested grids are presented in addendum A;

- *Computer Science*

From a computer science perspective we are interested in novel models for large scale complex simulations, that are ideal for execution on the current state-of-the-art high performance machines. We look for models that have intrinsic locality in their update mechanisms. A promising idea in this respect is indeed the philosophy of LGA, that is to allow only nearest neighbor interaction in space and to use explicit time update schemes. Although LGA and LBM models have been claimed to be easy for parallelization, efficient and generic load balancing has not been reported to the best of our knowledge. One obvious reason for this is that in most implementations of LGA and LBM algorithms, the parallelization effort is kept as simple as possible. In chapter 5 we discuss efficient and generic parallelization of lattice-Boltzmann simulations;

- *Physics*

Besides a thorough validation of the lattice-Boltzmann simulation results, we are, from a physics point of view, interested in the hydrodynamic properties of fibrous media. We first study the behavior of the hydraulic permeability as a function of the fiber volume fraction for many ordered and disordered models of fibrous media for a large range of fiber volume fractions and compare our results rigorously with existing theoretical, numerical and experimental data. Furthermore, the functional behavior of the hydraulic permeability is explored in more detail and correlated with the geometry of the media using simple scaling arguments. Finally, we study the effect of wall boundaries on the hydraulic permeability by simulating fluid flow in fibrous media placed between two parallel plates (the so-called bounded media). Although many realistic fibrous media are bounded there are not many theoretical studies reported on this topic. This is mainly due to singularities introduced by the parallel plates. We consider ordered and disordered media and calculate the hydraulic permeability as a function of the distance between the parallel plates and the fiber volume fraction (see chapter 7).

It is obvious that these different perspectives that are used in this thesis require a combined knowledge of hydrodynamics, numerical modeling and computer science. As it became clear from our example focusing on weather forecasting as an application of CFD, the success of computer simulations of large scale complex problems depends on refinements on these three areas. This combined view is indeed the unique and main objective of *computational science* and we believe that especially due to such a typical 'computational scientists' approach, the potentials of new models similar to ideas of LGA can be further explored and developed.

Chapter 2

Theoretical background

2.1 Lattice-Boltzmann models

In the previous chapter we introduced the basic concepts of lattice gases. The main philosophy is to model fluid dynamics by a particle propagation - and collision process on a regular lattice. Although lattice gases have proven to be very useful for modeling hydrodynamics, one major drawback of the method is the statistical noise in the computed hydrodynamic fields. This shortcoming is a direct consequence of the single particle boolean dynamics. To obtain accurate results for the hydrodynamical fields, averaging over a large number of time steps and/or lattice points are often required and therefore the simulations may be rather inefficient.
It has been shown that a simple modification of the LG idea can reduce the noisy dynamics. In fact, by tracing a density of particles along each bond of the lattice, *cf.* following the motion of an average number of particles, the noise in the results can be eliminated. This is the key idea of the so-called lattice-Boltzmann methods (LBM). However, it must be emphasized that this modification has one major consequence for the simulated physical behavior. In this refinement of the method it is assumed that there are no particle correlations in the system, *cf.* the boolean variables n_i can be considered as independent random variables. This is the so-called Boltzmann molecular chaos assumption from kinetic theory [17]. To further understand this assumption we consider the ensemble average of a part of the two-body collision operator, $< D_i >$. The term D_i is a boolean valued expression that is true when only two particles are entering a lattice point along the bonds i and $i+3$ and otherwise it is false. It is a part of the two body collision rule discussed in the previous chapter (for more details see Ref. [16]). Its ensemble average is defined as,

$$< D_i > = < n_i n_{i+3}(1-n_{i+1})(1-n_{i+2})(1-n_{i+4})(1-n_{i+5}) > .$$

If it is assumed that the particle-particle correlations decay very fast due to the collisions between particles, the molecular chaos assumption is valid. This enables us to evaluate the ensemble averages $< n_k n_l n_m .... >$ in a simple way, and the following equality will hold,

$$< D_i > = < n_i > < n_{i+3} > < 1 - n_{i+1} > < 1 - n_{i+2} > < 1 - n_{i+4} > < 1 - n_{i+5} > .$$

In general, it is very difficult is show whether the molecular chaos assumption is valid. In kinetic theory it is argued that this assumption is reasonable for fluid flow at a macroscopic scale[17]. However, in many applications fluctuations and correlations play an important role, e.g. fluctuating hydrodynamics [18], reaction-diffusion systems [16] and diffusion of colloidal particles in a fluid [19]. In these cases the LGA are definitely more realistic than LBM.
In this chapter, we focus on the macroscopic behavior of the Lattice-Boltzmann models. The objective is to underline the basic physical assumptions and related limitations for modeling fluid flow by means of LBM. The complete derivation is based on Ref. [16]. First, a general equation for the macroscopic behavior of LBM is derived. Next, the different terms in the general equation are connected with the known hydrodynamic properties, e.g. velocity, pressure, speed of sound and viscosity. And finally, we present a brief overview of the development of the LGA and LBM in order to illustrate the latest improvements.

2.2 The general Lattice Boltzmann equation

The lattice-Boltzmann models can be described by the following equation,

$$f_i(\mathbf{r} + \Delta t \mathbf{v}_i, t + \Delta t) = f_i(\mathbf{r}, t) + \Omega_i(\mathbf{r}, t) \tag{2.1}$$

where $f_i(\mathbf{r}, t)$ is the probability of finding a particle with velocity $\mathbf{v}_i$ at position $\mathbf{r}$ and time t, Δt is the time step and $\mathbf{v}_i$ is the velocity along link i. The first term in Eq. 2.1 represents the streaming part and the second term, Ω_i, is the collision operator. The main difference between Eq. 2.1 and the regularly used continuous Boltzmann equation from kinetic theory [20], is the strict discretization of the phase space. In Eq. 2.1 the time and space variables are discrete and in the velocity space only a small number of values are allowed. For the time being we do not specify the exact form of the collision operator, but we state only the main requirements imposed on it, namely:

- conservation of mass, that is $\sum_{i=1}^{n} \Omega_i(\mathbf{r}, t) = 0$ (n is the number of links per lattice point) and
- conservation of momentum, $\sum_{i=1}^{n} \Omega_i(\mathbf{r}, t)\mathbf{v}_i = \mathbf{0}$.

The macroscopic variables, density $\rho(\mathbf{r}, t)$ and velocity $\mathbf{u}(\mathbf{r}, t)$ are defined as moments of the discrete velocity distribution $f_i(\mathbf{r}, t)$ as

$$\rho(\mathbf{r}, t) = \sum_{i=1}^{n} f_i(\mathbf{r}, t)$$

$$\mathbf{u}(\mathbf{r}, t) = \frac{\sum_{i=1}^{n} f_i(\mathbf{r}, t)\mathbf{v}_i}{\rho(\mathbf{r}, t)}$$

As stated in the introduction, our main objective is to derive the macroscopic behavior of Eq. 2.1 in terms of the hydrodynamic fields, ρ and $\mathbf{u}$. To obtain a continuum description we first apply a Taylor expansion to the left hand side of Eq. 2.1 up to second-order in time and space around $(\mathbf{r},t)$,

$$\Delta t\partial_t f_i + \Delta r(\mathbf{c}_i.\nabla)f_i + \frac{\Delta t^2}{2}\partial_t^2 f_i + \frac{\Delta r^2}{2}(\mathbf{c}_i.\nabla)^2 f_i + \Delta r\Delta t(\mathbf{c}_i.\nabla)\partial_t f_i = \Omega_i, \qquad (2.2)$$

where $\partial_x = \frac{\partial}{\partial x}$, Δr is the lattice spacing and the vector $\mathbf{c}_i$ denotes the coordinates of the neighbor along link i. In fact we have assumed here that the distribution f_i is a smooth and sufficiently differentiable function in time and space. This can be justified when the lattice spacing is much bigger than the mean free path* [16]. Notice that the traditional derivation of the Navier-Stokes equations from the basic conservation laws is based on similar arguments (the so-called continuum limit approximation)[3].
To proceed further with the derivation, we apply the Chapman- Enskog expansion [16, 17]. The Chapman-Enskog expansion is commonly used in statistical mechanics to solve the Boltzmann equation. It consists of three basic approximations,

- First the particle distribution function f_i is expanded into terms of different order of magnitude (with ε a small perturbation parameter),

  $$f_i = f_i^0 + \varepsilon f_i^1 + \varepsilon^2 f_i^2 + \ldots$$

  This expansion is analogous to the regularly used perturbation methods for solving differential equations.

- Furthermore, two different time-scales are introduced, the multi-scale expansion, for describing the time evolution of the macroscopic variables. It is known that in hydrodynamic phenomena the main physical processes are the convection of fluid parcels (determined by the local velocity of the fluid) and viscous effects as a results of diffusion of momenta. These two processes take place at different time-scales. Therefore, we expand the time and space variable as follows,

  $$t = \frac{t_1}{\varepsilon} + \frac{t_2}{\varepsilon^2} \qquad \partial t = \varepsilon\partial t_1 + \varepsilon^2\partial t_2$$

  $$\mathbf{r} = \frac{\mathbf{r_1}}{\varepsilon} \qquad \frac{\partial}{\partial r_\alpha} = \varepsilon\partial_{1\alpha},$$

  where α denotes the spatial coordinate (in two-dimensions the x or y coordinate) and t_1 and t_2 are the convective and diffusive time-scale respectively.

- Finally the f_i^l should satisfy the following constraints,

  $$\rho = \sum_{i=1}^{n} f_i^0 \quad \text{and} \quad \rho\mathbf{u} = \sum_{i=1}^{n} f_i^0\mathbf{v}_i$$

*The mean free path is the average distance that molecules travel between collisions and

$$\sum_{i=1}^{n} f_i^l = 0 \quad \text{and} \quad \sum_{i=1}^{n} f_i^l \mathbf{v}_i = \mathbf{0}$$

for $l \geq 1$. These constraints are necessary in order to find a consistent and unique solution for the distribution function f_i. As we will see in the next section, f_i^0 is considered as the equilibrium distribution.

For a more detailed description of the Chapman-Enskog expansion we refer the interested reader to standard text books on kinetic theory [17, 20]. Also, a nice introduction of this technique in the case of the diffusion automaton (a HPP type of model) is discussed in Ref. [16]. This description discusses the necessity for the different approximations in the Chapman-Enskog expansion in more detail. Having introduced the Chapman-Enskog expansion, we can now derive balance equations for different order of the perturbation parameter ε. Notice that to obtain relations for the hydrodynamic fields we need to sum over all the lattice bonds. By applying the Chapman-Enskog expansion to Eq. 2.2, and taking the sum over all links, we can derive the following balance equations for $O(\varepsilon)$,

$$\partial_{t_1}\rho + \partial_{1\alpha}\rho u_\alpha = 0 \tag{2.3}$$

and

$$\partial_{t_1}\rho u_\alpha + \partial_{1\beta}\Pi^{(0)}_{\alpha\beta} = 0 \tag{2.4}$$

where

$$\Pi^{(0)}_{\alpha\beta} = \sum_{i=1}^{n} v_{i\alpha} v_{i\beta} f_i^0(\mathbf{r}, t)$$

and the Einstein summation convention is used implicitly, meaning that repeated indices imply summation over space coordinates, e.g in 2D,

$$c_{i\beta}\partial_{1\beta} = c_{ix}\partial_{1x} + c_{iy}\partial_{1y}.$$

Eq. 2.3 states that the density fluctuations at time-scale t_1 are balanced by the net inflow of mass into a fluid element. And Eq. 2.4 states a similar balance for the momentum. These equations are similar to the Euler equations for inviscid fluid flows [3]. In an analogous way a balance equation can be derived for $O(\varepsilon^2)$,

$$\partial_{t_2}\rho + \frac{\Delta t}{2}\partial^2_{t_1}\rho + \frac{\Delta t}{2}\partial_{1\alpha}\partial_{1\beta}\Pi^{(0)}_{\alpha\beta} + \Delta t\partial_{t_1}\partial_{1\alpha}\rho u_\alpha = 0 \tag{2.5}$$

and

$$\partial_{t_2}\rho u_\alpha + \partial_{1\beta}\Pi^{(1)}_{\alpha\beta} + \frac{\Delta t}{2}\partial^2_{t_1}\rho u_\alpha + \frac{\Delta t}{2}\partial_{1\beta}\partial_{1\gamma}S^{(0)}_{\alpha\beta\gamma} + \Delta t\partial_{t_1}\partial_{1\beta}\Pi^{(0)}_{\alpha\beta} = 0 \tag{2.6}$$

where

$$S^{(0)}_{\alpha\beta\gamma} = \sum_{i=1}^{n} v_{i\alpha} v_{i\beta} v_{i\gamma} f_i^0 \qquad \text{and} \qquad \Pi^{(1)}_{\alpha\beta} = \sum_{i=1}^{n} v_{i\alpha} v_{i\beta} f_i^1.$$

Notice that in these equations we have some terms associated with time scale t_1 that can be further simplified using the balance equations 2.3 and 2.4. By taking the time derivative ∂_{t_1} of Eq. 2.3 the following relation can be derived,

$$\frac{\Delta t}{2}\partial_{t_1}^2\rho = -\frac{\Delta t}{2}\partial_{t_1}\partial_{1\alpha}\rho u_\alpha.$$

Using this expression and Eq. 2.4 it is easy to show that the following relation holds,

$$\frac{\Delta t}{2}\partial_{t_1}^2\rho + \frac{\Delta t}{2}\partial_{1\alpha}\partial_{1\beta}\Pi_{\alpha\beta}^{(0)} + \Delta t\partial_{t_1}\partial_{1\alpha}\rho u_\alpha = \frac{\Delta t}{2}\partial_{1\alpha}[\partial_{t_1}\rho u_\alpha + \partial_{1\beta}\Pi_{\alpha\beta}^{(0)}] = 0.$$

We can now use this property to simplify Eq. 2.5 and obtain the following simple form,

$$\partial_{t_2}\rho = 0.$$

This expression states that at time scale t_2 the density can be assumed to be constant. Thus in fact the density fluctuations are completely determined by the physical process that take place at time scale t_1, namely convection.
Similarly the following relation can be derived by taking the time-derivative ∂_{t_1} of Eq. 2.4,

$$\frac{\Delta t}{2}\partial_{t_1}^2\rho u_\alpha = -\frac{\Delta t}{2}\partial_{t_1}\partial_{1\beta}\Pi_{\alpha\beta}^{(0)}.$$

Using this expression in Eq. 2.6 gives,

$$\partial_{t_2}\rho u_\alpha + \partial_{1\beta}[\Pi_{\alpha\beta}^{(1)} + \frac{\Delta t}{2}(\partial_{t_1}\Pi_{\alpha\beta}^{(0)} + \partial_{1\gamma}S_{\alpha\beta\gamma}^{(0)})] = 0. \tag{2.7}$$

Eq. 2.7 contains the dissipative contribution to the Euler equation. The term, $\Pi_{\alpha\beta}^{(1)}$ is the dissipative part of the momentum tensor. It will be shown later that the second term, $\frac{\Delta t}{2}(\partial_{t_1}\Pi_{\alpha\beta}^{(0)} + \partial_{1\gamma}S_{\alpha\beta\gamma}^{(0)})$, accounts for the discreteness of the lattice. Due to the special form of LBM this term can be included as a correction factor in the kinematic viscosity. This is exactly the reason why the scheme is second-order convergent in space and time while it is based on first-order space and time difference methods (see addendum A). Combining the $O(\varepsilon)$ and $O(\varepsilon^2)$ terms we get the following general equation for the macroscopic description of the Lattice-Boltzmann equation:

$$\partial_t\rho + \nabla.(\rho\mathbf{u}) = 0 \tag{2.8}$$

$$\partial_t\rho u_\alpha + \frac{\partial}{\partial r_\beta}[\Pi_{\alpha\beta} + \frac{\Delta t}{2}(\varepsilon\partial_{t_1}\Pi_{\alpha\beta}^{(0)} + \frac{\partial}{\partial r_\gamma}S_{\alpha\beta\gamma}^{(0)})] = 0 \tag{2.9}$$

In summary, we derived the continuity equation, Eq. 2.8, and the momentum equation, Eq. 2.9, from general constraints for mass and momentum conservation. In fact these macroscopic equations are now expressed in terms of first-order, second-order and third-order tensor relation of the particle distribution function and the lattice velocities. In order to derive the final equations in terms of the velocity and the density (the macroscopic variables) we need to express f_i^0 and f_i^1 as functions of the local velocity and density and evaluate these tensorial functions.

2.3 The Lattice-BGK model

To proceed further with the derivation we need to consider the details of the collision term. In the simulations that will be reported in this thesis we use a special class of LBM, namely the lattice-Boltzmann BGK (Bhatnager, Gross and Krook) methods (LBGK). For simplicity we consider here the derivation of the macroscopic behavior of the so-called D_2Q_8 lattice-BGK model which is based on a two-dimensional square lattice (see Figure 2.1). In this model, $\mathbf{c}_i = (\cos(\frac{2\pi}{8}(i-1)), \sin(\frac{2\pi}{8}(i-1)))$ and the velocity $\mathbf{v}_i = \frac{\Delta x}{\Delta t}\mathbf{c}_i$ for the horizontal and vertical directions, and $\mathbf{v}_i = \sqrt{2}\frac{\Delta x}{\Delta t}\mathbf{c}_i$ for the diagonal directions.

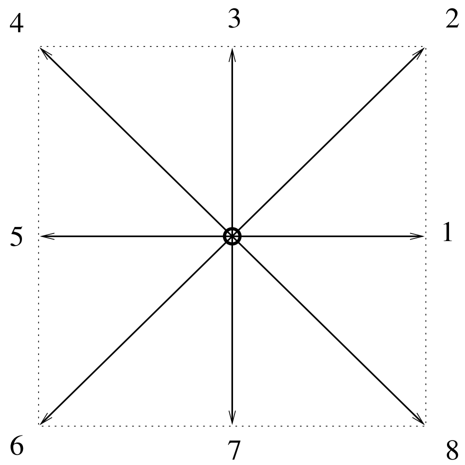

Figure 2.1: The grid stencil of the D2Q8 model.

2.3.1 Single time relaxation approximation

In LGA collisions are modeled by scattering of incoming particles. This can be expressed in a mathematical form by for example the Boolean operator D_i. However, in the context of LBM a direct connection can be made with the continuous Boltzmann equation from kinetic theory and thus existing knowledge may be used for modeling the collision term. In this way Qian et al. [21] and Chen et al. [22] independently proposed the single time relaxation approximation in which the collision process is modeled by a relaxation to the local equilibrium distribution function, the so-called Lattice-BGK model. This approximation has already been proposed by Bhatnager, Gross and Krook (BGK) in 1954, as an alternative collision model in the case of the continuous Boltzmann equation [17, 20]. In this model the collision term Ω_i is defined as,

$$\Omega_i = \frac{1}{\tau}(f_i^0(\mathbf{r},t) - f_i(\mathbf{r},t)),$$

where τ is the so-called relaxation parameter. The main assumption in the BGK model is that the fluid is locally close to thermal equilibrium and thus the dimensions of unit fluid volumes are much bigger than the microscopic scale (the mean-free path). The idea is that collisions tend to drive the system towards an equilibrium state, f_i^0, which is defined as [16],

$$f_i^0 = m_i\rho(a + \frac{b}{v^2}\mathbf{v}_i.\mathbf{u} + \frac{e}{v^2}u^2 + \frac{h}{v^4}(\mathbf{v}_i.\mathbf{u})^2), \tag{2.10}$$

where m_i, a, b, e and h are coefficients which should be determined according to mass and momentum conservation and the desired macroscopic behavior, as will be shown in the next section. Notice that Eq. 2.10 is a second-order expansion in velocity of the well known Maxwellian distribution [23] in the limit of small velocities (low Mach number).

2.3.2 The first-order distribution function

For the complete evaluation of Eq. 2.9, we still need to determine $f_i^{(1)}$ in terms of the density and the velocity. Here we do not go into the details of the derivation, but we state only the final results. The derivation is based on a Taylor expansion of the collision operator around the equilibrium state. After some algebraic manipulations and using the previously derived balance equations, the following expression can be derived [16]

$$f_i^{(1)} = -\Delta t\tau\frac{b}{v^2}m_i(v_{i\alpha}v_{i\beta} - \frac{av^2}{b}\delta_{\alpha\beta})\partial_{1\alpha}\rho u_\beta. \tag{2.11}$$

2.3.3 Lattice symmetries

In standard hydrodynamics the tensors in the momentum equation should be isotropic. This is due to the fact that in a real fluid stress effects relax equally in each direction. This implies that the tensors in Eq. 2.9 should be isotropic. This is the reason why in lattice Gas and lattice Boltzmann models only special lattices are used. For a square lattice isotropy is guaranteed by taken $m_i = 1$ for the diagonal links and $m_i = 4$ otherwise [16]. The following relations can then be derived,

$$\sum_{i=1}^{8} m_i v_{i\alpha} = 0 \qquad \sum_{i=1}^{8} m_i v_{i\alpha}v_{i\beta} = 12v^2\delta_{\alpha\beta} \qquad \sum_{i=1}^{8} m_i v_{i\alpha}v_{i\beta}v_{i\gamma} = 0$$

and

$$\sum_{i=1}^{8} m_i v_{i\alpha}v_{i\beta}v_{i\gamma}v_{i\delta} = 4v^4(\delta_{\alpha\beta}\delta_{\gamma\delta} + \delta_{\alpha\gamma}\delta_{\beta\delta} + \delta_{\alpha\delta}\delta_{\beta\gamma}),$$

with $\delta_{\alpha\beta}$ the Kronecker delta function.

2.4 The Navier-Stokes equations

By using the expression for f_i^0, f_i^1 and the isotropy identities we can compute $\Pi_{\alpha\beta}^{(0)}$, $S_{\alpha\beta\gamma}^{(0)}$ and $\Pi_{\alpha\beta}^{(1)}$. First, it is easy to see that the constraints

$$\rho = \sum_{i=1}^{8} f_i^0 \quad \text{and} \quad \rho\mathbf{u} = \sum_{i=1}^{8} f_i^0 \mathbf{v}_i,$$

and the isotropy identities, yield the following results for the coefficients of the equilibrium distribution function,

$$a = \frac{1}{20}, \qquad b = \frac{1}{12},$$

and

$$12h + 20e = 0. \tag{2.12}$$

Using the tensor identities and the definition of the equilibrium distribution function, $\Pi_{\alpha\beta}^{(0)}$ can be simplified as follows,

$$\Pi_{\alpha\beta}^{(0)} = \sum_{i=1}^{8} v_{i\alpha} v_{i\beta} f_i^0(\mathbf{r},t) = 12v^2(a + (e + \frac{h}{3})\frac{u^2}{v^2})\rho\delta_{\alpha\beta} + 8h\rho u_\alpha u_\beta.$$

Due to Galilean invariance the coefficient in front of the convective term should be equal to 1 and therefore $h = \frac{1}{8}$. Furthermore, using Eq. 2.12 it is easy to see that $e = \frac{-3}{40}$ and thus $\Pi_{\alpha\beta}^{(0)}$ can be rewritten as,

$$\Pi_{\alpha\beta}^{(0)} = p\delta_{\alpha\beta} + \rho u_\alpha u_\beta, \tag{2.13}$$

where the pressure p is defined as,

$$p = \frac{3}{5}v^2(1 - \frac{2}{3}\frac{u^2}{v^2})\rho = c_s^2\rho + O(u^2),$$

and c_s is the speed of sound. Notice that the pressure is velocity dependent. This unphysical effect can be eliminated by introduction of rest particles in the model [24]. By using the tensor identities and the relations for f_i^0 and f_i^1 we can analogously derive expressions for $\Pi_{\alpha\beta}^{(1)}$ and $S_{\alpha\beta\gamma}^{(0)}$ [16],

$$\varepsilon\Pi_{\alpha\beta}^{(1)} = \Delta t v^2 \tau[12a - 4b)\delta_{\alpha\beta}\nabla.\rho\mathbf{u} - 4b(\partial_\beta \rho u_\alpha + \partial_\alpha \rho u_\beta) \tag{2.14}$$

(here we have used $\varepsilon\partial_{1\gamma} = \partial_\gamma$) and

$$S_{\alpha\beta\gamma}^{(0)} = \frac{v^2}{3}\rho(u_\gamma\delta_{\alpha\beta} + u_\beta\delta_{\alpha\gamma} + u_\alpha\delta_{\beta\gamma}) \tag{2.15}$$

respectively. Substituting these computed expressions in Eq. 2.9 the following macroscopic equation can be derived after some algebraic manipulations [16],

$$\partial_t \rho u_\alpha + \rho u_\beta \partial_\beta u_\alpha + u_\alpha \nabla.\rho \mathbf{u} = -\partial_\alpha p + \Delta t v^2 (\frac{\tau}{3} - \frac{1}{6}) \nabla^2 \rho u_\alpha + \Delta t v^2 [\tau(\frac{2}{3} - 12a) - (\frac{1}{3} - 6a)] \partial_\alpha \nabla.\rho \mathbf{u} \tag{2.16}$$

In the case of an incompressible fluid one has $\nabla.\rho u = 0$ and we recover the usual Navier-Stokes equation

$$\partial_t \mathbf{u} + (\mathbf{u}.\nabla)\mathbf{u} = -\frac{1}{\rho}\nabla p + \nu_{lb} \nabla^2 \mathbf{u} \tag{2.17}$$

where ν_{lb} is the kinematic viscosity of the fluid in lattice units,

$$\nu_{lb} = \frac{\Delta t v^2}{3}(\tau - \frac{1}{2}). \tag{2.18}$$

Summarizing, the Lattice BGK model is based on the following physical constraints:

- The Boltzmann molecular chaos assumption;
- The Chapman Enskog expansion and the single time relaxation to the equilibrium distribution are only valid in the limit of low Knudsen number (the Knudsen number is the ratio of mean free path to the characteristic flow length);
- The expansion of the equilibrium distribution function is only valid in the limit of low Mach numbers;
- The lattice and the coefficients in the equilibrium distribution function must be chosen such that the macroscopic equations are isotropic.

2.5 Regularly used LBGK models

Many different formulations of the lattice-BGK model can be found in the literature. The differences mainly lie in the connectivity of the lattice used. In two dimensions 7 or 9 links per lattice point (the D_2Q_7 and D_2Q_9 models, respectively) are frequently used, while in three dimensions 15 or 19 links per lattice point (the D_3Q_{15} and D_3Q_{19} models, respectively) are regularly used, in addition to models without rest particles (the D_3Q_{14} and D_3Q_{18} models). In this thesis the D_2Q_9 model is used in the two-dimensional simulations, whereas in three dimensions the D_3Q_{15} and the D_3Q_{19} models are considered. In the D_2Q_9 model each lattice point is connected to its eight nearest and diagonal neighbors. In the D_3Q_{19} model each lattice point is connected to its six nearest and twelve diagonal neighbors at a distance of $\sqrt{2}$, while in the D_3Q_{15} model each lattice point

is connected to its six nearest and eight diagonal neighbors at a distance of $\sqrt{3}$ (see Fig. 3.7). Rest particles are included in all three models.
The time evolution of the lattice-BGK model is described in the previous section. However, we will use a commonly used formulation for the equilibrium distribution function [21]

$$f_i^0 = t_i\rho(1+\frac{1}{c_s^2}(\mathbf{c}_i\cdot\mathbf{u})+\frac{1}{2c_s^4}(\mathbf{c}_i\cdot\mathbf{u})^2-\frac{1}{2c_s^2}u^2), \tag{2.19}$$

where t_i is a weight factor depending on the length of the vector $\mathbf{c}_i$, and c_s is the speed of sound.

Model	**0**	**I**	**II**	**III**
D_2Q_9	$\frac{4}{9}$	$\frac{1}{9}$	$\frac{1}{36}$	0
D_3Q_{15}	$\frac{2}{9}$	$\frac{1}{9}$	0	$\frac{1}{72}$
D_3Q_{19}	$\frac{1}{3}$	$\frac{1}{18}$	$\frac{1}{36}$	0

Table 2.1: The coefficients t_i in the equilibrium distribution function $f_i^{(0)}$ for the different lattice-BGK models [21, 24]. 0 indicates a rest particle, I is for links pointing to the nearest neighbors, II is for the links pointing to the next-nearest neighbors, and III is for the next-next-nearest neighbors.

For the weight factors used in the different models see table 2.1.
The lattice-Boltzmann models presented here yield the correct hydrodynamic behavior for an incompressible fluid in the limit of low Mach and Knudsen numbers [21]. The kinematic viscosity of the simulated fluid ν and the speed of sound c_s expressed in lattice units, are $\nu_{lb}=\frac{\tau-\frac{1}{2}}{3}$ and $c_s=\sqrt{\frac{1}{3}}$ [21]. The fluid pressure $p(\mathbf{r},t)$ is given by

$$p(\mathbf{r},t)=c_s^2(\rho(\mathbf{r},t)-\bar{\rho}), \tag{2.20}$$

where $\bar{\rho}$ is the mean density of the fluid.

2.6 Taxonomy of LGA and LBM

In the previous sections we have shown that under specific assumptions the lattice BGK model simulate the behavior of incompressible fluid flow at a macroscopic scale. During the last years many different models have been developed (see Fig. 2.2). In this section we present an overview of these models.
As stated previously, the first particle based model that was proposed for simulating fluid flow was a lattice gas automaton on a square lattice, the so-called

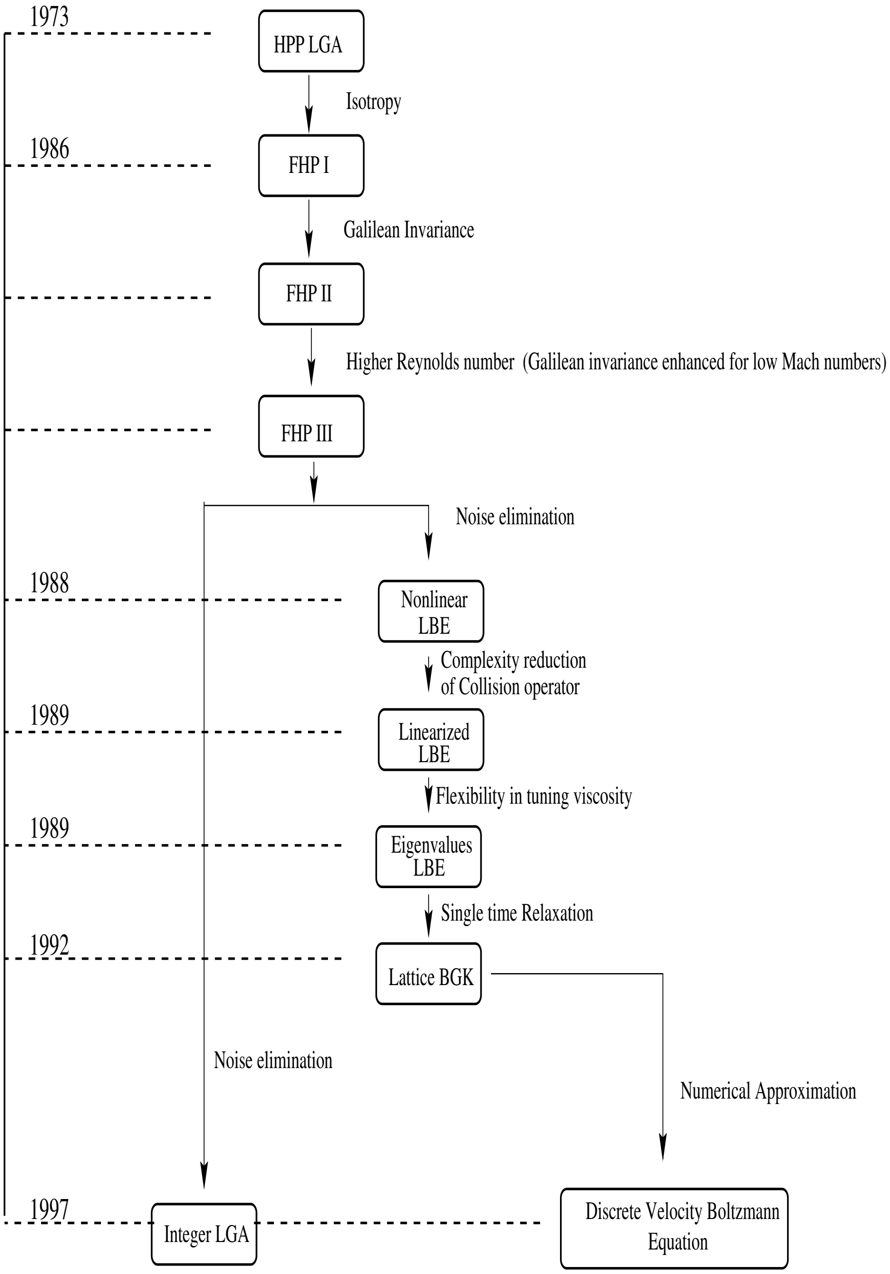

Figure 2.2: The development of the Lattice Gas and Boltzmann models.

HPP model [14, 15]. Although the basic ingredients for modeling the macroscopic behavior of fluid flow correctly, namely conservation of mass and momentum, were present in the HPP model, the viscous stress relaxation was not isotropic. Later, it was realized that isotropic behavior could be obtained by using a hexagonal lattice (FHP I model). However, as stated in the previous chapter these models were not Galilean invariant. This was due to a $g(\rho)$ factor in front of the convection term. By introducing rest particles in the model (FHP II) this $g(\rho)$ term could be set close to 1. In a next development the set of collisions that were allowed was extended (the FHP III model) in order to be able

to simulate higher Reynolds numbers (lower viscosities could be simulated by affecting the collision rate).
At this point one major artifact of all the LGA models was the statistical noise due to the boolean value dynamics. Due to the noise, averaging over a large number of lattice points and time steps were often required to produce smooth flow fields. In this context the statistical noise is considered as a disadvantage of LGA and the concept of lattice-Boltzmann methods was introduced to reduce it. The first method in the hierarchy of LBM was the non-linear lattice Boltzmann method [25]. The key idea was to track a population of particles instead of a single particle. In this model the collision was modeled by replacing the boolean **and** and **or** operators with **.** and **+**. Furthermore the collision operator is factorized by assuming the Boltzmann molecular chaos assumption, which states that the particle densities before and after the collision are not correlated. This simple modification eliminates the statistical noise problem. However, as we emphasized in the beginning of this chapter, the loss of particle correlations may be undesirable for some physical phenomena, e.g. reaction diffusion processes. Also the exact computing property of LGA is lost due to the floating point computations. For these reasons, LGA and LBM are still considered as two different approaches with their own favorable points and drawbacks.
The nonlinear LBM is more efficient compared to LGA, but the complexity of its collision operator is still exponential in the number of lattice bonds. This is due to the large number of post-collision states that are possible. In order to break down the exponential complexity of the collision operator a linearized version of the collision operator has been suggested [26]. In all these models, it was not possible to tune the viscosity of the simulated fluid, simply by adjusting some simulation parameters. The viscosity was adjusted by e.g. taking a different set of collision rules. In a later modification this shortcoming was also eliminated by reformulating the collision matrix as a function of its eigenvalues and eigenvectors [27, 28]. The simplest formulation of the collision operator is the BGK model in which the collision operator is implemented by means of a single time relaxation to the equilibrium distribution [21, 22]. The Lattice BGK model is a discrete formulation of the single relaxation time relaxation approximation of the collision process first introduced by Bhatnager, Gross and Krook in 1954 [17]. Note that the development of the different lattice models is much in the same line as the development of the Boltzmann equations in standard kinetic theory.
A few years ago it has been argued that the lattice-BGK scheme is a numerical discretization of the continuous Boltzmann-BGK transport equation for a discrete set of velocities (see addendum A) [29]. More specifically stated, the Lattice-BGK method can be derived from the discrete velocity Boltzmann equation by applying a first-order upwind space discretization and a first-order Euler time integration scheme. This similarity between LBGK and the discrete velocity Boltzmann equations seems to be promising in extending the standard Lattice-BGK scheme to simulations on for example non uniform lattices, thermal models, multi-phase flows etc.
Closely related to the spirit of LGA on the other hand, a new type of model has

been proposed which is based on integer arithmetic instead of boolean computations, the so-called Integer Lattice Gas model or multiparticle model [30, 16]. In this model the statistical noise of standard LGA is reduced and the model still has the nice feature of exact computation. This model is thus an intermediate approach which combines the good features of LGA with that of LBM.

Part II

Computational Methods

Chapter 3

Boundary Conditions and checkerboard effects in Lattice-BGK models

3.1 Introduction

In the previous part of this thesis we discussed the theoretical background of LBGK in detail. In this part * we address computational aspects related to LBM. We start with a benchmark study of the boundary conditions and regularly used 3D models (chapter 3). Next, we propose and verify a new technique to reduce the number of time-steps that are required to reach a steady state in LBM simulations (chapter 4). Furthermore, we discuss load balancing techniques for lattice-Boltzmann simulations that are generic for problems with a static workload (chapter 5). Finally, we propose a LBM scheme on nested grids and present some preliminary numerical results (addendum A).
In principle, it is known that the truncation error of the lattice-Boltzmann method is second-order in space. However, the accuracy of the solution depends on the boundary conditions and is found to be only first-order in many cases [31, 32, 33, 34, 35]. Understanding the effect of the boundary conditions is very important since they are crucial in many fluid-dynamical simulations. We discuss the boundary conditions for two common cases, namely the bounce-back boundary condition at a solid wall and the body force, which is often used as a substitute to pressure boundaries.
Besides the boundary conditions we also report on the regularly used 3D models. The D_3Q_{15} and the D_3Q_{19} model are considered. Here D denotes the dimensionality of the problem and Q is the number of bonds per lattice point [21, 22]. We show that, in the D_3Q_{15} model, checkerboarding in the fluid momentum can

*This chapter is based on the following publications:

- D. Kandhai, A. Koponen, A. Hoekstra, M. Kataja, J. Timonen, and P.M.A. Sloot, 'Implementation Aspects of 3D Lattice-BGK: Boundaries, Accuracy, and a New Fast Relaxation Method', *J. Comp. Phys.*, **150**, 482-501 (1999)

appear. In some cases this unphysical effect seems to be suppressed by boundaries. We discuss in some detail the numerical accuracy of these models.
In section 3.2 we discuss the bounce-back boundary condition and in section 3.3 we study the similarity of the body-force method and pressure-boundaries. Finally, in section 3.4 we study various 3D models and, especially, the checkerboard effect.

3.2 The bounce-back boundary condition

The bounce-back boundary rule is the simplest way to impose solid walls in lattice-Boltzmann simulations. Here, particles that meet a wall point are simply bounced back with a reversed velocity. It is obvious that this rule leads to a non-slip boundary (i.e. at the non-slip boundary the velocity of the fluid relative to the solid wall is **zero**) located *somewhere between* the wall nodes and the adjacent fluid nodes (in the literature this effect is known as the shift of the boundary). More sophisticated boundaries, which model a non-slip boundary exactly at the wall node (the so-called second-order boundaries), have been proposed by several authors [31, 32, 33, 36, 34, 35, 37]. Unfortunately most of them are restricted to regular geometries (like flat walls and octagonal objects) [31, 32, 33]. For practical simulations the bounce-back boundary is very attractive because it is a simple and computationally efficient method for imposing non-slip walls with irregular geometries.
Most previous studies of bounce-back have only considered flat walls, although a few more detailed studies have been published. Recently, an evaluation of the bounce-back method has been reported where the solutions obtained with the bounce-back rule were compared with those obtained with the finite-difference method for flow around octagonal and circular objects [38]. In this analysis the location of the non-slip boundary was taken to be at the wall node itself and the error in the solution was first-order convergent in space. Here we study the behavior of the bounce-back boundary for a similar geometry. Beside the standard analysis (i.e. where the location of the non-slip boundary is assumed to be *at* the wall node) our benchmark problem enables us to study the shift of the boundary for a specific staircase geometry, as will be shown in the following.
We chose the simple Poiseulle flow in a tilted channel as the benchmark problem. In this case the analytical solution for the velocity profile is known, and the effect of the bounce-back rule in a staircase boundary can be investigated by simulating fluid flow through an inclined tube (see Fig. 3.1a). The analytical solution for this problem (in lattice units) is given by

$$u_j = u_0 * (1 - \frac{j^2}{l^2}), \tag{3.1}$$

where u_j is the component of the velocity vector along the flow direction at a distance j from the center of the tube, l is the radius of the tube, and u_0 is the maximum velocity [3]. The absolute and relative errors at location j, ε_j^{abs} and

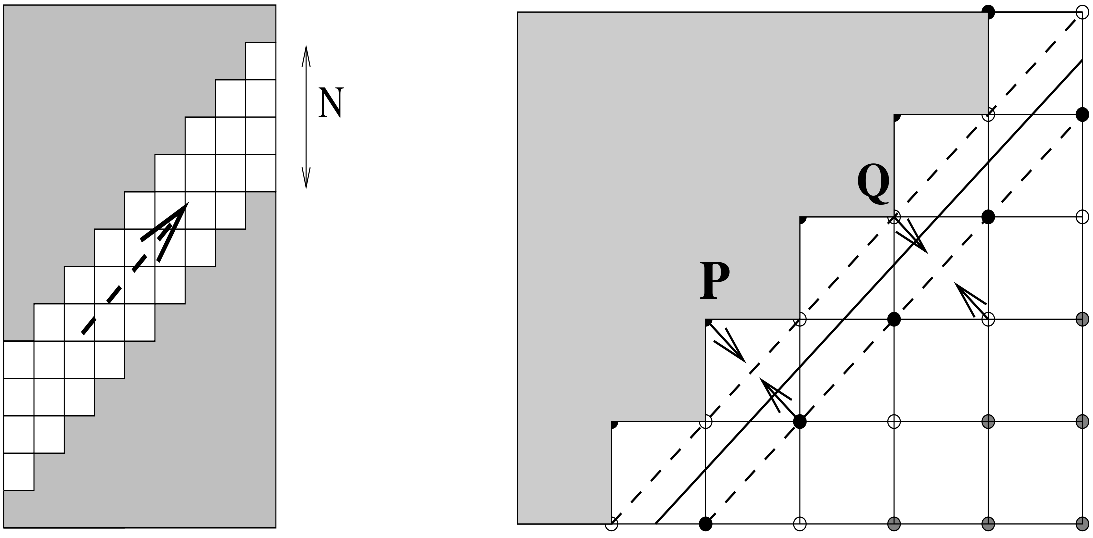

(a) (b)

Figure 3.1: The inclined tube flow benchmark. On the left the computational grid is shown and on the right the location of the wall. The meaning of points P and Q is explained in the text.

ε_j^{rel} respectively, are defined as

$$\varepsilon_j^{abs} = |u_j - \bar{u}_j|, \qquad \varepsilon_j^{rel} = |\frac{u_j - \bar{u}_j}{u_j}|, \tag{3.2}$$

where $\bar{u}_j$ is the simulated velocity at location j.
Periodic boundaries were imposed at the inlet and outlet of the tube, and a constant body force was used to drive the flow (*i.e.* a fixed amount of momentum $\mathbf{q}$ was added at every time step on each lattice point). More details related to the body force method can be found in the next section. The body force was directed along the flow direction, and periodic boundaries were implemented by taking into account the translation of the inlet and outlet in the vertical direction. The walls were modeled by the bounce-back boundary rule.
The mean relative error as a function of lattice spacing is shown in Fig. 3.2 for the standard bounce-back analysis. In this figure we included the results for the inclination angle $\alpha = 0$, 15, 30 and 45 degrees. As expected, a first-order convergence of the mean relative error is found in all cases (a fit to the data points gives a slopes of approximately -0.9 for all inclination angles). Furthermore, the error for the staircase geometries is on the average 50% higher than for the flat walls. The relative error close to the boundary nodes (very small velocities) is significantly higher than along the center of the tube (data not shown). This may explain why the lattice-Boltzmann method has proven to be an accurate method for the computation of mean flow quantities like *e.g.* the permeability of porous media. Moreover our results are of the same order as those of Galivan

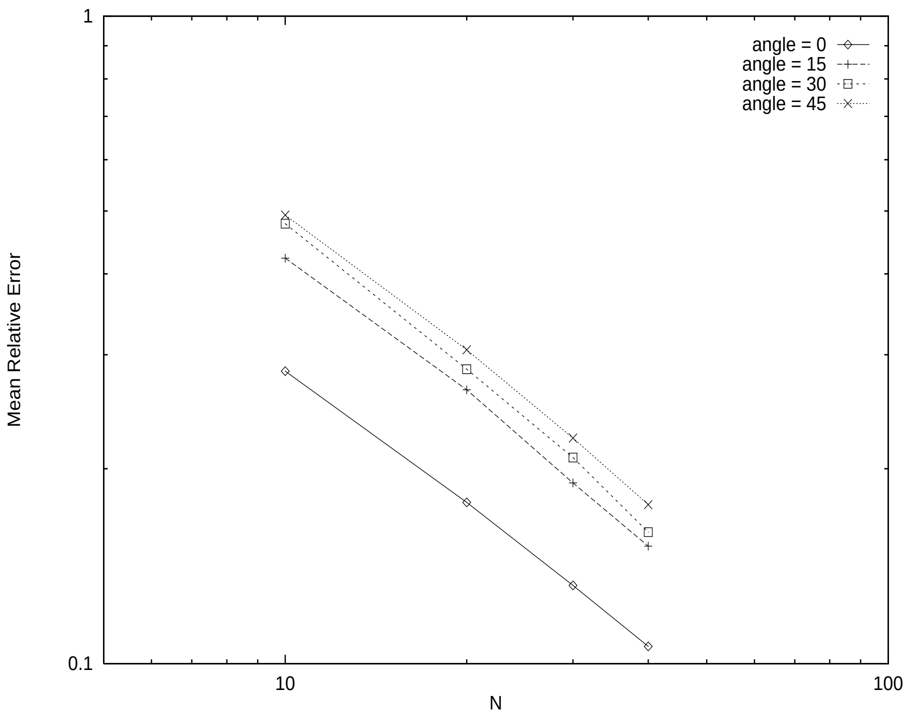

Figure 3.2: The mean-relative error in the inclined-tube flow simulations (angles 0, 15, 30 and 45 degrees) for the standard bounce-back analysis. Tube diameter is 10, 20, 30 and 40 lattice-points, $v_0 = 0.01$, $\tau = 1.0$.

et al. [38] (data not shown) for flow around octagonal cylinders when similar error metrics are used.

As discussed previously, the accuracy of the simulation is determined by the location of the non-slip wall. For flat geometries, it has been shown both numerically and analytically, that when the non-slip boundary is assumed to be in the middle of the first wall and the last fluid node, the error is second-order convergent [39]. In this case the analytic expression for the absolute error caused by the bounce-back boundary condition is given by [39]

$$u_j - \bar{u}_j = -\frac{u_0(4\tau(4\tau-5)+3)}{3(2l-1)^2}. \tag{3.3}$$

Notice that, according to Eq. (3.3), the "half-way shifted" wall is quite an accurate boundary condition for practical values of the relaxation parameter [39]. Furthermore, the location of the wall is exactly half-way ($u_j - \bar{u}_j = 0$) when the relaxation parameter is $\tau = 1.07$. We observed a very good agreement between our simulations and Eq. (3.3) (data not shown).

We also studied the shift of the boundary for non-flat geometries. Here we restricted the analysis to an inclination angle of 45 degrees. The "half-way shifted" location of the wall is expected to differ somewhat from that for a flat tube. In Fig. 3.1b we show the "half-way shifted" location of the wall. The stair-case geometry is staggered between two straight lines (lines through the type-P and type-Q points in Fig. 3.1b). Therefore, the "half-way shifted" boundary is also staggered between two straight lines (dashed lines in Fig. 3.1b). The location of the boundary is taken as the average of these two lines (see the thick solid line in Fig. 3.1b).

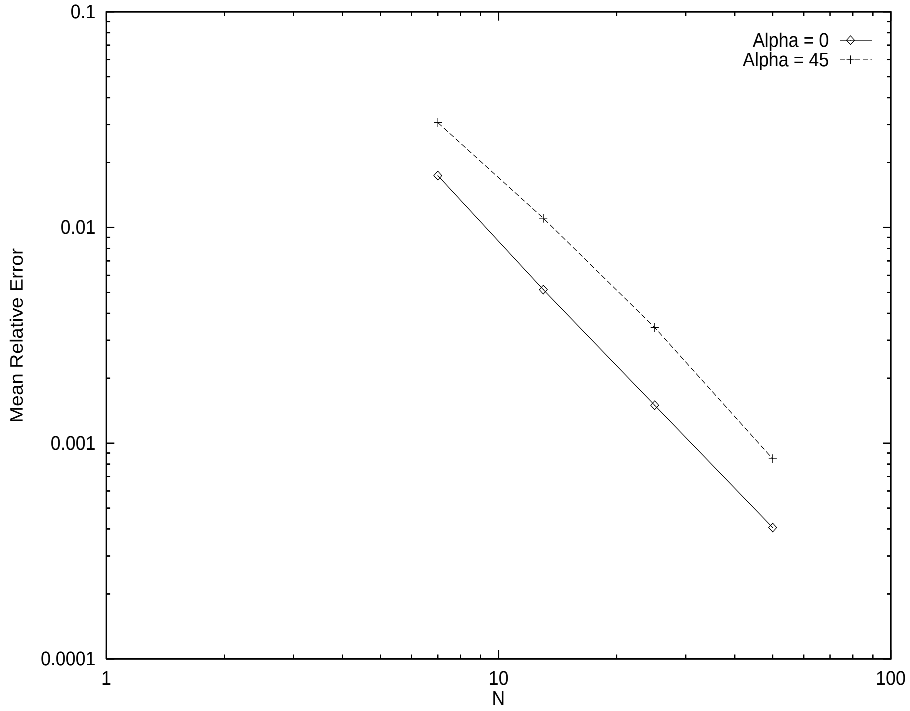

Figure 3.3: The mean-relative error on lattices with N = 7, 13, 25 and 50 lattice points is shown. Square (slope of the line is -2.0) and stars (slope is -1.9) are the half-way shifted results for flat and inclined tube respectively, $v_0 = 0.01$, $\tau = 1.0$.

The mean relative error as a function of lattice spacing is shown in Fig. 3.3. In this figure we included two curves, namely the results for the flat tube and the inclined tube experiment, where for both cases the wall is placed at the "half-way shifted" location. For both cases the error is second-order convergent (a fit to the data points gives an approximate convergence of -1.9). Furthermore, we clearly see that the range of the mean relative error for the flat tube is somewhat smaller than that for the inclined tube.

In Fig. 3.4 the error as a function of the relaxation parameter is shown. A qualitatively similar error behavior for the inclined- and flat-tube flow (Eq. (3.3)) is found. For an increasing relaxation parameter, the error first decreases and subsequently increases after some optimal value of the relaxation parameter. Here we clearly see that, for practical values of the relaxation parameter, the "half-way shifted" boundary is quite accurate. The optimal relaxation parameter in this case is approximately 1.55.

To summarize, we have seen that the error due to stair-cased structure is on the average 50% higher than for flat geometries. For a specific case ($\alpha = 45$ degrees), we verified that the bounce-back boundary rule tends to generate an imaginary boundary, which is located between the last fluid node and the solid wall. For the general case, it is expected that the exact location of the boundary depends

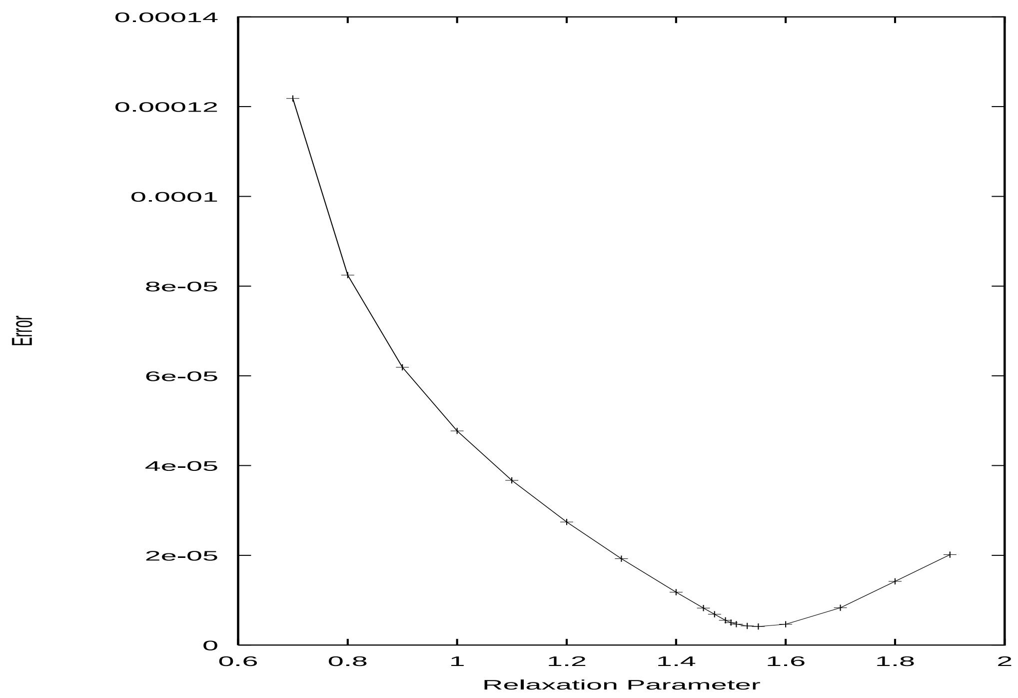

Figure 3.4: The mean-relative error as a function of τ for $N = 25$ and $v_0 = 0.1$.

on the relaxation parameter and the geometry of the problem. We believe that it is very difficult to predict the location of the non-slip wall for arbitrary geometries.

However, for geometries with finite curvatures, *e.g.* for spherical particles, we found that the difference between the hydrodynamic radius and the actual radius is quite small when the relaxation parameter is taken to be $0.7 \leq \tau \leq 1.3$, and the particle radius is expressed in the units of half lattice spacing (*c.f.* Section 4). Also, we have recently performed a detailed comparison between the lattice-Boltzmann method, the Finite Element method and experimental data for fluid flow in a complex 3D chemical mixing reactor (see chapter 6). The geometry of the reactor consisted of a number of solid tubes in different orientations and locations, and was such that it promoted mixing of fluid flowing through it. The results of the lattice-Boltzmann simulations were quite satisfactory even on moderate lattices. Supported by these results, we thus conclude that in irregular geometries the bounce-back boundary is certainly very useful despite its simplicity. In some applications however, sufficient accuracy may only be obtained on large lattices. In such cases, the accuracy can be increased by locally refining the grid in the vicinity of solid walls (see addendum A).

3.3 Comparison between body force and pressure boundaries

Successful numerical simulation of practical fluid-flow problems requires that the velocity and pressure boundary conditions have been set in a consistent way. However, general velocity and pressure boundaries are still under development for the lattice-Boltzmann method [12, 40, 41, 42, 43, 31, 32, 33, 34, 35, 44, 45, 46]. So far practical simulations have usually included first-order velocity boundaries [24, 47], and a body force [12, 48, 6, 49] has often been used instead of pressure boundaries in problems with a periodic geometry.

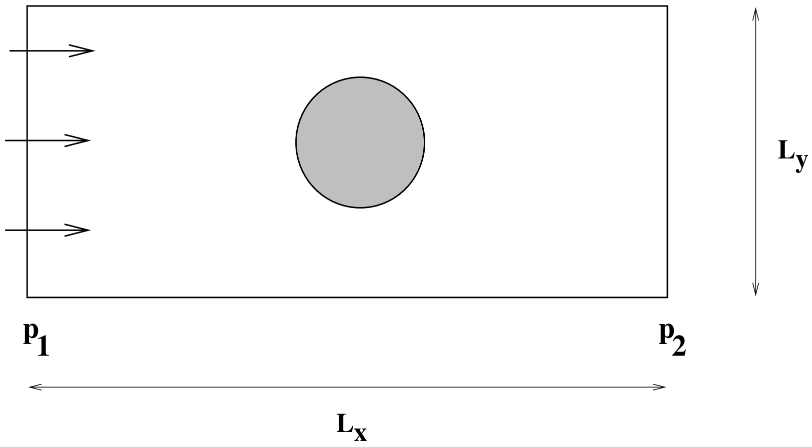

Figure 3.5: One unit shell in a vertically infinite array of cylinders. L_x and L_y are the length and the width of the unit shell, and p_1 and p_2 are the fluid pressures at the inlet and outlet, respectively.

Consider, *e.g.*, fluid flow through an infinite vertical array of cylinders, where pressure is kept constant in vertical planes in front and beyond the cylinders (see Fig. 3.5). Here, the use of body force instead of pressure boundaries is based on the assumption that the effect of the external pressure force $(p_1 - p_2)L_y\mathbf{e}_x \equiv Q\mathbf{e}_x$, is approximately constant everywhere in the system. Provided that this indeed is the case, and that the densities at the inlet and outlet surfaces are kept constant, pressure boundaries can be replaced with a global body force $Q\mathbf{e}_x$ that gives rise to an acceleration $g\mathbf{e}_x$ of the fluid. Pressure fields are then obtained from the effective pressure p_{eff}, which is defined as

$$p_{eff} = c_s^2 \Delta\rho - \bar{\rho} g x, \tag{3.4}$$

where x is the distance measured from the inlet of the system. Notice that, for a simple tube flow, the body force approach is an accurate substitute to pressure boundaries in that, *i.e.*, the velocity and pressure fields given by the two methods are identical.

In order to check the validity of the body-force and pressure boundaries approaches, we simulated the system shown in Fig. 3.5 with both the body force

and the pressure boundaries. The simulation lattice was $L_x \times L_y = 300 \times 100$ lattice points, the cylinder radius a_0 was 5.5 lattice points, the center of the cylinder was located 100 lattice points from the inlet, and periodic boundaries were used in the y direction. The cylinder Reynolds number, Re$= 2a_0U/\nu$, was varied between 0 and 6 by adjusting the LBGK relaxation parameter τ between 0.6 and 2.0.
In the body-force simulations periodic boundaries were used also in the x direction. Density, and thus effective pressure, were kept constant at the inlet and outlet. The fluid momentum was also kept constant to prevent the cylinders from seeing their periodic images in the x direction. This was done as follows: after the propagation step the average fluid densities ρ_{in} and ρ_{out}, and the average velocities $\mathbf{v}_{in} = \mathbf{P}_{in}/\rho_{in}$ and $\mathbf{v}_{out} = \mathbf{P}_{out}/\rho_{out}$, were first calculated at the inlet and outlet, respectively. (Here $\mathbf{P}_{in}$ and $\mathbf{P}_{out}$ are the corresponding total fluid momenta.) Then the particle densities f_i at the inlet and outlet were set to $f_{i,in} = f_i^{(0)}(\rho_{in}, \mathbf{v}_{in})$ and $f_{i,out} = f_i^{(0)}(\rho_{out}, \mathbf{v}_{out})$, respectively.
Pressure boundaries were implemented by the method described in Ref. [35]. Because in both cases velocity and pressure can develop freely, and the channel is big compared to the size of the cylinder, the conditions close to the cylinders are very similar in both simulations.
Notice that, when the system is fully saturated, the drag force acting on the obstacle completely cancels the effect of pressure or body force. So, if the pressure boundary of Ref. [35] is accurate, the two different methods should give equal drag forces.

Re	0	0.05	0.4	2	3	6
Mean ε_v	0.33	0.34	0.33	0.34	1.36	2.2
Max ε_v	0.81	0.96	0.79	0.86	2.35	62
Mean ε_p	0.24	0.24	0.27	0.46	1.9	3.94
Max ε_p	0.97	0.90	0.92	1.92	6.2	14.1
ε_d	$1.2 \cdot 10^{-8}$	$8 \cdot 10^{-4}$	$7.3 \cdot 10^{-3}$	7.710^{-2}	1.1	2.6

Table 3.1: The mean and maximum relative difference in the velocity, ε_v, pressure, ε_p and the drag forces, ε_d, acting on the particle, between pressure boundary and body force simulations for different Reynolds numbers. The numbers are expressed in percentages.

In table 3.1 we show for different Reynolds numbers the relative difference in the velocity, pressure and the drag forces acting on the particle, between the pressure boundary and the body force simulations. The difference is calculated in a box of 60×50 lattice spacings around the obstacle. The relative difference in the velocity, ε_v is defined as $\varepsilon_v = (v_p - v_b)/v_p$, where v_p and v_b are the velocities of the pressure boundary and body force simulations, respectively, and the relative difference in the pressure is defined as

$$\varepsilon_p = (\delta p - \delta p_{eff})/\delta p_{12}, \tag{3.5}$$

where $\delta p = p_{in} - p$ and $\delta p_{eff} = p_{eff,in} - p_{eff}$ are the pressure differences between the inlet and a point (x, y) for the pressure boundary and body force simulations, respectively. We chose $\delta p_{12} = p_1 - p_2$ as the reference scale instead of δp, because on many lattice points δp was very close to zero. We clearly see that for $Re \leq 2$ the mean relative difference in pressure and velocity is less than 1%. For higher Reynolds numbers bigger differences are found. These are probably caused by problems related to the pressure boundary conditions, because the drag in the pressure boundary simulations was not in good agreement with the expected value, in contrast with the results of the body-force simulations.

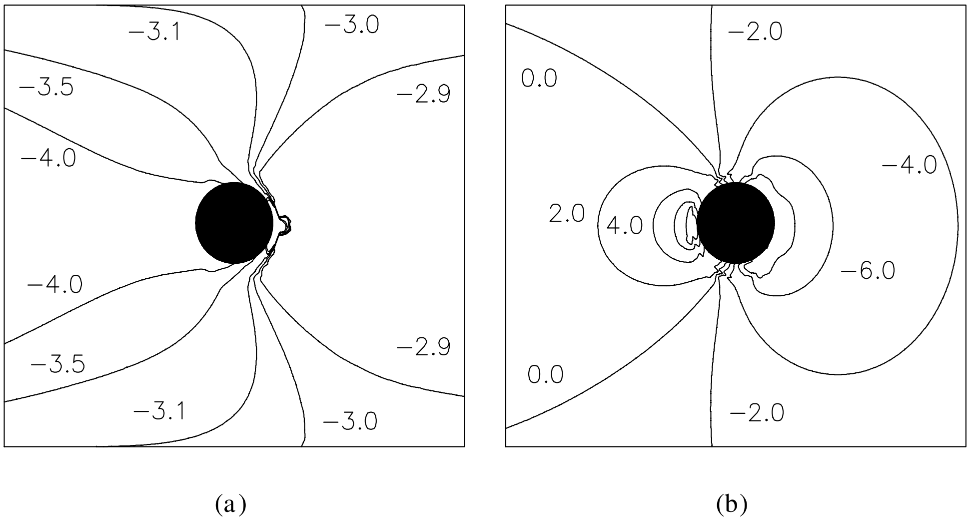

Figure 3.6: Comparison of relative difference of velocity and pressure for body force and pressure boundaries. The numbers are expressed in 1/1000 in both cases. The flow is from left to right. Fig. 3.6a. Contours of relative difference ε_v. Fig. 3.6b. Contours of relative difference ε_p.

In Fig. 3.6a we show the contour plot of the relative difference ε_v for Re= 0.4. The pressure boundary simulations systematically resulted in slightly smaller velocities, the average difference being $|\varepsilon_v|_{ave} = 0.33\%$. The biggest differences in the velocities, namely -0.79% and -0.74%, were found at the up-stream and down-stream stagnation points, respectively. The contour plot of ε_p is shown in Fig. 3.6b. Its average value was $|\varepsilon_p|_{ave}$ =0.27%. The maximum and minimum values for ε_p, namely 0.87% and -0.92%, are once again found at the stagnation points.

In addition to this benchmark, we studied a more complicated case, namely fluid flow in a disordered porous medium composed of non-overlapping spheres. The radii of the spheres were $a_0 = 5.5$ lattice spacings, the porosity of the medium was 0.8 and $\tau = 1.0$. The lattice dimensions were $L_x \times L_y = 500 \times 100$, and the porous medium was placed at a distance of 200 lattice spacings from the inlet and outlet. The obstacle Reynolds numbers were on average 0.003. The difference in the total drag given by the pressure boundary and body-force simulations was here quite high, namely 4%. The average relative differences $|\varepsilon_v|_{ave}$

and $|\varepsilon_p|_{ave}$ in the velocity and pressure fields were 4.2% and 2.2%, respectively, and the maximum differences of $|\varepsilon_v|$ and $|\varepsilon_p|$ were 28% and 4.3%. Thus, although the difference in total drag was quite big, the overall results were still quite satisfactory. Here we used the drag force acting on the particle as a reference. More detailed comparison of the complete velocity and pressure profiles for body-force driven simulations with results of traditional methods and experimental data of different problems for a wide range of Reynolds numbers, can be found in chapter 6 and Refs [50] and [51].
We can conclude that, for small Reynolds numbers and simple geometries, the body-force approach is quite an accurate substitute to pressure boundaries. However, for high Reynolds-number flows, where nonlinear effects are dominant, and for more complicated geometries, more sophisticated pressure boundaries are still needed.

3.4 Checkerboard effect in the D_3Q_{14} and D_3Q_{15} models

The lattice-Boltzmann method was originally developed from the lattice-gas automata. The first lattice used in 3D simulations was the D_3Q_{19} lattice [28], which is a 3D projection of the 4D FCHC lattice [12] used for 3D lattice-gas simulations (see Fig. 3.7a).

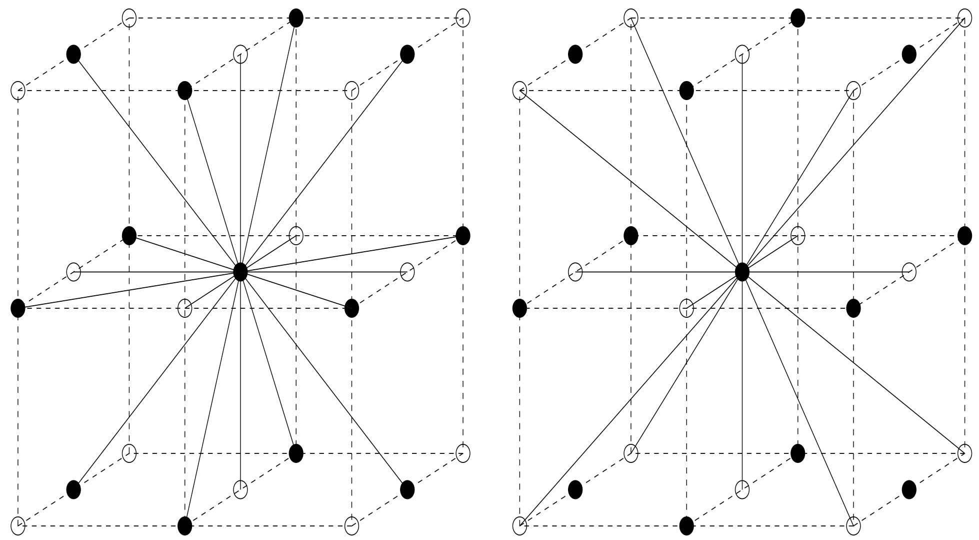

(a) (b)

Figure 3.7: Lattice structures of the D3Q19 (on the left) and D3Q15 (on the right) lattice-BGK models. The checkerboard coloring is included in the figures.

It was later realized that the relative freedom in choosing the lattice-Boltzmann equilibrium distribution function also gave some freedom in choosing the structure of the simulation lattice. As a result, the D_3Q_{15} model (see Fig. 3.7b) was developed [21]. The D_3Q_{14} and D_3Q_{18} models are obtained from the D_3Q_{15} and D_3Q_{19} models, respectively, by excluding the rest particles. However, the presence of rest particles is often desirable for improving the accuracy of the model [52]. Also, for a small relaxation time τ, the rest particles may be needed to stabilize the system [53]. Therefore, the D_3Q_{15} and D_3Q_{19} models are most often used in practical simulations.

The computational intensity and the memory requirements of LBM scale linearly with the number of fluid particles. The D_3Q_{14} and D_3Q_{15} models are thus somewhat more efficient than the D_3Q_{18} and D_3Q_{19} models. However, in the D_3Q_{14} and D_3Q_{15} models, checkerboard behavior in the fluid momentum can occur, *i.e.*, fluid momentum may form unphysical regular patterns. We demonstrate this below in the case of saturation of a random velocity field, and in the case of fluid flow around a spherical obstacle.

Let us mark the lattice points (i, j, k) by black colour if $i + j + k$ is odd, and by white colour otherwise, thus forming a checkerboard pattern shown in Figure 3.7 for the D_3Q_{19} and D_3Q_{15} models. To each lattice-Boltzmann fluid particle, we also assign the colour of the lattice point at which they reside in the beginning of the simulation. If there are no obstacles in the system, it is easy to see that, in the D_3Q_{14} model, the black and white particle populations are completely independent of each other: the colour of the lattice point at which a given fluid particle resides changes at every time step (see Figure 3.7b). As a consequence of this checkerboard effect, the total mass and momentum of the black and white particle populations are spurious invariants, *i.e.* unphysical conserved quantities in the D_3Q_{14} model. Similar spurious invariants are also found in the HPP lattice-gas models [13]. These invariants can create unphysical hydrodynamic modes in the simulated system, and for this reason they should be eliminated from the model [12]. Notice that, in the D_3Q_{18} model, the black and white populations mix immediately with each other. Consequently, there is no checkerboard effect in this model.

In the D_3Q_{15} model the black and white populations are not entirely independent as they are coupled through the rest particles. Here, however checkerboard effects may also lead to unphysical behavior. If the lattice is initialized with equilibrium distributions such that, *e.g.*, the velocity is set to $\mathbf{u}_b$ at black lattice points and to $\mathbf{u}_w$ at the white lattice points, while $|\mathbf{u}_b|$ is equal to $|\mathbf{u}_w|$, it is easy to see that the total momenta of the black and white populations are conserved quantities.

We studied the checkerboard effect by following the relaxation of a perturbed velocity field with a constant initial density and with periodic boundaries imposed in all directions. We used two different lattices. In the first case the lattice dimensions were $10 \times 10 \times 10$ lattice points. When a steady state was reached in the D_3Q_{19} model, all components of the particle momenta were found to oscillate at each lattice point between two values (see Figure 3.8a). Such oscillations are caused by the so-called staggered invariants [40, 41]. They can be removed with proper initial conditions, and their effect can also be filtered out by averaging the momenta over two time steps. After time averaging the momentum field was uniform, as expected [40, 41]. In the D_3Q_{15} model, the fluid remained partially unmixed in the steady state. After time averaging, two different values for the particle momenta were found in the lattice (see Figure 3.8b), and each component of momentum was constant along lines parallel to the corresponding direction. The x component, *e.g.*, was constant on lines parallel to the x axis, and its distribution in the yz plane formed a checkerboard pattern. The relative difference between the two values of the momentum varied in the simulations, being typically 0.5 – 3%.

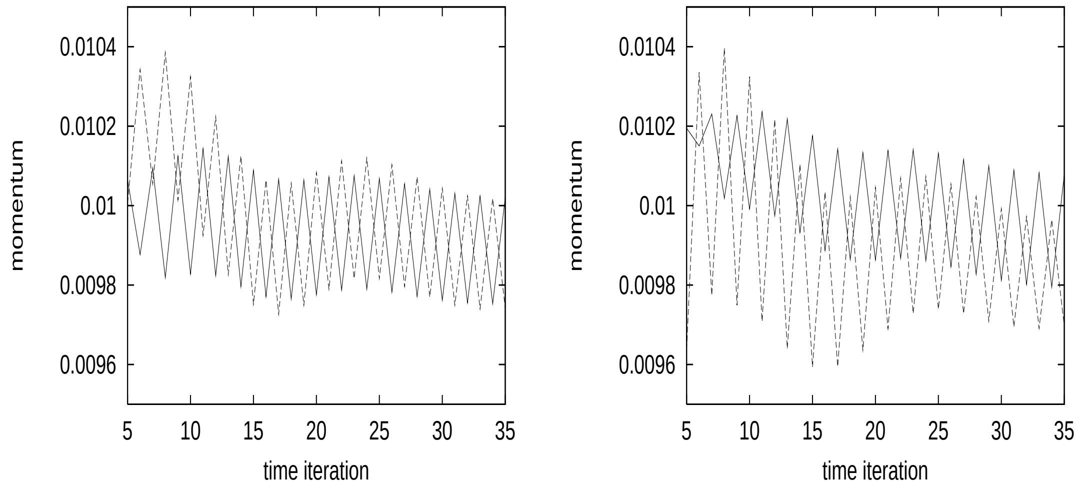

(a) (b)

Figure 3.8: Relaxation of the x components of the momenta of two next-nearest neighbors in the xy plane on a lattice of dimension $10 \times 10 \times 10$. On the left and right we show the time evolution of the D_3Q_{19} and D_3Q_{15} models, respectively. The initial perturbed velocity field is the same in both models.

Similar simulations were also performed on a $9 \times 9 \times 9$ lattice. In this case the two populations had additional mixing on the boundaries of the lattice, as the coloring rule was not continuous, due to the length of the lattice being an odd number. As a result, the steady-state momentum field was uniform for both models even without time averaging, *i.e.*, both the staggered invariants and the checkerboard effect were eliminated in the end. However, the weak coupling between the black and white populations in the D_3Q_{15} model was still apparent in the time evolution of the relaxation process.
This can be seen in Figure 3.9, where relaxation of the momenta of two next-nearest neighbors is shown in one direction. In the D_3Q_{15} model the relaxation process is significantly slower, and there are long-lasting oscillations in the local values of the momentum in this case.
We also studied the checkerboard effect in the presence of solid walls. The first test case was fluid flow in a rectangular duct. The duct dimensions were 30×30 lattice points, the relaxation parameter was $\tau = 1.0$, and bounce-back at the

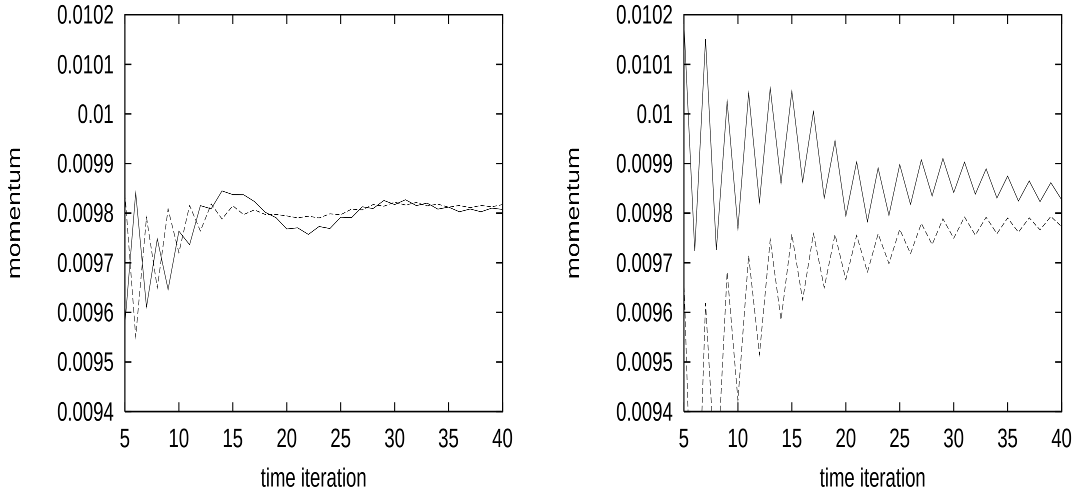

(a) (b)

Figure 3.9: Relaxation of the x components of the momenta of two next-nearest neighbors in the xy plane on a $9 \times 9 \times 9$ lattice. On the left and right we show the time evolution of the D_3Q_{19} and D_3Q_{15} models, respectively.

nodes was used on the solid walls. Periodic boundaries were used in the direction of flow driven by a body force. In this case no checkerboard effects were seen, and the average relative difference $|\Delta v| = |(v_{Q19} - v_{Q15})/v_{Q19}|$ between the velocity fields given by the D_3Q_{19} and D_3Q_{15} models was only 0.34%. (A detailed duct-flow comparison between the D_3Q_{18} and D_3Q_{15} models has previously been reported in Ref. [35], where the D_3Q_{18} model was found to be more accurate in general, while the results given by the D_3Q_{15} model were also found to be satisfactory.)

The second test case was fluid flow around a sphere. The radius of the sphere was $a_0 = 5.5$ lattice points. In the first simulation, the lattice consisted of $30 \times 30 \times 30$ lattice points, and the relaxation parameter was $\tau = 1.0$. Bounce-back condition was used on the solid walls, and periodic boundaries were imposed in all directions. Flow was driven by a body force. In this case, the checkerboard effect did not lead to momentum oscillations, but appeared instead as unphysical patterns in the velocity and pressure fields.

We observed that the velocity field of the D_3Q_{15} model includes horizontal patterns which are not found in the D_3Q_{19} model. This kind of pattern is clearly seen in the values of Δv shown in Figure 3.10a. Similar patterns were also seen in the values of Δp (in this comparison Δp was calculated from Eq. (3.4)). In Figure 3.10b, the velocity profile at the inlet boundary is shown for the two models. It is evident that the D_3Q_{19} model generates a very smooth profile, whereas the D_3Q_{15} model generates a profile staggered between two smooth curves. The average values of $|\Delta v|_{ave}$ and $|\Delta p|_{ave}$ were 2.5% and 3.9%, respectively. The difference between the total momenta of the fluids was in steady state only 0.62%.

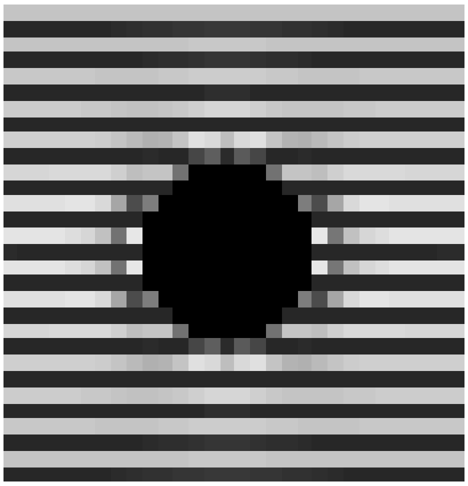

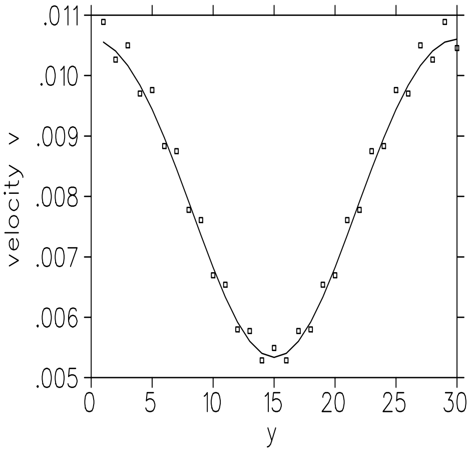

(a) (b)

Figure 3.10: The results for fluid flow around a sphere. The velocity field in a plane which bisects the sphere is analyzed. Fluid is flowing from left to right, and periodic boundaries are used in both directions. In Figure 3.10a the relative difference Δv between the velocity fields obtained by the D_3Q_{19} and D_3Q_{15} models is shown. The colors run from gray to white with the scale $-3.0\% \leq \Delta v \leq 3.0\%$. Figure 3.10b depicts the velocity profile at the inlet for both models. The solid line and open boxes show the results for the D_3Q_{19} and D_3Q_{15} models, respectively. For the results obtained by the D_3Q_{19} model, a solid line is drawn through the simulated points in order to illustrate the effect of checkerboarding more clearly.

For this reason *e.g.* the hydrodynamic radii a of the sphere (a detailed description of the determination of a is found in Refs [40, 41]) given by these models were very close to each other: the D_3Q_{15} and D_3Q_{19} models resulted in $a = 5.50$ and $a = 5.52$, respectively. We performed similar simulations with bounce back on the links, and on a lattice of $31 \times 31 \times 31$ lattice points. Similar patterns were seen also in these two cases.

We conclude that, in the D_3Q_{15} model, there is a checkerboard effect which may appear in the hydrodynamic fields. In some cases the boundaries can suppress this unphysical effect. However, it does not have significant effect on global values such as the average fluid momentum. Therefore, in spite of its shortcomings, the D_3Q_{15} model appears a viable alternative for steady-state hydrodynamics.

As Figure 3.9b shows, in dynamical systems (*e.g.* in fluid-particle suspensions or in turbulence simulations) the checkerboard effect may slow down the relaxation of momentum and can, in principle, produce unphysical effects in the dynamics of the system. Notice, however, that the solid boundaries increase mixing also in the D_3Q_{15} model in the case when bounce back on the links is used at the boundaries.

3.5 Conclusions

In this chapter we addressed various issues related to the lattice-BGK method which are important from a practical point of view. We first discussed the effect of the bounce-back boundary condition (which is widely used to model solid walls) for regular staircase boundaries. It was found that the error for staircased geometries is on the average 50% higher compared to that for flat walls. For a special case the bounce-back scheme was shown to be second-order convergent when the non-slip boundary was taken in the middle of the solid and adjacent fluid nodes. The quality of the method was determined by the compatibility of the shifted walls (the so-called hydrodynamic geometry) and the real geometry.
In addition, we also considered boundaries which are responsible for driving a flow between the inlet and outlet of the system. In this context we compared the well-known body-force approach with pressure boundaries. For low Reynolds numbers and simple geometries good agreement between these approaches was found.
Apart from the evaluation of the boundary conditions, we studied two common implementations of the lattice-Boltzmann model in $3D$ simulations. It was shown that within the D_3Q_{15} model, an unphysical checkerboard effect can be found, which generates spurious conservation of momentum and mass of two distinct populations of particles. For some stationary flows, this unphysical effect generates unphysical patterns in the hydrodynamic fields. However, in the test cases the overall effect of these artifacts is negligible.

Chapter 4

Iterative Momentum Relaxation for Fast Lattice-Boltzmann Simulations

4.1 Introduction

Lattice-Boltzmann simulations are often used for studying steady-state hydrodynamics. In these simulations, however, the complete time evolution starting from some initial condition is computed due to the transient nature of the scheme. In this chapter * we present a refinement of body-force driven lattice-Boltzmann simulations that may reduce the simulation time significantly. This new technique is based on an iterative adjustment of the local body-force and is validated on three test cases, namely fluid flow around a spherical obstacle, flow in random fiber mats and flow in a static mixer reactor.
As most numerical algorithms, the standard lattice-Boltzmann scheme has its shortcomings. For instance, in a recently performed comparative study between the finite element and the lattice-Boltzmann method for simulating steady-state fluid flow in a SMRX static mixer reactor (see chapter 7), it became evident that the computational time (on a sequential machine) required by the lattice-Boltzmann method was higher than that of the finite element method for obtaining the same level of accuracy. The memory requirements on the other hand were lower for the lattice-Boltzmann simulations (details can be found in chapter 6 and Ref. [54]). It can be argued that the longer computational time of LBM is a direct consequence of the transient nature of this

*This chapter is based on the following publications:

- D. Kandhai, A. Koponen, A. Hoekstra, M. Kataja, J. Timonen, and P.M.A. Sloot, 'Implementation Aspects of 3D Lattice-BGK: Boundaries, Accuracy, and a New Fast Relaxation Method', *J. Comp. Phys.*, **150**, 482-501 (1999)
- D. Kandhai, A. Koponen, A. Hoekstra, and P.M.A. Sloot, 'Iterative Momentum Relaxation for Fast LBM Simulations' *High-Performance Computing and Networking 1999*, **LNCS 1593**, Springer-Verlag, 311-319 (1999)

algorithmic scheme. In this chapter, we present a new technique, namely the Iterative Momentum Relaxation technique (IMR), which can significantly reduce the saturation time. In this technique the body force which is often used to drive a flow in lattice-Boltzmann simulations, is adjusted dynamically by calculating the average loss of momentum due to viscous forces.
We first describe the concept of the IMR technique. Next, we discuss the results obtained with the IMR technique and finally the conclusions are presented.

4.2 The Iterative Momentum Relaxation (IMR) technique

Generally, flow simulations require a consistent set of boundary conditions for the solid walls and the in- and outlets. In Lattice-Boltzmann simulations solid walls are often imposed by using the bounce-back method, while inlet and outlets can be implemented by using pressure/velocity boundaries or body-forces[34, 55]. In the case of pressure/velocity boundaries the particle densities f_i at the inlet and outlet are chosen such that they yield consistent values for the velocity or pressure. In the body-force approach, which is somewhat restricted to problems with periodic geometries, the flow is driven by adding a fixed amount of momentum along the flow direction at each lattice point. The overall effect is that a pressure gradient is imposed between the inlet and outlet. For low Reynolds number flows, it has been shown for several benchmark problems that in the stationary state the hydrodynamic behavior of both the body-force and pressure/velocity boundaries are similar[55].
According to Newton's second law, the net force acting on the fluid phase during the simulation is equal to the rate of change of the total momentum,

$$\frac{d\mathbf{P}(t)}{dt} = \mathbf{Q} - \mathbf{T}(t), \tag{4.1}$$

where $\mathbf{P}(t)$ is the total momentum, $\mathbf{Q}$ is the total body-force and $\mathbf{T}(t)$ is the total viscous friction force due to the obstacles. In standard lattice-Boltzmann simulations the body-force is kept constant during the simulation, while the friction force depends on the velocity field and the geometry of the problem. A steady-state solution is reached when the total body force $\mathbf{Q}$ acting on the fluid is completely cancelled by the viscous friction force $\mathbf{T}$ due to the walls and obstacles.
The main idea of the IMR technique is to reduce the saturation time by adjusting the applied body force during the iteration depending on the change of fluid momentum at the iteration step considered. For some fixed amount of iteration steps (considered as a time interval in IMR) the momentum loss is computed and used to calculate the friction force acting on the fluid during that time interval as follows,

$$\mathbf{T}(t) = \mathbf{Q}(t) - \frac{d\mathbf{P}(t)}{dt}. \tag{4.2}$$

The body-force for the next time interval is then set equal to this guess. Notice that in this formulation, the body-force is no longer constant. Moreover, this

strategy does not influence the explicit character of the Lattice-Boltzmann algorithm and thus its efficient and straightforward parallelization.
In summary, the IMR technique can be described by the following algorithm. First a flow is initialized. After every t_{step} time steps, the following iterative procedure (where k denotes the iteration counter of the IMR-loop) is repeated:

1. Calculate the momentum change $(\Delta P)_k$ of the fluid phase in the direction of the body force during the next time step.

2. Calculate the average momentum loss $T_k = Q_k - (\Delta P)_k$ (Q_k is the total body force at the iteration step k) of the fluid due to the viscous forces during this time step.

3. Choose a new body force as $Q_{k+1} = T_k$.

The new body force Q_{k+1} accelerates the fluid during t_{step} time steps before returning to step 1. The simulation is carried out until the body force Q and the total momentum reaches an acceptable degree of convergence, similar to the heuristical approach for the convergence criteria used in standard lattice-Boltzmann simulations.

4.3 Simulation results

To validate the IMR technique, we simulated 3 benchmark problems, namely fluid flow around a spherical obstacle, flow in a random fiber mat (see chapter 8) and flow in an SMRX static mixer reactor (see chapter 7). We included the last benchmark, as it is one of the very few cases of fluid flow in complex geometries with well documented results from traditional numerical methods and experimental data.
In our first benchmark the sphere radius was $a_0 = 5.5$ lattice points and the lattice dimensions were $100 \times 100 \times 100$ lattice spacings. We performed simulations at two Reynolds numbers, namely $Re = 0$ (Stokes flow) and $Re = 1$. In both cases the IMR method was extremely efficient. One percent accuracy in the velocity and pressure fields was already obtained after 5000 time steps, whereas the constant body-force method would have required 180000 time steps (data not shown).
In our second test-case we computed the permeability k (a measure for the fluid conductivity through a porous material) of a random fiber web. The permeability can be computed from the expression $k = (\phi P \nu \rho)/(mq)$ where P is the total fluid momentum in the direction of the body force, m is the total mass of the fluid, ρ is the fluid density, and q is the body-force density in the fluid phase. In Figure4.1.a we show the time evolution of the fluid momentum in a $400 \times 400 \times 60$ lattice with a porosity of $\phi = 0.94$, when a constant body force (solid line) or the IMR method (dashed line) is used. It is evident that with the IMR method the momentum is saturated very quickly. An accuracy of 1% in the permeability

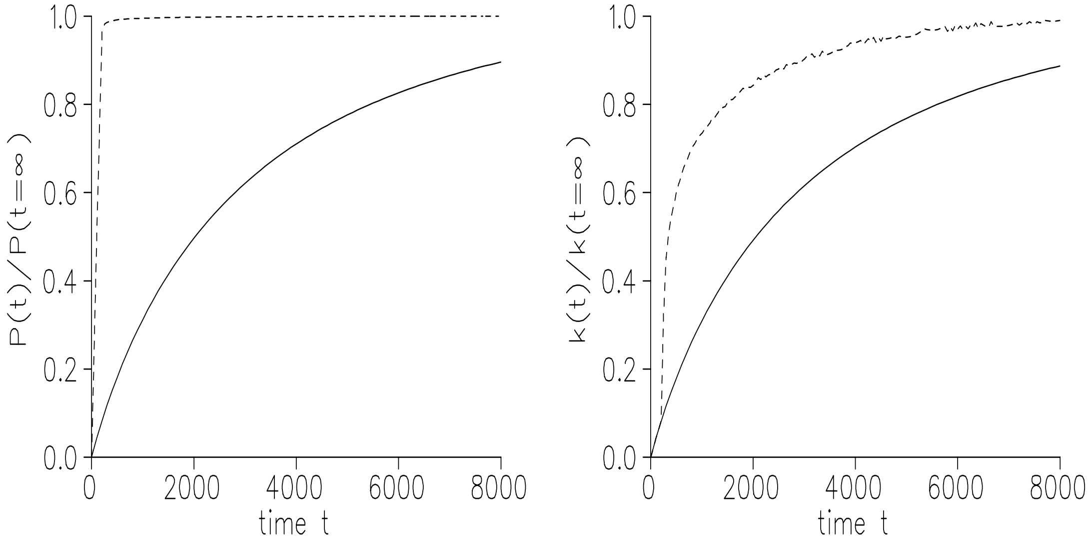

(a) (b)

Figure 4.1: Left: the time evolution of the fluid momentum $P(t)/P(t=\infty)$ when a constant body force (solid line) or the IMR method (dashed line) is used. Right: the time evolution of the web permeability $k(t)/k(t=\infty)$ when a constant body force (solid line) or the IMR method (dashed line) is used. Permeability $k(t)$ has been computed using the body force and total fluid momentum at time step t.

(and thus also in the body force Q) is reached in 7000 time steps, while the constant body-force method requires more than 18000 time steps for reaching the same level of accuracy (see Figure 4.1.b).

Our last test-case was fluid flow in a static mixer reactor. The SMRX static mixer reactor is a technology introduced $15-20$ years ago, which has gained more and more in popularity within the chemical industry over recent years. It is a plug-flow type reactor filled with a series of SMRX static mixer elements turned at 90 degrees with respect to each other. The mixer element consists of specially designed stationary obstacles which promotes mixing of fluid flowing through it. Its mixing mechanism relies on splitting, stretching, reordering and recombination of the incoming fluid streams. We focus on only one SMRX element. Due to usually rather complex flows and geometries, only few 3D numerical simulations of flow through static mixers were performed in the past [56]. We have taken this application as a benchmark, since it is one of the very few cases of fluid flow in complex geometries with well documented results from traditional numerical methods and experimental data.

The time evolution of the body-force and the total momentum along the flow direction for the lattice-Boltzmann simulations with a constant body-force and the IMR technique is shown in Figure 4.2. These simulations were performed for an element discretization of $56\times56\times56$ lattice points and the relaxation parameter τ was equal to 1. It is clear that the damping of the oscillatory behavior of the momentum is enhanced by the IMR technique. This is a result of the

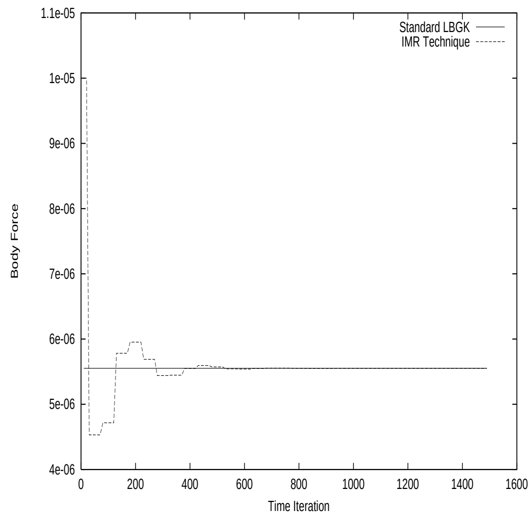

(a)

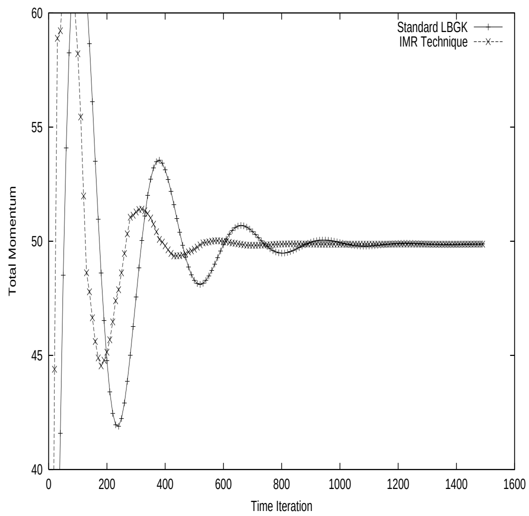

(b)

Figure 4.2: Left: Body-force as a function of the time iteration. Right: the time evolution of the total x-momentum along the SMRX reactor for the standard LBGK algorithm and the IMR technique is shown. $\tau = 1$ and the element dimensions are $56 \times 56 \times 56$ lattice points.

feedback of the flow field on the body-force. Moreover, both approaches clearly converge to the same value for the total momentum.

The time evolution of the relative difference in the total momentum along the flow direction, $\frac{|\Delta P_x|}{|P_x|}(t)$ (ΔP_x is computed between two results of two successive IMR trials), for the standard LBGK algorithm and the IMR technique is shown in Figure 4.3. From this figure, it is evident that with the IMR method the relative difference converges faster to some level of tolerance.

In Figure 4.4 we show the relative difference in the mean velocity along the reactor (in %) for different time-steps, in the case of the standard LBGK method (on the left) and the IMR technique (on the right). As reference data we used the simulation results obtained after 1500 time-steps, as then the simulations were completely saturated in both cases. With the IMR technique 1% accuracy in the velocity and the pressure fields compared to the reference data, was already reached after 550 time steps, whereas the constant body-force method required around 1000 time steps to reach a similar accuracy. Moreover, the steady state solution of both approaches are very close to each other (data not shown). The relative difference in the mean velocity along the reactor, between the stationary state of both approaches, is smaller then 0.07% (see Figure 6.4). In Ref. [54] we have shown in detail that the results of the standard LBGK method are also in good agreement with Finite Element calculations and experimental data. Thus we can conclude that the results obtained by the IMR technique are also consistent with experimental data.

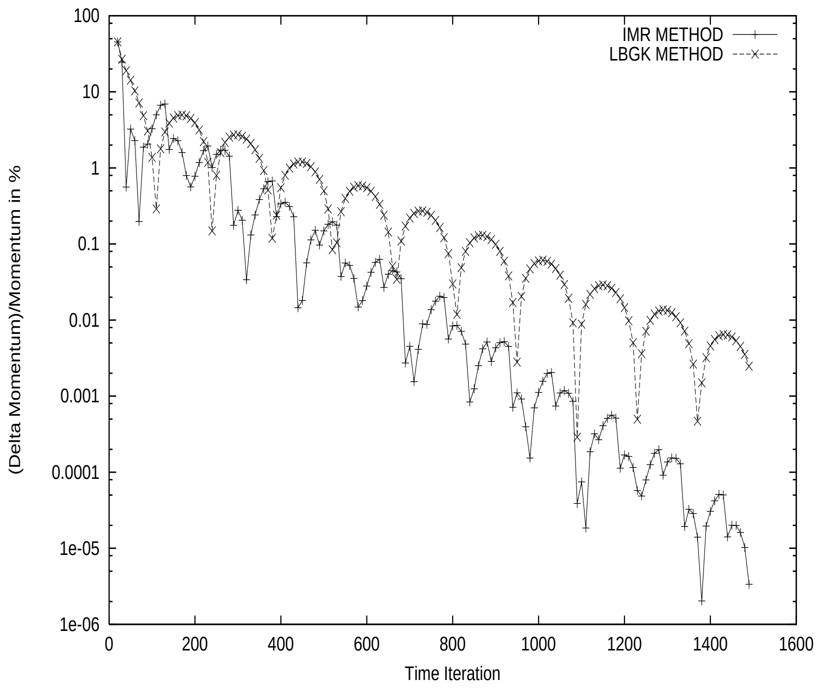

Figure 4.3: The relative difference (in %) in the total momentum along the flow direction, $\frac{|\Delta P_x|}{|P_x|}(t)$, as a function of time, for the standard LBGK algorithm and the IMR technique. $\tau = 1$ and the element dimensions are $56 \times 56 \times 56$ lattice points. In both cases the oscillatory behavior is due to a non-zero initial velocity field. In the case of the IMR technique more oscillations are present due to the iterative refinement of the body-force.

In this test case we used $t_{step} = 50$. Tests with some other values of t_{step} did not show significant improvements in the overall benefit gained by the IMR technique. Similar speedup results were also found for other Reynolds numbers provided that the flow is laminar.

4.4 Conclusions

In many lattice-Boltzmann simulations, the complete time evolution of the system is computed with a constant body force starting from some initial velocity and pressure fields. The number of time steps which is required to reach the steady state can then be very large in some cases. We presented a new technique for reducing the number of time steps that is needed to reach the steady state for body-force driven flows. This strategy does not influence the explicit character of the Lattice-Boltzmann algorithm and thus its efficient and easy parallelization. We conclude that at least in problems involving laminar flow, the IMR technique can be very efficient in decreasing the number of time steps needed to reach the steady state.

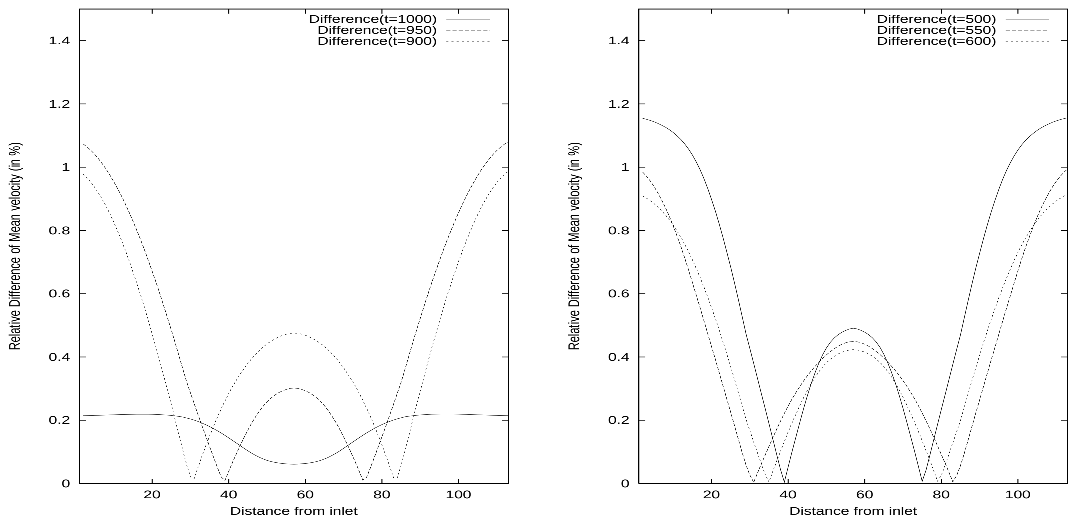

(a) (b)

Figure 4.4: On the left the relative difference in the mean velocity (in %) of the standard LBGK method is shown for $t = 900$, $t = 950$ and $t = 1000$. On the right the relative difference in the mean velocity (in %) of the IMR technique is shown for $t = 500$, $t = 550$ and $t = 600$. In both cases the relative difference is computed with respect to the simulation result at $t = 1500$ time-steps (simulation is then completely saturated) and the mean velocity is computed at different cross-sections along the reactor. $\tau = 1$ and the element dimensions are $56 \times 56 \times 56$ lattice points. The relative error is higher at the inlet and outlet, because the mean-velocity is smaller at those locations.

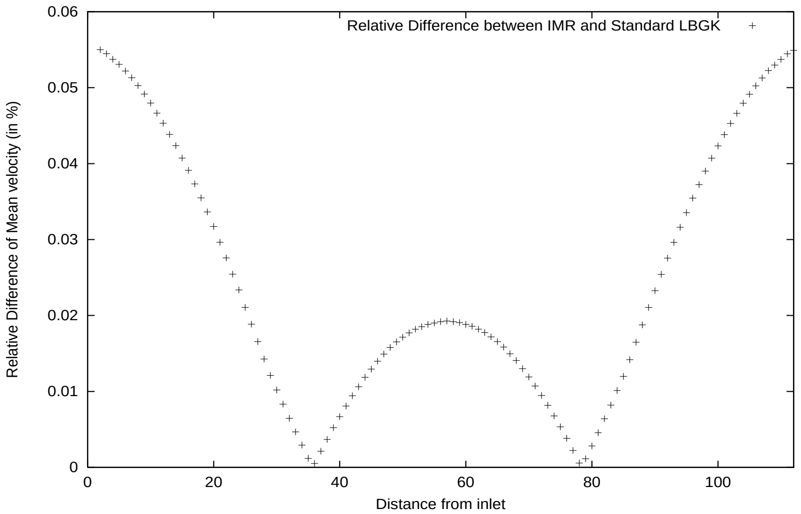

Figure 4.5: The relative difference between the mean velocity obtained by the standard LBGK method and the IMR technique after 1500 time steps.

Chapter 5

Load Balancing in Lattice-Boltzmann Simulations

5.1 Introduction

Realistic lattice-Boltzmann simulations often require large amounts of computational resources and are therefore executed on parallel systems. Generally, parallelization * of Lattice-Boltzmann simulation programs is based on one- and two-dimensional decomposition of the computational grid in equal sub-volumes, and load balancing is completely ignored for simplicity. These decompositions are therefore only efficient when the workload is distributed homogeneously † over the lattice.

However, in many fluid dynamical problems, the workload may be highly non-homogeneous and sometimes can even vary dynamically during the simulation. To facilitate efficient simulations of these problems, we developed a generic, portable parallel lattice-Boltzmann simulation program which can handle three domain decomposition strategies, namely slice and box decomposition and the Orthogonal Recursive Bisection (ORB) method. The ORB method can be used to generate approximately balanced decompositions by taking into account the workload on each lattice point. In this thesis we will restrict ourselves to applications with a static workload distribution.

To illustrate the usefulness of the different load balancing strategies we applied the methods to two realistic test cases. The first one is fluid flow through a massive random fibre network which poses a realistic model for man-made fibrous webs such as paper [57]. In this model, flexible fibres are positioned randomly over the grid on a flat substrate. Slice and box decomposition are therefore ex-

---

*This chapter is based on the following publication:

- D. Kandhai, A. Koponen, A. Hoekstra, M. Kataja, J. Timonen, and P. Sloot, 'Lattice-Boltzmann Hydrodynamics on Parallel Systems', *Comput. Phys. Commun.*, **111**, 14-26 (1998)

†By homogeneous workload distribution we mean that obstacles in the fluid are distributed uniformly over the lattice, while in a heterogeneous workload distribution this is not the case.

pected to be sufficient to achieve a relatively balanced and efficient parallel simulation. To clarify the idea of load balancing through the ORB technique, we also simulated fluid flow in a tube of varying cross-section, an example taken from a medical setup where blood cells are isolated due to their differences in sedimentation velocity [58]. It is shown that high parallel efficiencies can be obtained for both homogeneously and heterogeneously distributed workloads, thus supporting efficient simulations of a variety of realistic systems.
We shall first demonstrate that parallel computing is a practical technique to fulfill the computational requirements for simulating fluid flow in representative random geometries. Then we shall discuss in detail the different parallelization strategies, and study both homogeneously and heterogeneously distributed workloads.

5.2 Parallel computing in complex flow simulations

Parallel computing is often a prerequisite for achieving appropriate computing times and for fulfilling the memory requirements of large-scale 3D simulations. In this section we will shortly discuss the average computational requirements for simulating fluid flow in a prototypical realistic simulation, namely fluid flow in random fibrous media. The main emphasis is to illustrate the role of parallel computation in simulating realistic applications by the lattice-Boltzmann method.
As we have shown in chapter 3, the main artifacts of lattice-Boltzmann simulations are standard discretization errors and boundary effects due to the bounce-back rule. Apart from the error sources of the lattice-Boltzmann method, the computational requirements are also determined by the physical dimensions of the application to be simulated. For example, in the case of flow in representative random fiber mats, a square sample with an edge length of 4 fibre lengths in the horizontal plane and a height of 10 fibre thicknesses has to be used (details can be found in chapter 7. Moreover, due to the error sources of LBM, we found that lattices of 400x400x60 or 800x800x110 points (where an additional fluid layer of thickness 10 is included) are required to simulate a representative network with an accuracy of 15% (see chapter 9 for details). To represent the larger lattices using 32-bit real numbers, a memory capacity of the order of 5.4 Gb is required.
Moreover, estimates of timing requirements show that the real simulations would require approximately three hours of computing time on the full domain of a 64 -node Cray T3E system (with 128 Mb of main memory for each Digital Alpha EV5 300 Mhz processor) [59]. On a single processor it would take about 200 hours of computing time (assuming parallel efficiencies close to one). This is a serious bottleneck especially since in the present problem it is necessary to simulate several samples in order to find statistically confident correlations between permeability and various structural parameters of the fibre network.

It is therefore clear that parallel computing is the only possibility to fulfill the large computational requirements of the present prototype simulation and presumably of many other related practical problems.

5.3 Load balancing in a homogeneous workload distribution

Basically parallelization of grid based algorithms like those of finite-difference, finite-element and lattice-Boltzmann models is done by means of the data decomposition strategy where the computational grid is decomposed into subdomains [60]. Each processor performs computations on a certain sub-domain and exchanges information with other nodes in order to resolve dependencies. The two factors controlling the efficiency of parallelization are the ratio between the communication time and the computation time, and the balance of workload among the processors. In this section we will study parallelization of problems with a homogeneously distributed workload such as fluid flow in the random fibre network.

5.3.1 Slice and box decomposition

For problems with a homogeneous workload, parallelization can be done by means of a straightforward decomposition of the computational grid in equal sub-volumes, as discussed in Refs. [61, 62, 63]. With a moderate number of nodes, the decomposition may be done in one dimension ('slice decomposition') or in two dimensions ('box decomposition'). These methods depend only on the dimensions of the lattice and on the number of processors while the geometry of the application itself is neglected. An important feature of the lattice-Boltzmann schemes in this context is the inherent spatial locality of the collision operator. Furthermore, interactions between processors are only required at the propagation step. At this step particles on a border node can move to a lattice point in the domain of a neighboring processor or vice versa. By using a ghost layer of lattice points in the surroundings of the sub-domain, the propagation step can be isolated from the data exchange step. After the propagation step, the values in the ghost layer are send to the neighboring processors (communication process). The advantage of the slice and box decomposition is that the dependencies between the processors are simple due to the regular connectivity of the lattice and the fact that the partitions are of equal size.

The simulation program that is used in the present fluid flow problem was implemented in the programming language C. Parallelization was accomplished using features of the MPI message passing library [64].

5.3.2 Performance model and results

To get insight in the performance of slice and box decomposition, we derive first a simple time-complexity model with the following assumptions.

1. No overlapping in computation or communication between nodes.
2. No load imbalance due to the geometry of the problem. The only source of load imbalance may be caused by the number of lattice points being not divisible by the number of processors.

The turnaround time of one time iteration, $T(\mathbf{N}, p)$, is the sum of the computation time, $T_{calc}(\mathbf{N}, p)$, and the communication time, $T_{comm}(\mathbf{N}, p)$, where $\mathbf{N} = (N_x, N_y, N_z)$ gives the number of lattice points in each direction and p is the number of processors. For the slice decomposition (in the x direction),

$$T_{calc}(\mathbf{N}, p) \sim \lceil \frac{N_x}{p} \rceil N_y N_z \tau_{calc}, \qquad \text{and} \qquad T_{comm}(\mathbf{N}, p) \sim 20 N_y N_z \tau_{comm},$$

where the factor 20 originates from the number of neighbors (left and right), the number of communication actions per neighbor (send/receive), and the number of lattice vectors to be exchanged. The parameters τ_{calc} and τ_{comm} represent the time needed to perform one lattice-Boltzmann grid point update and the time needed to send one link value from a processor to a neighboring processor, respectively. In this model we neglected the communication latency. Analogously, it can be shown that, for the box decomposition (for an equal number of partitions in the x and y directions), the computation and communication times can be approximated by

$$T_{calc}(\mathbf{N}, p) \sim \lceil \frac{N_x}{\sqrt{p}} \rceil \lceil \frac{N_y}{\sqrt{p}} \rceil N_z \tau_{calc} \qquad \text{and} \qquad T_{comm}(\mathbf{N}, p) \sim 20(\lceil \frac{N_x}{\sqrt{p}} \rceil + \lceil \frac{N_y}{\sqrt{p}} \rceil) N_z \tau_{comm}.$$

The relative efficiency ε, a measure for the scalability of a parallel program, is defined as the ratio $\frac{p_0\, T(\mathbf{N}, p_0)}{p\, T(\mathbf{N}, p)}$ [62, 60], where p_0 is the minimum number of processors for which the job has been run. For these decompositions the relative efficiencies can be approximated by

$$\varepsilon_{slice} \sim \frac{1}{1 + \frac{20p}{N_x} \frac{\tau_{comm}}{\tau_{calc}}} \qquad \text{and} \qquad \varepsilon_{box} \sim \frac{1}{1 + 20(\frac{\sqrt{p}}{N_x} + \frac{\sqrt{p}}{N_y}) \frac{\tau_{comm}}{\tau_{calc}}}. \tag{5.1}$$

In Figs. 5.1 and 5.2 we plotted the measured relative efficiencies for slice and box decomposition together with a fit to the corresponding performance model for fibre networks of dimensions 100x100x60 and 200x200x110, respectively. We emphasize that the purpose of these fits is to gain more insight into the scalability of these decompositions with respect to the number of processors and the lattice dimensions. An actual performance prediction based on machine parameters is not very useful here due to the simplicity of the model. The computations were performed on a 64 -node Cray T3E system. The fits by the theoretical model, Eqs. (5.1), on the computed results for 100x100x60 and 200x200x110

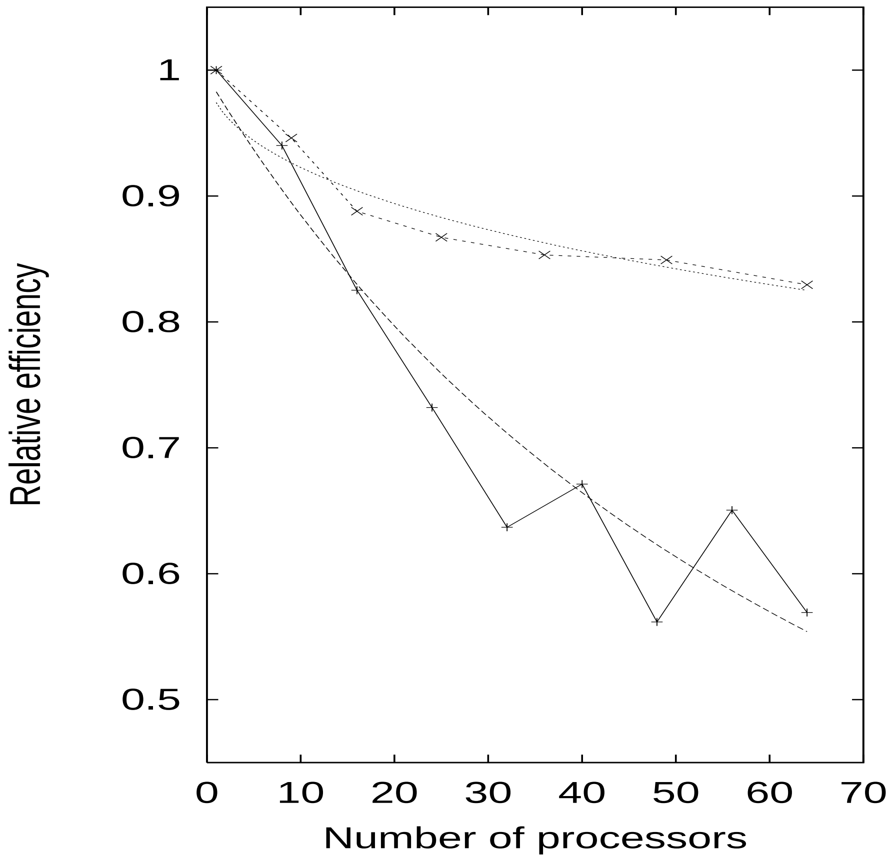

Figure 5.1: The relative efficiency as a function of the number of processors. The test problem is flow in random fibre networks on a lattice of dimensions 100x100x60. Solid line (with marked points) is the result for slice decomposition and dashed line (with marked points) is that for box decomposition. A least squares fit by the theoretical model is shown for both decomposition strategies.

lattice give for the slice decomposition $\frac{\tau_{comm}}{\tau_{calc}} = 0.06$ and 0.07, respectively and for the box decomposition $\frac{\tau_{comm}}{\tau_{calc}} = 0.07$ and 0.08, respectively.

The fluctuations of the data by almost 15% is due to the effect of caching and the load imbalance (when the number of lattice points is not evenly divisible by the number of processors). Similar fluctuations are also seen when flow in a geometry with no obstacles at all, is simulated (data not shown). It is evident from these experiments that slice and box decompositions are both efficient and useful strategies for problems with a homogeneous workload distribution. Slice decomposition is relatively easy to implement, but its efficiency is satisfactory only when the number of processors is relatively small (below 20, say). For the box decomposition, the efficiency with a lattice of 100x100x60 is around 0.9 on 64 processors.

For a large number of processors, it may become useful to extend these strategies to three dimensional cubic decompositions for which the relative efficiency

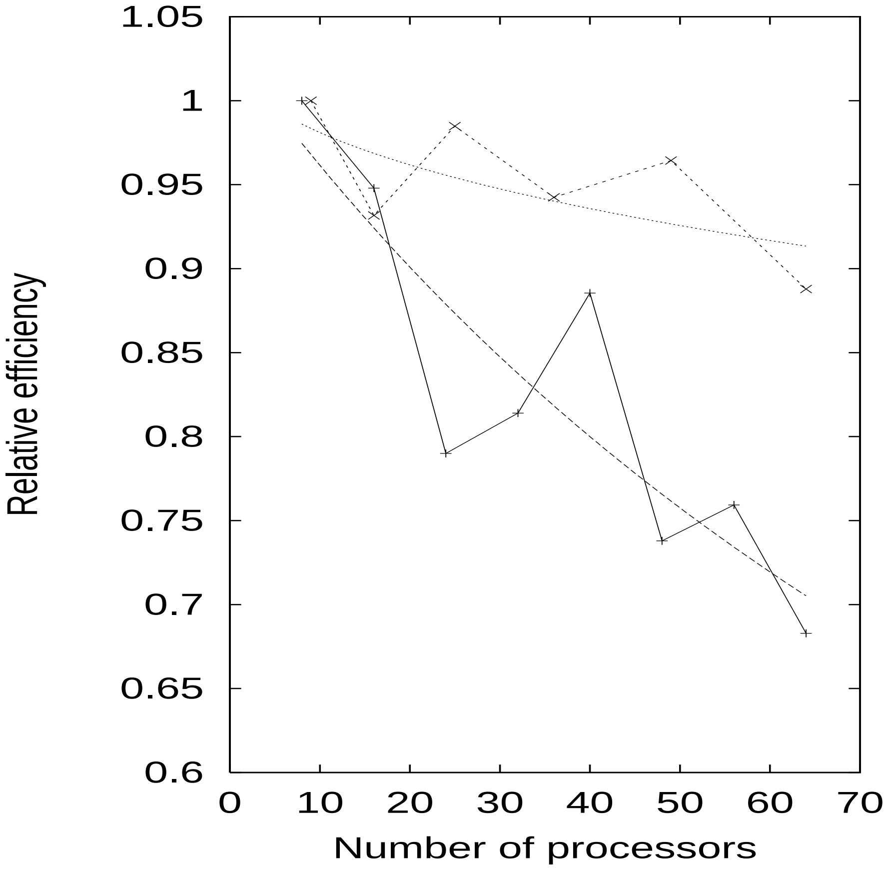

Figure 5.2: The relative efficiency as a function of the number of processors. The test problem is flow in random fibre networks on a lattice of dimensions 200x200x110. Solid line (with marked points) is the result for slice decomposition and dashed line (with marked points) is that for box decomposition. A least squares fit by the theoretical model is shown for both decomposition strategies.

can be approximated by,

$$\varepsilon_{cubic} \sim \frac{1}{1+20\left(\frac{p^{\frac{1}{3}}}{N_x}+\frac{p^{\frac{1}{3}}}{N_y}+\frac{p^{\frac{1}{3}}}{N_z}\right)\frac{\tau_{comm}}{\tau_{calc}}}.$$

5.4 Load balancing in a heterogeneous workload distribution

In the previous section we assumed that load imbalance among different processors is negligible. This is true for a random fibre network because the fibres are more or less homogeneously distributed in space. For a heterogeneously distributed workload, slice and box decompositions can result in a considerable load imbalance. Consequently the efficiency of the parallel program will decrease due to idle synchronization times. Also, one of the main advantages of the lattice-Boltzmann method is its suitability for a large class of different geometries, and in many fluid-dynamical problems workload is certainly not distributed homogeneously over the grid due to the geometry of the problem. It is therefore important to study decompositions that can deal with heterogeneously distributed workloads. The need for such load balancing approaches was already noticed in Ref. [61]. In this section we will analyze these issues in detail. For a typical example we take the simulation of flow in so-called centrifugal elutriation chambers [58, 65, 66, 67]. In centrifugal elutriation, human blood cells are isolated by means of differences in their sedimentation coefficients. The core of this technique is the combined effect of centrifugal and hydrodynamic forces acting on a blood cell moving in a rotating chamber. The geometry of the chamber (see Fig. 5.3) is a critical factor in the separation process [58], and is such that straightforward slice and box decompositions will create significant load imbalance among the processors.

5.4.1 Domain decomposition

The first step in load balancing is to find a partitioning of the grid such that differences in the workload of the processors are minimized. There are several ways to accomplish this goal, namely

1. Orthogonal Recursive Bisection: the computational grid is decomposed into partitions in an orthogonal direction, such that the workload is balanced. On each partition the same procedure is applied recursively. Workload due to obstacles in the fluid is neglected. The ORB method will create decompositions like the one in Fig. 5.3.

2. the Recursive Spectral Bisection method [60]: in the Recursive Spectral Bisection method both the connectivity of the grid and the workload at each lattice point are taken into account to find partitions with an optimal balance of both communication and computation;

3. load balancing by means of optimization strategies [68]: in this strategy, the computation and communication times are modeled by means of a cost function, and a partitioning which minimizes this cost function is approximated by means of optimization methods like the Simulated Annealing or Genetic Algorithms.

We have chosen the ORB method for two reasons. First of all, from a practical point of view minimization of the computation time is more important than minimization of the communication time. It became evident in our previous timing experiments that in the lattice-Boltzmann method the communication overhead is small for moderate lattice sizes. Secondly, the other two strategies are quite expensive and should be used when the communication time becomes significant.

5.4.2 Processor dependencies and performance results

The major difference between the ORB partitioning and the slice and box decompositions is the communication pattern of the processors. Each processor can now have a varying number of neighbors, and the interprocessor dependencies are more complicated for the corner points. In Fig. 5.4 this irregular communication pattern is clearly illustrated for the decomposition of Fig. 5.3. In the west direction *e.g.*, processor 5 will now exchange data with processors 1, 2 and 3, while processor 4 will only communicate with processor 1. Also the amount of data to be exchanged between the neighboring processors is not the same for each neighbor. This irregular communication pattern depends completely on the grid partitioning and thus on the geometry of the problem.

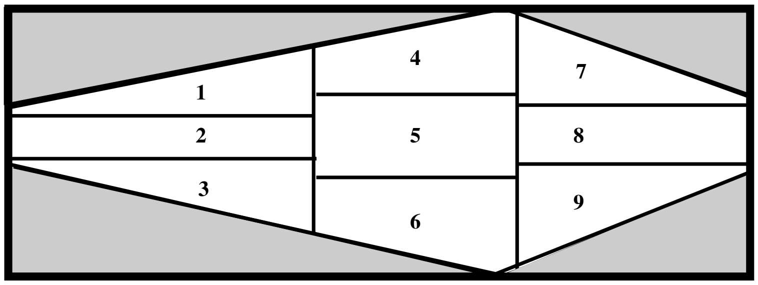

Figure 5.3: The elutriation-chamber geometry (tube of varying cross-section) and a 3x3 partitioning based on the orthogonal recursive-bisection method. Dark and white regions are solid and fluid space respectively.

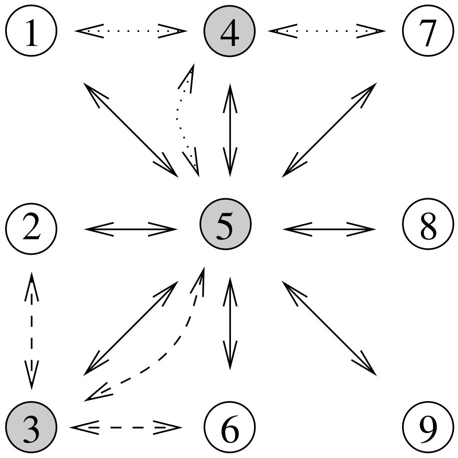

Figure 5.4: The irregular interprocessor dependency (for the decomposition of Fig. 5.3) in case of processors 3 (dashed), 4 (dotted) and 5 (solid arrows). The inter-processor dependencies are different for each node and depend on the decomposition.

We implemented the ORB strategy and performed timing measurements for the test problem of Fig. 5.3. The calculation time per processor is shown in Fig. 5.5 for a run on 16 nodes.

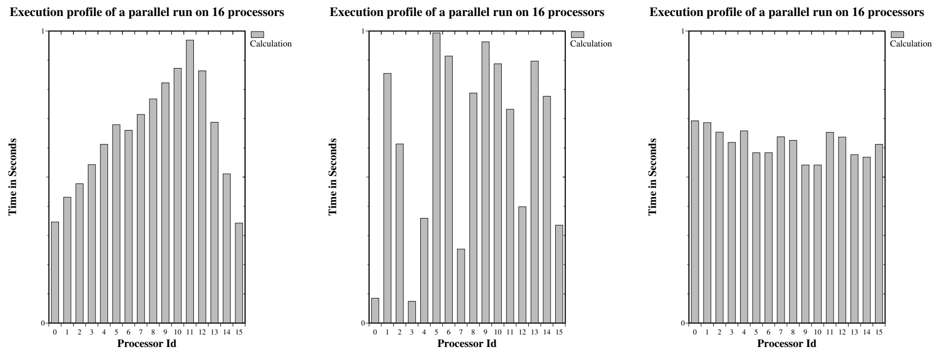

(a) Slice (b) Box (c) ORB

Figure 5.5: Execution profiles for the different decomposition methods. In this figure we clearly see that the slice and box decompositions are inefficient for this application. The execution profile obtained for the ORB decomposition is approximately balanced.

In this picture we included the cases where slice and box decomposition are applied to the same problem. It is evident that indeed both slice and box decomposition are inefficient approaches for this application. The workload between the processors is approximately balanced when the ORB method is used, while in slice and box decomposition we see big differences in the calculation times of the different processors.

p	T_{Slice}	T_{Box}	T_{ORB}	$\frac{min(T_{Slice},T_{Box})}{T_{ORB}}$
1	53.3	53.5	53.7	-
2	33.2	33.1	27.8	19.1 %
4	18.2	15.7	14.0	12.1 %
9	8.7	9.1	7.1	22.5 %
16	5.2	5.3	4.1	26.8 %

Table 5.1: The average execution time for 5 time iterations obtained by the different decomposition strategies for the test problem of Fig. 5.3. The problem size was 150x50x100 points. In the last column we show the benefit, which is defined relative to the minimum of the turn around times of slice and box decompositions. It is evident that for this specific test case slice and box decomposition are 12 to 27% less efficient compared to ORB.

p	T_{Slice}	T_{Box}	T_{ORB}	$\frac{min(T_{Slice},T_{Box})}{T_{ORB}}$
4	57	44.9	38	18.2 %
9	31.1	31.3	19.5	59.5 %
12	25	22.7	16.8	35.2 %
16	18.8	17.6	13.3	32.3 %
20	15.5	14.9	11.6	28.5 %
24	13.5	11.9	7.6	56.6 %

Table 5.2: The average execution time for 5 time iterations obtained by the different decomposition strategies for the test problem of Fig. 5.3. The problem size was 139x380x50 points. In the last column we show the benefit, which is defined relative to the minimum of the turn around times of slice and box decompositions. It is evident that for this specific test case slice and box decomposition are 18 to 60 % less efficient compared to ORB.

The results of timing measurements for different number of processors are shown in table 5.1 and 5.2. The ORB method is on the average 12 to 27% and 18 to 60% more efficient than the slice and box decomposition for a lattice of 150x50x100 and 139x380x50 points respectively. We expect that similar timing behavior will be found when both the problem size and the number of processors are increased. The benefit gained by load balancing will certainly be significant for large-scale simulations (execution time of many hours) and even higher for complicated fluid-dynamical problems like simulation of particle - suspensions in a chamber. The important point we want to emphasize here is that the extra communication overhead due to the irregular communication pattern is small. Extension of these ideas to dynamically varying workloads (as present in simulation of growth phenomena by convection-diffusion [6]) looks promising, especially because of this relatively small overhead.
Another important point is parallelization of lattice-Boltzmann models based on non-uniform lattices. It has been argued that one of the serious shortcomings of the lattice-Boltzmann method is the uniform nature of the lattice. Lattice-Boltzmann models based on non-uniform lattices have been proposed recently by several authors (see for example Refs. [69, 29] and addendum A). Parallelization of these models will certainly profit from using this load balancing approach.

5.5 Conclusions

We discussed a generic and efficient parallelization of the lattice-BGK method. The most straightforward parallelization is based on slice and box decomposition of the computational grid. By using this approach we obtained efficiencies varying between 0.8 and 0.9 for lattices of 100x100x60 points on 64 processors of a Cray T3E system. This approach is limited to problems with a homogeneous workload distribution. A property of the lattice-Boltzmann method is its suitability to a wide range of geometries. It is therefore important to study load balancing issues related to this method. We applied the ORB method to generate decompositions with approximately equal workloads. The main difficulty is that the communication pattern between the processors now becomes irregular. We found that the extra communication overhead associated with this irregular communication pattern is small and, for a test problem, on the average 12 to 60% increase in speed was gained in comparison with the slice and box decomposition.

We restricted our study to static workloads since all the applications that will be discussed in this thesis have a static computational geometry. However, in our research group much effort is put towards the dynamic load balancing subject. Recently, Schoneveld et al [70] studied rigorously dynamic load balancing strategies for Lattice-Boltzmann simulations with varying computational workloads. For this a generic framework based on dynamic data structures was developed that allows migration of computational cells among processors. As a test case a simulation of coral growth was considered. In this test case the real biophysical problem is to investigate the effect of flow and diffusion on the morphology of a model of a stony coral [6]. It was demonstrated that appropriate dynamic load balancing may have significant effect on the parallel performance of the simulations. Overeinder et al [71] extended the PVM parallel programming library with features for automatic balancing of computational tasks (Dynamic PVM library). In fact, they monitored the workload on each processor during a simulation. Whenever a significant imbalance in the computational work between the different processors is observed some of the tasks executed on a machine with a high load are migrated to an idle or less occupied machine. For different applications an average speedup of around 20% was gained.

Our aim is to extend our lattice-Boltzmann simulation kernel with functionalities to deal with multi-phase flows and moving particles and to combine that with the ideas for dynamic load balancing proposed by Schoneveld et al [70] and Overeinder et al [71]. In this way a lattice-Boltzmann simulation environment which is generic from both a parallel-computing and an application point of view will be realized. We believe that such an approach, which is typical in the field of computational science, is a fruitful strategy for modeling and simulation of a large class of realistic fluid-dynamical problems of great complexity.

Part III

Validation and Applications

Chapter 6

Lattice-Boltzmann and Finite-Element Simulations of Fluid Flow in a SMRX Mixer

6.1 Introduction

In the previous chapters we have studied various aspects of the lattice-BGK method. First, we presented some new results on the accuracy of the boundary conditions. Next, we proposed and validated a new relaxation technique to reduce the number of time-steps to reach steady state. Furthermore, efficient parallelization of the LBM scheme including load balancing methodologies based on the orthogonal recursive bisection technique were applied to a number of flow problems. Finally we studied grid refinement for 2D lattice-Boltzmann simulations.

In the remainder of the thesis we will focus our attention on applications. In this context our main interest is fluid flow in complex geometries focusing on fibrous porous media. Flow in fibrous media has many realistic applications as will become apparent in the next chapters. Before going into the details of the hydrodynamic properties of flow through fibrous media, we report in this chapter * a rigorous comparison between the finite-element and the lattice-Boltzmann method applied to a realistic test case with complex geometries.

We studied 3D fluid flow in a SMRX static mixer. A SMRX static mixer is a piece of equipment composed of cylindrical pipes with excellent mixing performance and it is used as a highly efficient chemical reactor for viscous systems like poly-

---

*This chapter is based on the following publications:

- D. Kandhai, D.J.-E. Vidal, A.G. Hoekstra, H. Hoefsloot, P. Iedema and P.M.A. Sloot, 'A Comparison between Lattice-Boltzmann and Finite-Element Simulations of Fluid Flow in Static Mixer Reactors', *Int. J. Mod. Phys. C*, **9**, 1123 (1998) .
- D. Kandhai, D. Vidal, A. Hoekstra, H. Hoefsloot, P. Iedema, and P. Sloot, 'Lattice-Boltzmann and Finite-Element Simulations of fluid flow in a SMRX Static Mixer', *Int. J. Num. Meth. Fluids*, In press.

mers [72]. The complex geometry of this mixer makes 3D simulations certainly non-trivial. We have chosen for this problem as a benchmark case, as it is one of the very few applications related to flow in complex geometries with well documented results obtained by state-of-the- art traditional numerical methods and experimental measurements.
It is important to notice that our comparative study between LBM and other traditional numerical methods is not the first one since the introduction of LBM. In the literature several studies can be found in which some kind of validation of the LBM results is included. However, a large number of LBM simulations have been validated only on a qualitative level. This is partly due to the fact that these applications were highly complicated and have hardly been studied using traditional methods. To convince people not familiar with LBM, of its effectiveness, rigorous comparative studies with standard state-of-the-art traditional methods such as finite-element methods are extremely important. This is especially necessary because the Lattice-Boltzmann method seems to be, at the first glance, too simple to be effective for realistic problems. The need for comparative studies of LBM has also been noted by Luo in Ref. [51]:
"Since LBE is a newly developed method and is still in its infancy, most numerical results obtained with this technique are qualitative in nature. (See, for example, results in the collective works edited by Doolen [73] and the recent reviews by Benzi et al. [28] and by Qian et al. [52]) High precision results of numerical simulations by the LBE method (e.g. work by Hou et al. [24]) are rarely available. Also, since the LBE method can handle complex boundary geometry easily, many LBE simulations have no counterpart produced with traditional numerical methods with which to compare. Thus, there is a pressing need for high quality numerical benchmarks using the LBE method which can be compared with the results obtained by traditional methods or by experiments."
The most notable comparative efforts are that of Hou et al. [24] and that of Luo [51]. Our study is different from theirs in two respects. First of all we study flow in quite complex geometries in 3D and we additionally compare the computational requirements of FEM and LBM in more detail. The studies of Hou et al. [24] and that of Luo [51] have focussed on simple 2D geometries, e.g. the cavity flow problem and the backward facing step. However, their studies are certainly relevant as they have studied the complex behavior that may emerge as the Reynolds number is increased. We restrict to the laminar flow regime as our main interest is in low Reynolds number flow.
A comparison of a lattice-Boltzmann method and a finite-element method, applied to the complex SMRX test case, will be presented from a theoretical, methodological and experimental point of view.

6.2 The Static Mixer Reactor

The static mixer, a rather new technology introduced 15 – 20 years ago, has gained more and more in popularity within the chemical industry over recent years [72]. It consists of specially designed stationary obstacles inserted in a pipe in order to promote mixing of fluid streams flowing through it. Its mixing mechanism relies on splitting, stretching, reordering and recombination of the incoming fluid streams. Compared to traditional mechanical mixing equipment, the static mixer offers several advantages: it has low maintenance and operating costs, low space requirements and no moving parts.

Nowadays, over 200 different designs are available on the market. They are widely used in all kinds of chemical processes. Among those are gas/liquid reactors, polymerization reactors, blending units, heat exchangers and, to summarize, devices for promoting homogenization in concentration, temperature or velocity (e.g. for uniform residence time). Among all the static mixer designs, one of the most complex is the SMRX, an SMR-type mixer manufactured by Sulzer Chemtech Ltd. and used mainly in polymerization reactors [56].

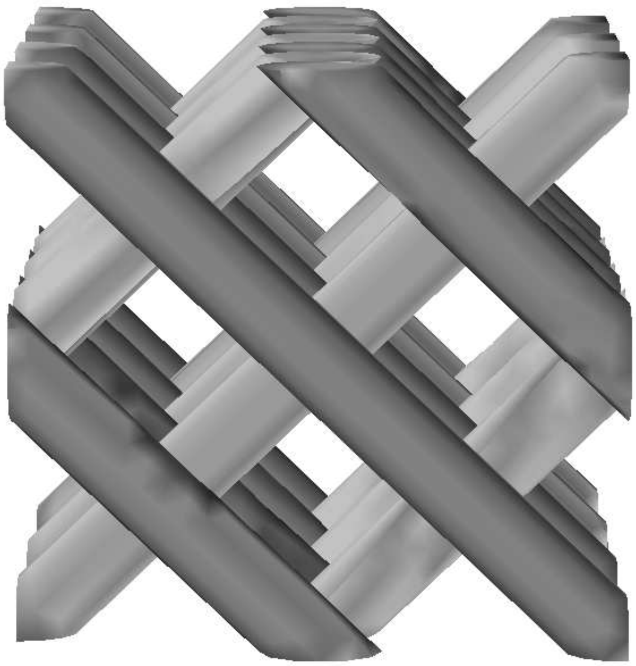

Figure 6.1: SMRX geometry.

It consists of a series of solid crossing tubes, placed inside a rectangular tubular reactor (see Figure 6.1). In this work, we will focus our attention on this static mixer and use the experimental results of van Dijck et al. [74] as a validation for the numerical investigation.

Due to rather complex flows and geometries, only few 3D numerical simulations in static mixers were performed in the past. The first one was in 1992 on a Kenics static mixer by Gyenis and Blickle [75] using stochastic simulations of steady state particle flows. The simulations that followed were all based on macroscopic momentum balance methods like finite-element, finite difference, or finite volume methods. Using the finite volume package FLUENT^{TM}, Bakker and LaRoche [76] also studied flow and mixing in a Kenics static mixer. Later on, using RheoTek's finite-element program POLY3D^{TM}, Bertrand et al. [77] looked

at residence time distribution in Ross Engineering's LPD and ISG static mixers for Newtonian and power-law fluids. In the same way, Tanguy et al. [78] and Mickaily-Huber et al. [56] investigated flow and mixing in the complex SMRX static mixer. Recently, Avalosse and Crochet [79] studied mixing of Newtonian and power-law fluids in a series of Kenics mixers using a finite-element method. A close review of these previous articles clearly shows that the major problem of the momentum balance methods is to generate a satisfactory body-fitted grid or mesh that does not require too much memory. Briefly stated, they have high memory requirements per grid element and as a consequence are quite rapidly limited by the available computer resources. Furthermore, complex geometries like the SMRX can lead to numerical inaccuracy due to poor body-fitted meshes, especially for the pressure field (see section III).
In this chapter we intend to show that the lattice-Boltzmann method [28, 22, 80, 12] can be used successfully as an alternative approach to traditional macroscopic momentum balance methods for computing fluid flows in complex geometries such as the SMRX static mixer.

6.3 The Galerkin Finite-Element method

In this section we present the basic fundamentals of the finite-element method (FEM). A description of the lattice-Boltzmann method (LBM) can be found in the introduction of this thesis. The aim is to underline the conceptual differences between both methods. For more exhaustive reviews, we refer to the book of Cuvelier et al. [81] for FEM and Refs. [28, 22, 80, 12, 16] for the lattice-Boltzmann method.
On a macroscopic scale, flow of an incompressible fluid in a given geometry Ω can be described by the classical Navier-Stokes equations [2]

$$\rho(\frac{\partial \mathbf{v}}{\partial t} + \mathbf{v}\cdot\nabla\mathbf{v}) + \nabla\cdot\sigma + \nabla p = \mathbf{f}, \tag{6.1}$$

$$\nabla\cdot\mathbf{v} = 0 \tag{6.2}$$

where ρ is the fluid density, $\mathbf{v}$ is the velocity, p is the pressure and $\mathbf{f}$ is a body force, e.g. the gravitational force. The stress tensor σ is a function of the rate-of-strain tensor $\dot{\gamma} = \frac{1}{2}(\nabla\mathbf{v} + (\nabla\mathbf{v})^T)$, through a rheological model:

$$\sigma = -2\eta\dot{\gamma} \tag{6.3}$$

where, depending on the rheological model chosen, the fluid viscosity η could be a function of $|\dot{\gamma}|$ (non-Newtonian models) or simply equals to the Newtonian viscosity μ.
The finite-element method for solving fluid flow dynamics makes use of variational calculus which allows to transform a set of partial differential equations (in our case, the Navier-Stokes equations) into a system of linear algebraic

equations. For the sake of simplification and concision, let us consider the following differential equation

$$L\mathbf{u} = \mathbf{f}, \tag{6.4}$$

where $\mathbf{u}$ is the unknown function of the problem (in our case, there are 4 degrees of freedom: the three components of the velocity and the pressure) and L represents the differential operator related to the partial differential equation treated.

The first step in FEM is to multiply the differential equation by a test function ψ chosen in an appropriate vectorial space and to integrate the resulting equation in the studied domain Ω. We subsequently obtain the following equation

$$\int_{\Omega} \psi(L\mathbf{u} - \mathbf{f})d\Omega = 0. \tag{6.5}$$

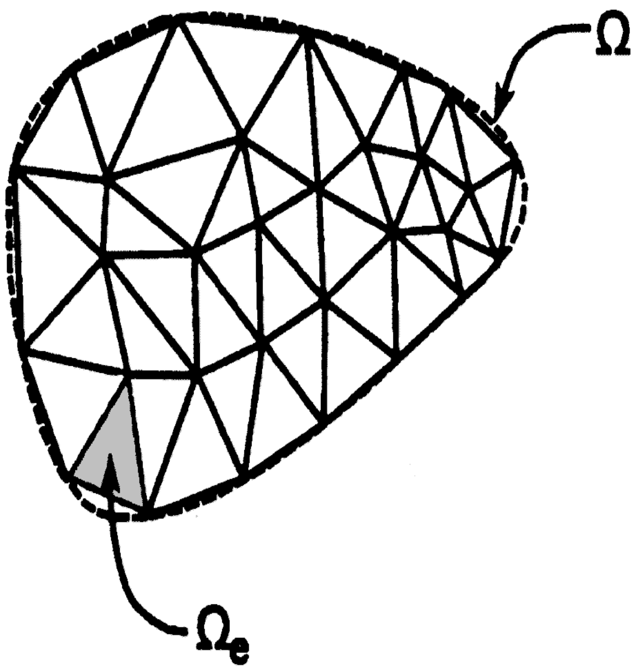

Figure 6.2: Discretization of the domain Ω by a set of triangular elements Ω_e.

In order to solve equation 6.5 the domain Ω is split up in many sub-domains Ω_e called finite elements (Figure 6.2). Each element is made of geometrical nodes and is constructed in such a way that it fits as good as possible the geometry Ω and respects a certain continuity with its neighbors. The element set is called a mesh. Normally, the quality of the solution is improved as the mesh resolution is increased. The repartition and the number of nodes determine the type of element to be used. Briefly stated, there are triangular and quadrilateral elements in 2D and tetrahedral and hexahedral elements in 3D. Due to their flexibility, triangular and tetrahedral elements are more suitable to fit non-trivial geometries. Especially in 3D, mesh creation requires the use of automatic and robust mesh generators. If we now apply equation 6.5 to each element Ω_e, we get the following equation,

$$\sum_{i=1}^{ne} \int_{\Omega_e} \psi_i (L\mathbf{u} - \mathbf{f}) d\Omega_e = 0, \tag{6.6}$$

where ne is the total number of elements. Then, in each domain element, an approximation of the unknown function is introduced in the following form:

$$\mathbf{u} = \sum_{j=1}^{nn} \phi_j \mathbf{u}_j \tag{6.7}$$

where nn is the number of nodes in the element, $\mathbf{u}_j$ is the value of the unknown function at node j and ϕ_j is called a basis function. A Lagrange polynomial is usually taken as basis function.
Combining equations 6.6 and 6.7 and using the Galerkin method, which consists simply of taking $\phi_i = \psi_i$, we obtain

$$\sum_{i=1}^{ne} \sum_{j=1}^{nn} (\mathbf{u}_j \int_{\Omega_e} \phi_i L \phi_j d\Omega_e - \int_{\Omega_e} \phi_i \mathbf{f} d\Omega_e) = 0 \tag{6.8}$$

In order to lower the order of differentiation of the first integral in the previous equation, integration by parts (Green's formula) can be performed. This usually leads to an expression where Neumann type boundary conditions can be introduced [81]. It is important to note that to avoid the definition of different sets of basis functions for each element, each integral is actually first evaluated in a reference element with fixed geometry.
Finally, equation 6.8 leads to an overall sparse matrix system of the form

$$\mathbf{A}\mathbf{u}_j = \mathbf{b} \tag{6.9}$$

which can be solved using a LU decomposition or by means of iterative algorithms. The latter usually requires preconditioning.
In the context of the Navier-Stokes equations, it is important to introduce a few extensions. Since the pressure is related to the velocity, the Uzawa algorithm [82] can be implemented in order to decouple the pressure and the velocity. This iterative algorithm is based on the penalization of the incompressibility constraint through,

$$p^{l+1} = p^l + \alpha \nabla \cdot \mathbf{v}^{l+1} \tag{6.10}$$

where α is the descent parameter, p^l and $\mathbf{v}^l$ are the pressure and the velocity at iteration l, respectively.
The inertial term of the Navier-Stokes equations is non-linear. For low Reynolds number, it can be added to the right hand side of the matrix system. It is then evaluated by means of the velocity solution found at the previous iteration using the Picard algorithm [9]. When the Reynolds number is rather high (laminar-transient regime), linearization of the Navier-Stokes equations using the Newton-Raphson algorithm is required for convergence. For non-Newtonian fluid flows, the problem becomes non-linear in shear rate. In this

case, a Lagrangian augmented method is used that allows to decouple the treatment of the non-linearity from the pressure and the velocity fields [83].
It is obvious that FEM and LBM are two very different numerical approaches. FEM is based on approximations of flow equations that are governed by basic physical conservation laws on a *macroscopic* scale, whereas LBM is based on evolution rules which obey the same conservation laws on a *mesoscopic* scale. In LBM the physical evolution rules are discrete while in FEM methods the discretization is performed on the level of the macroscopic flow equations.

6.4 Simulation results

In this section we present a detailed comparison between the two methods using the SMRX test case. We compare the simulation results such as the velocity and the pressure along the SMRX mixer of both methods, as well as their computational requirements. The experimental results of van Dijck et al. [74] for the pressure drop at different flow rates are used to validate both numerical methods. The simulation parameters correspond to those used in these experiments (Table 6.1). The rectangular reactor consists of an inlet section, followed by one or two mixer elements and an outlet section.

Fluid flow properties	
Newtonian viscosity	1.46 Pa.s
Fluid density	1053 kg/m^3
Flow rate	$0-250\ l/h$
Reactor dimensions	
Height/width	8.5 cm
Length	17.0 cm (1 SMRX) 25.5 cm (2 SMRX)
Mixer dimensions	
Height/width/length	8.5 cm
Number of tubes per SMRX	21

Table 6.1: The fluid flow properties and the SMRX dimensions adopted from van Dijck's experiments and used to validate the simulations.

Concerning the FEM simulations, the first step is to generate a satisfactory mesh of the SMRX geometry. Generating a body-fitted mesh for such a complex geometry is quite a challenge [56]. Using the mesh generator included in the commercial I-DEAS package [78], we succeeded in creating two adequate meshes (with adequate we just mean meshes that look satisfactory) made of roughly 35,000 and 45,000 tetrahedral elements (Figure 6.3). However, even with this powerful software, some problems occurred at certain crossing points between the tubes. To overcome these problems, 4 tubes with the same diameter as the mixer tubes were placed perpendicular to the flow direction at the

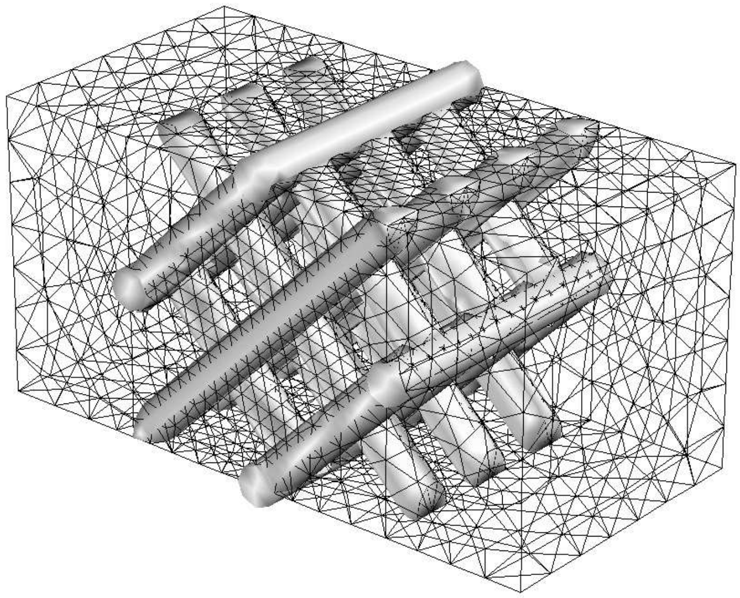

Figure 6.3: Finite-element mesh for the SMRX reactor (35000 elements).

crossing points. It can be argued that they have minor influence on the flow since there are located in dead or low velocity zones. In our meshes, we used two types of tetrahedral elements, namely the P_1^+-P_0 elements (called linear elements) and the P_2^+-P_1 elements (called quadratic elements). These element types satisfy the so-called Brezzi-Babuska condition [84], a theoretical compatibility condition which ensures reliable computations, especially for the pressure. The P_1^+-P_0 linear element is an 8 nodal points element where the velocity is approximated linearly, the pressure is taken to be constant and extra degrees of freedom are added at the middle of each face to satisfy the Brezzi-Babuska condition. The P_2^+-P_1 quadratic element is a 15 nodal points element where the velocity and pressure are approximated quadratically and linearly, respectively, and extra degrees of freedom are added at the middle of each face and edge and also at the centroid. We refer the reader to the paper of Bertrand et al. [85] for more details. The flow simulations were performed on one RISC6000 77 MHz node of an IBM 9076 SP2 with 512 MB of nodal memory using POLY3D^{TM}. The boundary conditions are summarized in Table 6.2. The memory space usage was 129 MB, 480 MB, and 165 MB respectively for the 35,000 element P_1^+-P_0 and P_2^+-P_1 meshes and for the 45,000 element P_1^+-P_0 mesh. We did not consider simulations on a 45,000 element P_2^+-P_1 mesh, because the simulation results obtained on the 35,000 element P_2^+-P_1 mesh were quite satisfactory, as will be shown in the next section. The computational time was 40 CPU min, 190 CPU min and 57 CPU min respectively.

In LBM the geometry is represented on a uniform Cartesian grid. Each grid point is marked as a solid point when it belongs to an obstacle and otherwise it is marked as a fluid point. To obtain a satisfactory discretization of the SMRX element we have used lattices of dimension 112x56x56 and 224x112x112 grid points, based on a tube radius discretization of 4 and 8 grid points respectively. Tube radii of 4 and 8 grid points respectively are based on previous studies using the lattice-Boltzmann method (see for example Refs [40, 41]). Compared to FEM, the grid generation is much easier for LBM, especially due to the uniformity of the lattice. Of course, it must be emphasized that the uniform nature of the lattice has its own limitations. For example, in this specific SMRX case the number of grid points for representing the inlet and the outlet sections is of the same amount as the number of grid points for representing the mixer element itself. A grid refinement based on a coarser grid resolution for the inlet and the outlet sections and a finer resolution for the element discretization could be very useful. However, the formulation and application of LBM schemes based on non-uniform lattices is still an important research topic (see for example addendum A and Refs. [69, 29, 86]).

Boundary	**FEM**	**LBM**
Inlet	v_x using a quasi-parabolic velocity distribution given by a series approximation [87]; $v_y = v_z = 0$	Periodic
Outlet	$-p + \rho\frac{\partial v_x}{\partial x} = 0$; $v_y = v_z = 0$	Periodic
Solid walls	$v_x = v_y = v_z = 0$	Bounce-back rule

Table 6.2: Boundary conditions used in both methods (v_x, v_y and v_z are the components of the velocity vector and the flow is in the x direction).

The boundary conditions used in the LBM simulations are summarized in table 6.2. Notice that the flow boundaries and especially the no-slip boundaries can be implemented quite easily due to the particle based approach. The in- and outlet are periodic and the flow is driven by a local body force. The use of periodic boundaries is based on the assumption that the velocity profiles at the in- and outlet are fully developed (the inlet and outlet sections are long enough to guarantee that). More sophisticated pressure and velocity boundaries can be used when these conditions are not valid (see e.g. Ref. [35]). The solid walls have been modeled by the bounce-back boundary condition; the velocities of the particles that reach the wall are simply reversed. The bounce-back rule generates a no-slip boundary which is located somewhere between the solid and the adjacent fluid nodes (see chapter 3 and Refs. [38, 55]). As the grid resolution is increased, the agreement between the actual geometry and the locations of the no-slip boundaries is improved. Careful determination of the appropriate lattice dimensions for a certain simulation is therefore very important. The flow rate in the simulations is controlled by the magnitude of the body force and the viscosity is tuned by the relaxation parameter.
The LBM simulations were performed on a Parsytec CC parallel machine with 128 MB memory per node (133 MHz PowerPC 604). The total memory space usage was 50 MB and 400 MB for the 112x56x56 and 224x112x112 lattice respectively. The computational time on one node of the parallel machine was

Mesh	**FEM**	**LBM** on 1 node	**LBM** on 16 nodes
I	40 min/ 129 MB	110 min / 50 MB	10 min / 50 MB
II	57 min/ 165 MB	-	-
III	190 min/ 480 MB	3300 min / 400 MB	210 min / 400 MB

Table 6.3: Computational requirements of FEM and LBM for different grid/mesh resolutions. In the case of FEM the meshes I, II and III denote the 35000 P_1^+-P_0 element mesh, 45000 P_1^+-P_0 element mesh and the 35000 P_2^+-P_1 elements mesh, respectively. In the case of LBM the 112x56x56 and 224x112x112 lattices are meant by I and III, respectively. We have included the CPU times and the total memory requirements of both methods. As both methods are quite different, it does not make sense to compare the computational requirements of both methods obtained on the various mesh/grid types. However, with additional information concerning the accuracy obtained on the different mesh/grid types one can still gain some insight in the computational requirements of both method for a certain accuracy range. In the next section, we will see that for FEM accurate results are only obtained on the type III mesh, whereas the results obtained with LBM on the type I grid is quite accurate.

110 CPU min and 3300 CPU min (estimated, because this simulation could not be executed on a single node of the machine due to memory constraints) respectively.

However, the final LBM simulations were performed on 16 nodes of the parallel machine and then the computation time was 10 CPU min (parallel efficiency [88] of 0.7) and 210 CPU min (parallel efficiency close to 1) for the two grid resolutions. The computational requirements of both methods are summarized in Table 6.3. It is evident that the sequential computation time of the fine grid LBM simulations is quite high. The reason is that although the computation time for each LBM iteration increases linearly with the number of lattice points, the number of time iterations to reach the steady state depends quadratically on the lattice spacing (provided that the relaxation parameter is kept constant). Notice that in LBM a complete time dependent flow is simulated (see chapter 4 for details) in contrast to FEM where in our simulations the stationary Navier-Stokes equations are solved.

Figures 6.10.a to 6.10.f show the velocity at three slices along the reactor. We conclude that qualitatively there is a good agreement for the local velocities obtained by the two methods. We have to underline the fact that the software used to render the FEM contour plots uses only the geometrical nodes (vertex nodes), leading to a loss of accuracy (especially when simulations are performed with P_2^+-P_1 element) and to coarser contour plots than the LBM. Nevertheless the agreement is good. Furthermore, it is clear that the hot spots in the velocity profiles obtained by both methods agree with each other.

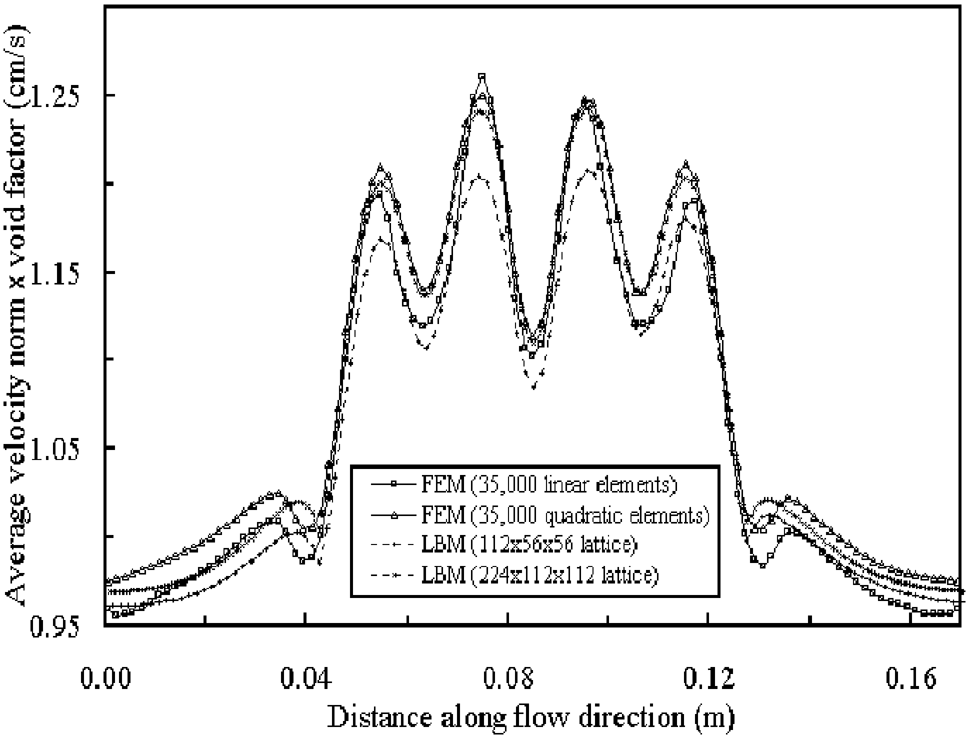

Figure 6.4: Average velocity norm times void factor along the reactor (flow rate is 250 l/h).

The average of the norm of the velocity along the reactor multiplied by the void factor, is shown in Figure 6.4. The reason for multiplying by the void factor is to avoid small fluctuations due to the 4 tubes added in the cross flow direction in the FEM mesh. In this figure we have included the results obtained on the two LBM grids and on the two types of FEM meshes (the P_1^+-P_0 and P_2^+-P_1 elements, respectively). The qualitative shape of the profile mimics the distribution of the void space along the reactor, as one would expect. For FEM the average and maximum difference between the velocity field of the two meshes is approximately 1.7% and 4.2%, respectively. For LBM we have found an average and maximum difference of around 1.6% and 3.1% for the velocity field, respectively. Moreover, we clearly see that there is a very good agreement (maximum difference 1%) between the solution obtained on the fine LBM grid and the P_2^+-P_1 FEM mesh.

The pressure along the reactor, which is much more sensitive to numerical accuracy than the velocity [56], is depicted in Figure 6.5. Here we see that there are clear differences in the pressure field obtained on the two FEM meshes, despite the good agreement found for the velocity field. The difference in pressure drop between the P_1^+-P_0 and P_2^+-P_1 meshes is around 44%. The difference between the LBM simulations however is around 7.6%. Moreover, it is evident that there is a very good agreement for the average pressure along the reactor between P_2^+-P_1 FEM simulations and the LBM simulations on the fine grid. The difference in

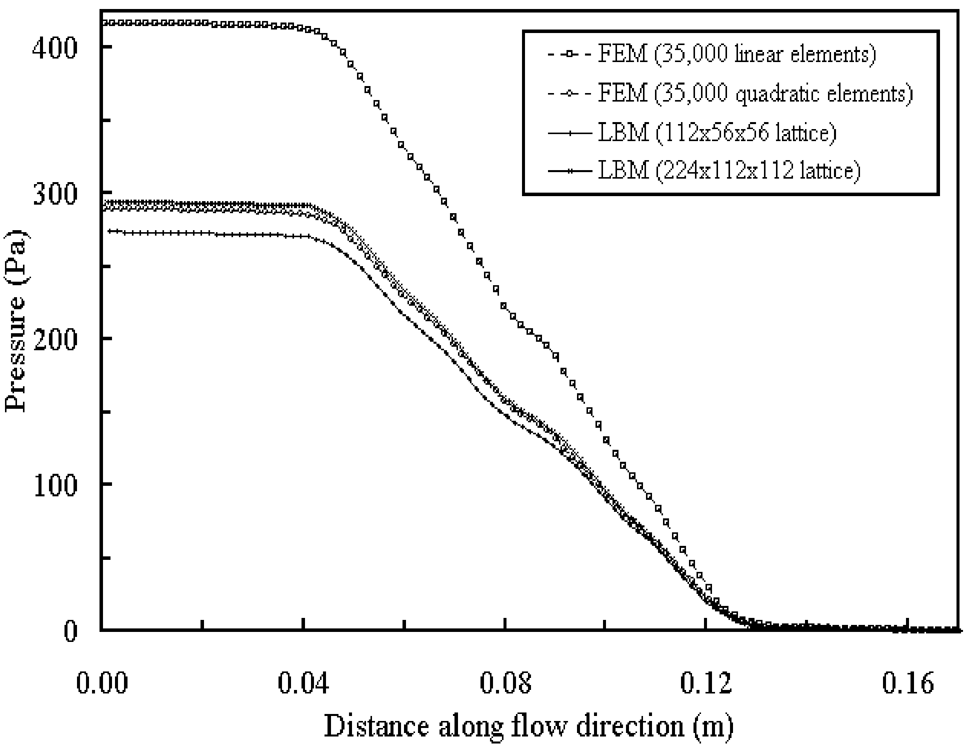

Figure 6.5: Pressure along the reactor (flow rate 250 l/h).

pressure drop is around 1.6% and also the small fluctuations in the mean pressure along the SMRX element zone are similar.

The pressure drop as a function of the flow rate is shown in Figure 6.6. Here we have included the results obtained by the two methods on the different grids and meshes. We see that for FEM there is a large discrepancy between the P_1^+-P_0 and the P_2^+-P_1 meshes for all flow rates. Even for increasing number of elements the results obtained by the P_1^+-P_0 are not that accurate. An approximately 30% increase in the number of P_1^+-P_0 elements leads to an improvement in the pressure drop by around 8% only, which is normal for such type of element. The LBM results on the two grids are quite close to each other. We clearly see that indeed the FEM and the LBM solutions converge to each other as the grid or mesh-element type is refined. These results are also good in agreement with the experimental data of van Dijck et al. The error in the experimental data is approximately 7% [74]. For low flow rates the simulations are in the estimated error range of the experimental data. For higher flow rates the simulations overestimate the pressure drop. The maximum difference between simulations and experiment is around 15%. These differences may be caused by experimental uncertainties in the calibration of the flow rate and in viscosity measurements. Notice that in both simulations, we have assumed that the fluid is Newtonian, whereas from experimental measurements it was evident that the fluid is not purely Newtonian [74]. Furthermore, more detailed experimental measurements (at least more data points) are required in order to judge the ac-

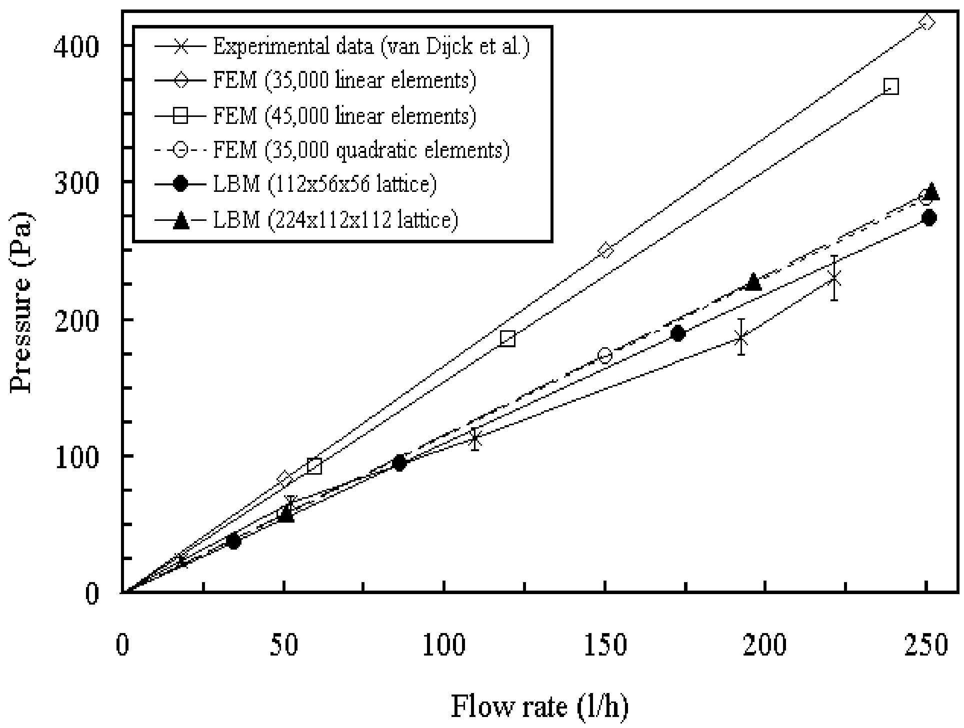

Figure 6.6: Pressure drop versus flow rate.

tual cause of the slight disagreement between simulations and experiments.

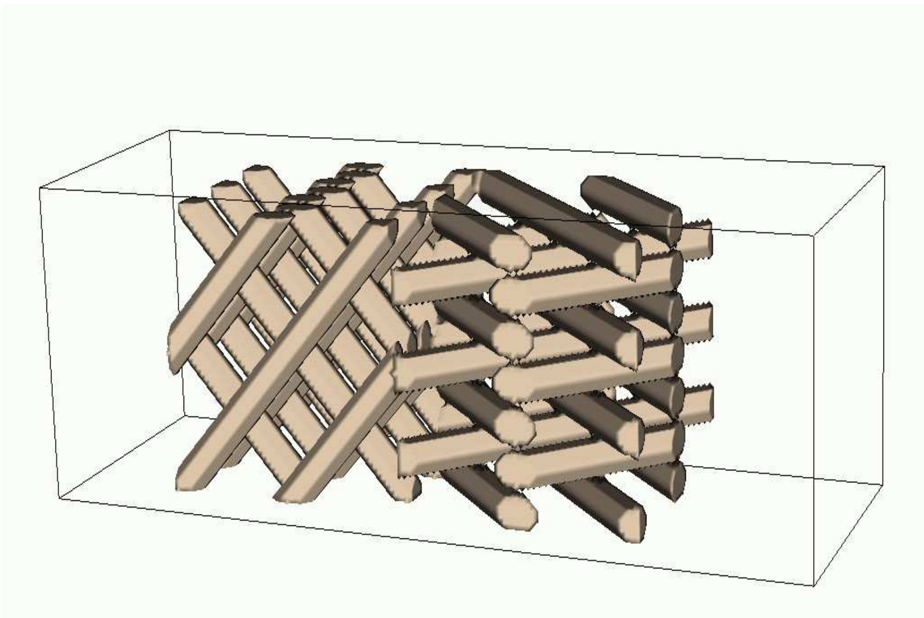

Figure 6.7: LBM discretization of two SMRX reactors (tube radius of 4 lattice points).

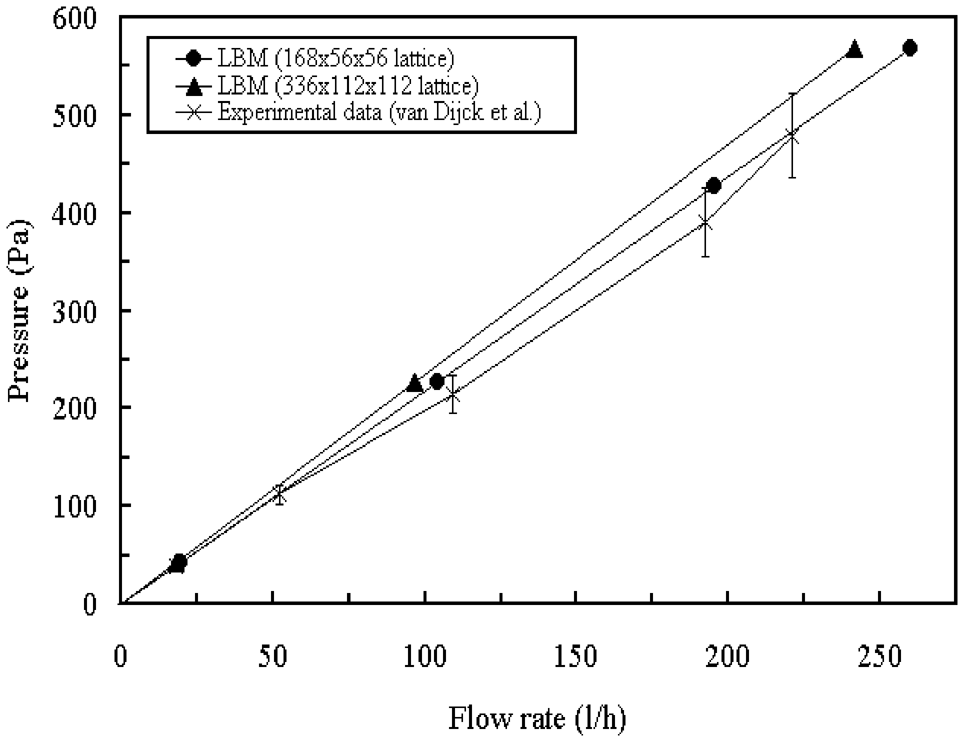

Figure 6.8: Pressure drop versus flow rate for a two SMRX elements reactor (flow rate is 250 l/h).

We have also simulated fluid flow in a reactor consisting of 2 SMRX elements with the LBM. The geometry of this reactor is shown in Figure 6.7. In this setup the second SMRX element is rotated 90 degrees. The results for the pressure drop on the different grids are shown in figure 6.8. We clearly see that also in this case there is a good agreement between simulation and experiment. Here we found a deviation in the order of 15% between simulation and experiment. This case could not be simulated using FEM due to memory requirements. For LBM, the total amount of memory usage depends linearly on the number of mixer elements. In principle a reactor consisting of more mixer elements (which corresponds to the actual configuration in industrial reactors) can be simulated on the full domain of the parallel machine.

From all these results, it appears that the FEM has more difficulties in predicting the right pressure drop. With the FEM, a too coarse mesh will most probably lead to a poor estimate of the pressure field, despite a relative good estimate of the velocity field. Especially for the current test case, we argue that a P_2^+-P_1 type of element is absolutely required to get a satisfactory estimate of the pressure field.

Moreover, the LBM uses roughly 10 times less memory than the FEM to reach a similar accuracy since the solution given by the LBM coarse grid reaches already a satisfactory precision. Although the simulations were not executed on the same computer, it appears also that the LBM coarse grid simulation requires roughly the same computational time (on a sequential machine) compared to the FEM fine mesh simulation. However, the computational time required by the LBM fine grid simulation shows a drastic increase compared to the coarse grid simulation.

6.5 Methodological Comparison

In the previous section, we have demonstrated that LBM is indeed efficient for simulating a single-phase, isothermal, incompressible and laminar fluid flow through an SMRX reactor. In this section, we will discuss the possibilities to simulate more complicated flow problems by the two methods. Also more practical aspects like for example code development and memory usage will be considered. Table 6.4 summarizes the different aspects.

	FEM	**LBM**
Code implementation	long	easy
Memory Usage (Number of “elements”/MB)	P_1^+-P_0: 274 P_2^+-P_1: 74	6800
CPU Time (∼ (number of “elements”)^X)	$X = 1.4$	$X = 1.7$
Parallelization	not trivial	inherent locality
Local mesh refinement	available	in development
Transient flow	available	inherent
Heat transfer	available	research topic
Mass transfer	available	available
Multi-phase	not as straightforward as in LBM	research topic
Non-Newtonian/elastic fluid rheology	available	research topic
Turbulence	partially successful	partially successful

Table 6.4: A methodological comparison between FEM and LBM.

The FEM is in use in many commercial CFD packages like POLY3D^{TM}, POLY FLOW^{TM} or FIDAP^{TM}. This in contrary to the LBM, which is a rather new method and it is still in its development phase. The only commercial LBM code at the moment is POWERFLOW^{TM} developed by EXA Corporation. The implementation of a LBM code is quite straightforward, whereas the implementation of a FEM code is long and tedious (a matter of years). For this specific application, the LBM can reach the same level of accuracy with a memory usage roughly 10 times lower than the FEM. In Table 6.4, we have included the average requirements (at least for the codes used) for both methods in terms of elements or grid cells per MB of memory, although the nature of one ”element” differs from one method to the other and therefore these numbers should be interpreted with care. Nevertheless, it can provide some insights in the amount of memory needed for a specific application given the number of elements or grid points which are required for a satisfactory discretization.

As we mentioned earlier, it was possible for our test case to achieve the same level of accuracy using roughly the same computational time. However, the computational time as a function of the number of elements or grid cells behaves quite different for both methods. It appears that as the mesh or the grid is refined the computational time as a function of the number of "elements" increases with the power 1.4 for the FEM [78] and 1.7 for LBM as explained below. Notice that in LBM a decrease of the lattice spacing by a factor 2 results into 8 times more lattice points. The lattice spacing is thus proportional to $N^{\frac{1}{3}}$ (N is the number of lattice points) and the number of time steps to reach a steady-state depends quadratically on the lattice spacing [55]. Therefore the total computational time is proportional to $N^{\frac{2}{3}}N \approx N^{1.7}$, which explains the sharp rise in computational time noticed for the LBM fine grid simulations. Nevertheless, the total computational time depends on the problem. Notice that a more efficient relaxation scheme (see chapter 3) may be used to accelerate the convergence of the LBM simulations.

The inherent locality of the update rules in the LBM makes efficient parallelization straightforward (see chapter 5), whereas parallelization of FEM codes may be more complicated especially when implicit methods are used.

Concerning the mesh or grid generation for complex geometries we can make the following remarks. It is obvious that it is much easier to generate a grid for the LBM than to generate a mesh for the FEM. However, recently a new method, the so-called virtual finite-element method (VFEM), has been proposed by Bertrand et al. [89]. This method belongs to the class of Fictitious Domain Methods based on Lagrange multipliers (Glowinski et al. [90]). It allows to impose fictitiously the inner part of the geometry using kinematic constraints introduced into the mathematical formulation by means of Lagrange multipliers. Then only one volumetric mesh representing the enclosure without its internal parts (in our test case, the reactor without the SMRX element) has to be generated. To gain insight in the performance of LBM compared to the promising VFEM approach, we have performed a preliminary comparison between LBM and VFEM. The results for the pressure drop as a function of the flow rate are shown in Fig. 6.9. We clearly see that there is a good agreement between LBM and VFEM. However, in return for the gain in terms of mesh generation, a much longer computational time was observed to reach equivalent convergence criteria. The VFEM method allowed us to simulate the SMRX test case without the introduction of the 4 tubes in the cross flow direction as mentioned earlier and it may be really useful in cases where usually remeshing is required or meshing is impossible by conventional methods. Otherwise, in classical 3D FEM meshing, only the use of tetrahedral elements allows the creation of a suitable mesh for geometries like our test case. Fortunately, mesh refinement techniques are fully available for the FEM, which support mesh refinement only where needed,

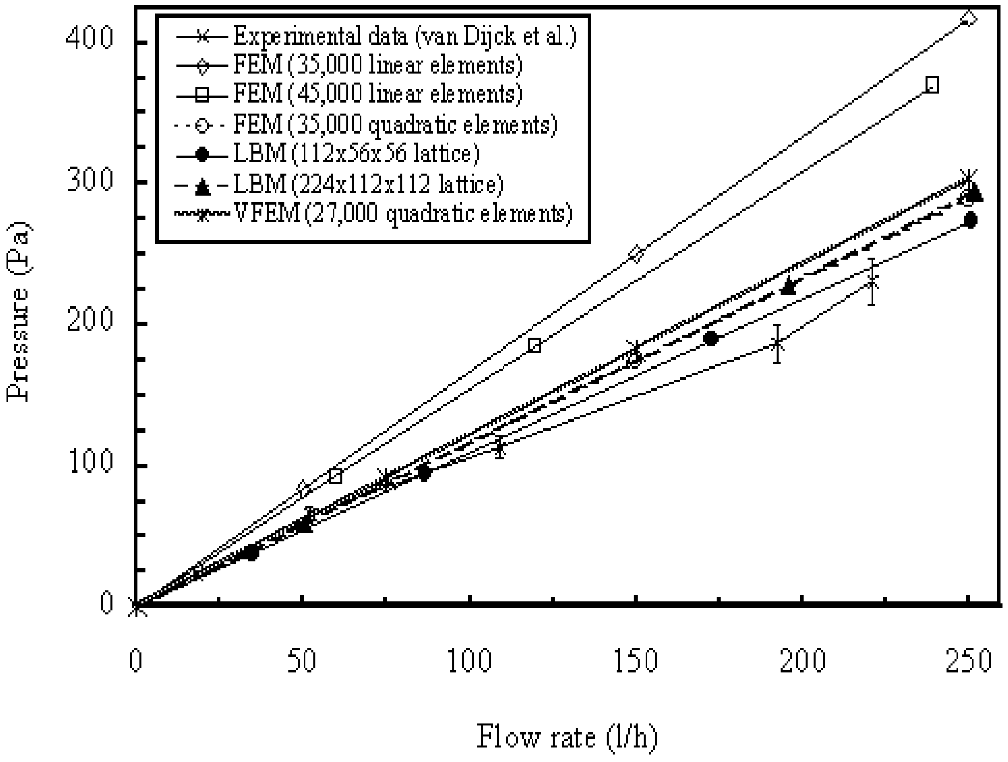

Figure 6.9: Preliminary comparison between the VFEM, the conventional FEM, the LBM and the experimental data (Memory usage VFEM: 413 MB).

whereas it is still a research topic for the LBM. Recently some schemes based on non-uniform grids for LBM have been proposed (see addendum A and Refs. [29, 86]).

Simulation of transient flows is a fully available feature for both methods and it is even inherent in the LBM. Heat transfer, mass transfer, non-Newtonian and elastic fluid rheology are other features that have already been studied for many years by using FEM, but are quite recent developments in LBM [80, 91]. Extensions of both models to deal with turbulence have been studied for several test cases (see e.g. [92]). It is however important to notice that the complex phenomena which are inherent to turbulence makes both methods only partially successful. However, simulation of multi-phase flow and suspension flow using FEM is not as straightforward as in LBM. The LBM method appears to be suitable for modeling these complex flows in some hydrodynamic regimes as demonstrated by e.g. Grunau et al. [93] and Ladd [40, 41]. This discussion clearly suggests that both methods are good in their own respect and also that there may be developments in the future which may change the range of tractable applications for both methods.

6.6 Conclusions

Our results based on flow in a SMRX reactor show a good agreement between FEM simulations, LBM simulations, and experimental measurements. This suggests that the LBM is an accurate method for flow through complex geometries. It appears that the LBM is less memory consuming and uses computational times comparable to the FEM (for the same accuracy of the simulations), although there may be cases where the FEM method is more efficient, e.g. due to the uniform nature of the LBM grids. However, the execution times of the LBM methods show a sharp increase on very fine meshes. We discovered also that the LBM shows similar accuracy between pressure and velocity fields, whereas the FEM could exhibit a rather good estimate of the velocity field combined with a bad estimate of the pressure field due to mesh coarseness. Clearly, the choice between the two methods relies on the type of problem to solve, the computer resources available and time. For instance, starting to build a code from scratch, having a problem requiring a lot of memory and/or parallelization and/or dealing with multi-phase, the LBM will turn out to be a faster and easier method. On the other hand, having a flow problem involving heat transfer and/or non-Newtonian and elastic fluid rheology, the FEM would be a better choice. However, as mentioned earlier, the LBM is a rather new method and those features could probably become tractable for LBM in the coming years.

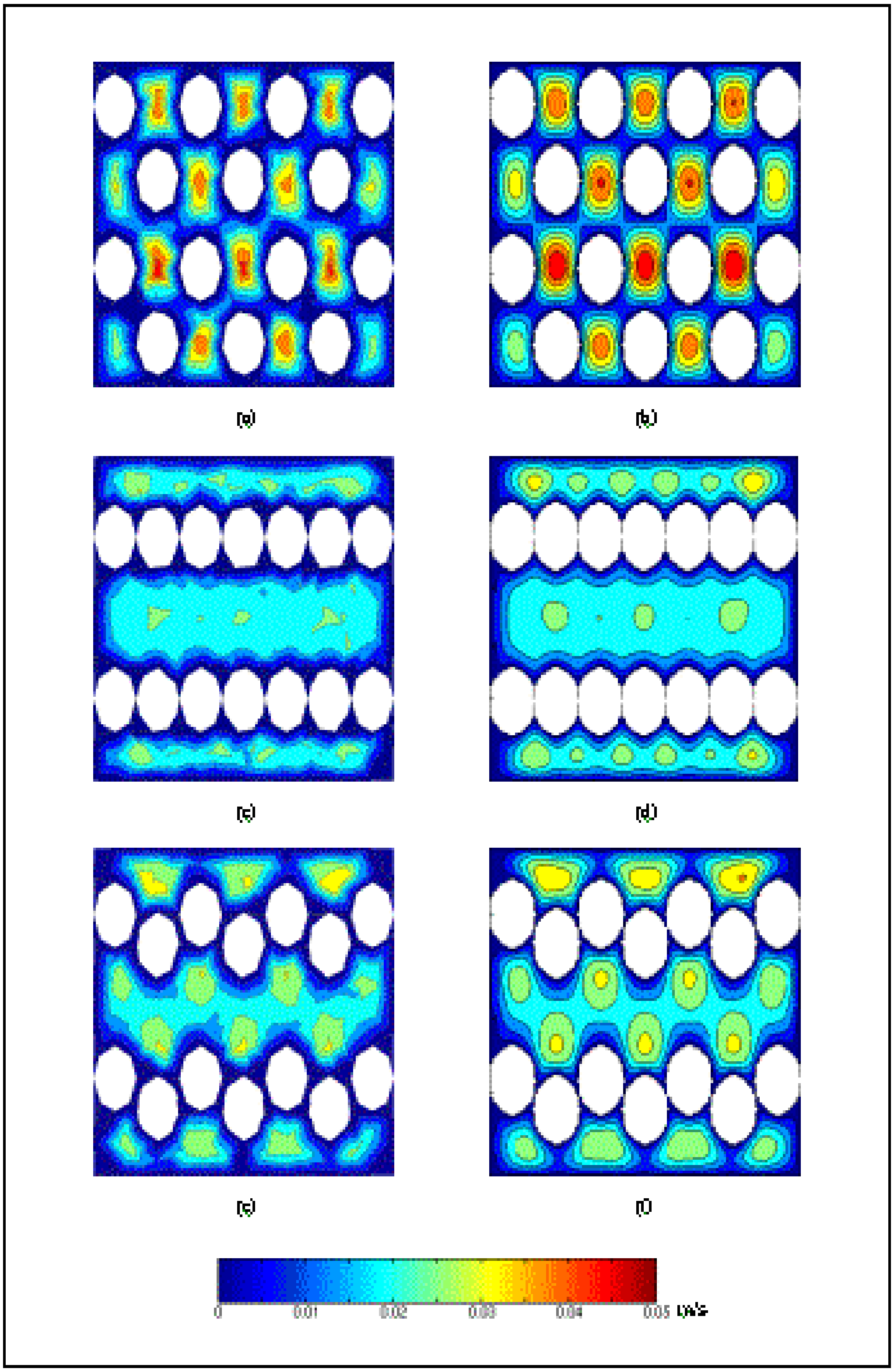

Figure 5

Figure 6.10: Contour plots of the velocity profile at different cross sections in the reactor (a and b at $x = 3.1$ cm, c and d at $x = 6.4$ cm, e and f at $x = 6.8$ cm where $x = 0$ is at the beginning of the static mixer element) for FEM (a, c and e) and LBM (b, d and f) simulations (finest meshes and flow rate is 250 l/h).

Chapter 7

Hydraulic Permeability of Fibrous Media

7.1 Introduction

In the previous chapter we have demonstrated that the Lattice-Boltzmann method is a versatile tool for simulating fluid flow in realistic 3D geometries. In the remainder of the thesis we use LBM to study hydrodynamic properties of disordered porous media. We focus on porous media made of fibers.
Fluid flow in porous media plays an important role in a wide variety of technical and environmental processes, such as oil recovery, paper manufacturing and spread of hazardous wastes in soils. The single-phase creeping flow through a porous substance is well described by Darcy's law [94, 95] which can be written in the form

$$\mathbf{q} = -\frac{k}{\nu}\nabla p, \tag{7.1}$$

where $\mathbf{q}$ is the fluid flux through the medium, ν and p are the kinematic viscosity and the pressure of the fluid, respectively, and k is the permeability coefficient that is a measure of the fluid conductivity through the porous medium. It depends on the geometrical properties of the medium.
Determination of the permeability, k, for each particular substance is a long standing problem. The experimental methods that are currently used are based on sophisticated approaches, which utilize *e.g.* mercury porosimetry, electrical conductivity, nuclear magnetic resonance or acoustic properties of the medium [96, 97, 98]. Theoretical methods typically rely on analytical models based on simplified pore geometries, which allow solution of the microscopic flow patterns [94], or on more advanced methods that statistically take into account the structural complexity of the medium [94, 95].
Numerical simulations are often used to connect theory with experiments. Realistic three-dimensional flow simulations in complex geometries are however very demanding in terms of computing power. Until recently this approach has been hampered by the necessity of major simplifications in the pore structure or flow dynamics. New techniques based on massively parallel computers and increased single processor capabilities have now made 3D simulations of realistic

flow problems feasible. This development is further augmented by the introduction of the lattice-gas-automaton (LGA) [99, 12] and lattice-Boltzmann (LB) method [21, 28, 46], which have already been applied to a wide class of fluid-flow problems and are particularly useful in complex and irregular geometries [100, 40, 41, 49, 101, 6].
In this chapter * we report on the results of lattice-Boltzmann simulations of creeping flow through various fibrous media and compare them with previous experimental, analytical and numerical results. The aim of this study is three-fold:

- First, we validate the Lattice-Boltzmann results rigorously by direct comparison with analytical, numerical and experimental data for various models of fibrous media with a large variation in geometrical properties (see section 8.2);

- Next, we study the effect of disorder on the hydraulic permeability and make a connection between the permeability and the geometry of the media (see sections 8.2 and 8.3);

- Finally, we study the permeability of *bounded* fibrous media, *cf.* media placed between two parallel plates, as a function of the distance between the parallel plates (see section 8.4). These studies are particularly relevant as many fibrous media in practice are bounded systems.

7.2 Permeability of (dis)ordered fibrous media

7.2.1 Background

For a specific fiber arrangement, the permeability depends on the size and concentration of fibers [102]. It is assumed here that the fibers are uniform in diameter and are long enough such that the logical metric for size is the fiber radius, r. The fiber concentration is characterized by the fiber volume fraction, ϕ. The main objective is then to study the functional behavior of the dimensionless hydraulic permeability, $\frac{k}{r^2}$ as a function of the volume fraction,

$$\frac{k}{r^2} = f(\phi).$$

*This chapter is based on the following publications:

- A. Koponen, D. Kandhai, E. Hellen, M. Alava, A. Hoekstra, M. Kataja, K. Niskanen, P. Sloot, and J. Timonen, 'Permeability of Three-Dimensional Random Fiber Webs', *Phys. Rev. Lett.* , **80**, 716-719 (1998).

- D.S. Clague, D. Kandhai, R. Zhang, P.M.A. Sloot, 'Hydraulic Permeability of (Un)Bounded Fibrous Media Using the Lattice-Boltzmann Method', *Phys. Rev. E*, Accepted for publication.

In the past years several studies have been conducted to explore $f(\phi)$ for various fiber arrangements. These studies were based on analytical, numerical and experimental methods. In this section we present a brief overview of the results. The theoretical approach has been to solve Stokes equation in a unit cell via mathematical methods. Due to several approximations in the analytical models, these results are usually only valid for small fiber volume fractions. For simplicity, the unit cell is often restricted to a circular rod placed at the center of a polygon with periodic boundaries. One of the first analytical expressions has been published by Langmuir in 1942 [103]. His work was based on flow parallel to an array of cylinders (one-dimensional flow) in a circular unit cell. This unit cell greatly simplifies the mathematics. Later, several other studies have been reported in which a square unit cell was used instead of circular unit cells. Alternatively, the cylinders were placed in a square, triangular or hexagonal array arrangement. A general equation for the dimensionless hydraulic permeability, $\frac{k}{r^2}$, in the case of flow parallel to an array of rods was published by Drummond and Tahir in 1984 [104],

$$\frac{k}{r^2} = \frac{1}{4\phi}(-ln(\phi) + K + 2\phi - \frac{\phi^2}{2}), \tag{7.2}$$

where K is a constant depending on the fiber arrangement. From this equation, we clearly see a dominant $\frac{ln(\phi)}{\phi}$ functionality for very small volume fractions. For higher volume fractions polynomial correction terms are included.

A more complicated case which has been studied rigorously, is flow perpendicular to an array of cylinders. Here the flow field is truly two-dimensional. Different analytical expressions have been proposed by several authors during the last years. The most notable is the result of Sangani and Acrivos (1982) for a square array of cylinders [105],

$$\frac{k}{r^2} = \frac{1}{8\phi}(-ln(\phi) - 1.476 + 2\phi - 1.774\phi^2 + 4.076\phi^3). \tag{7.3}$$

In addition to this expression, which is only valid in the dilute limit, Sangani and Acrivos reported a semi-analytical study of the hydraulic permeability of a 2D periodic array of cylinders for the full range of fiber volume fractions [105]. We clearly see that the hydraulic permeability for flow perpendicular to an array of cylinders (higher resistance as expected) is approximately half of the hydraulic permeability of flow parallel to an array of cylinders.

So far we discussed one- and two-dimensional flow in fibrous media. Jackson and James studied the hydraulic permeability of a three-dimensional cubic lattice model. They used the expressions of the permeability of flow parallel to an array of cylinders and perpendicular to an array of cylinders to derive the following results for the cubic lattice model [102, 106],

$$\frac{k}{r^2} = \frac{3}{20\phi}(-ln(\phi) - 0.931 + O(ln(\phi))^{-1}). \tag{7.4}$$

In Ref. [102] it is shown that this equation agrees reasonably well with experimental data for ϕ smaller than 0.25. Another very useful method to predict the

permeability is via the Kozeny-Carman equation, where the permeability is related to the fiber volume fraction and the specific surface area of the media. In the next section we will discuss the Kozeny-Carman equation in more detail.
Besides these theoretical studies, Higdon and Ford recently reported, numerical simulations of the hydraulic permeability of different models of 3D fibrous media using spectral boundary element methods [107] for the full range of fiber volume fractions. Their results will be used and discussed in more detail in the next sections. Other numerical studies include those on fluid flow through random arrays of parallel cylinders and suspension of prolate spheroids [108, 109]. All these efforts neglect the disorder typical of real 3D fibrous media. The work of Clague and Philips [110] on permeability of disordered fibrous media is an exception. They used numerical slender body theory methods to calculate the permeability of 3D disordered fibrous media. However, their study was restricted to dilute systems due to inherent limitations of their numerical approach.
Finally, we stress that a large body of experimental data has been published (see *e.g.* [102] for a comprehensive review). However, despite these numerous experimental, numerical and theoretical studies, permeability characteristics of *three-dimensional disordered* fibrous porous media are still poorly understood. Here we use the lattice-Boltzmann method to calculate the hydraulic permeability for different fibrous media and for a large range of fiber volume fractions.

7.2.2 Description of the fibrous media

The first model of fibrous media that is studied is a 2D periodic array of cylinders (see Fig. 7.1). As stated in the previous section, the hydraulic permeability of this simple configuration has been studied theoretically in detail by Sangani and Acrivos [105]. This problem is a well known and accepted benchmark for fluid flow in fibrous media.
Additionally, we simulated fluid flow through a 3D BCC lattice configuration with periodic boundaries. In the BCC lattice configuration the fibers are placed such that their intersection points coincide with the BCC positions (see Fig 7.2). This simulation cell has been studied numerically by Higdon and Ford [107] for a wide range of solid fractions using spectral boundary element methods.
The main motivation for performing simulations of the periodic array of cylinders and the BCC configuration, is to validate the LBM simulations for a wide range of solid fractions and to determine the minimum number of lattice points that are required for discretising the cylinders such that accurate results are guaranteed. Moreover, these simulation cells will be used in the next section to study in more detail the connection between the hydraulic permeability and the geometry of the medium. In that section we focus on the behavior of the hydraulic permeability as a function of ϕ. Details of the geometry are not explicitly taken into account.
Besides the simulations of flow through ordered fibrous media we studied media where the fibers are placed randomly. We considered two configurations, namely random fiber mats and fibrous media consisting of randomly placed overlapping cylinders.

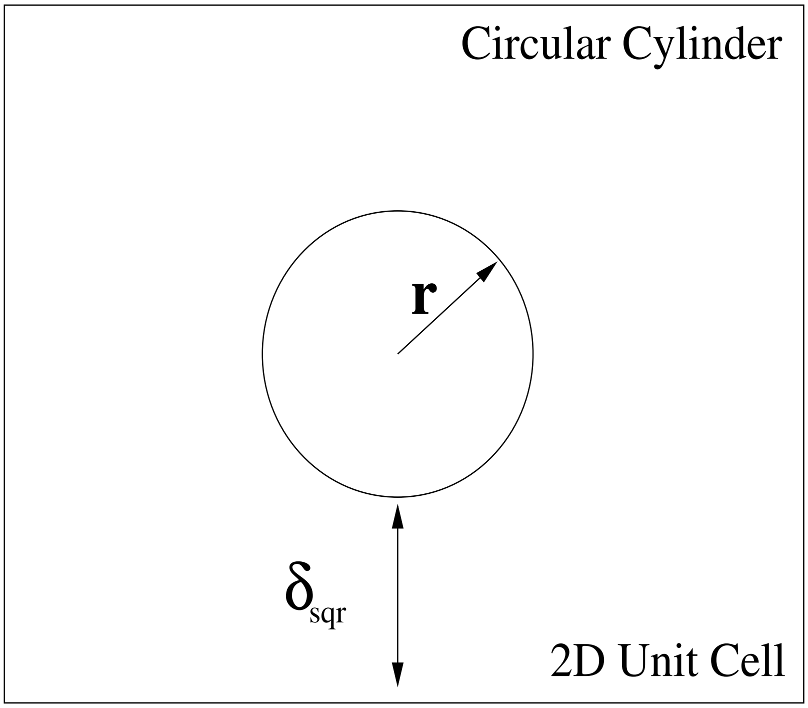

Figure 7.1: A 2D array of periodic cylinders. r is the radius of the cylinder and δ_{sqr} is the half-distance between the cylinders. δ_{sqr} will be used in the next chapter.

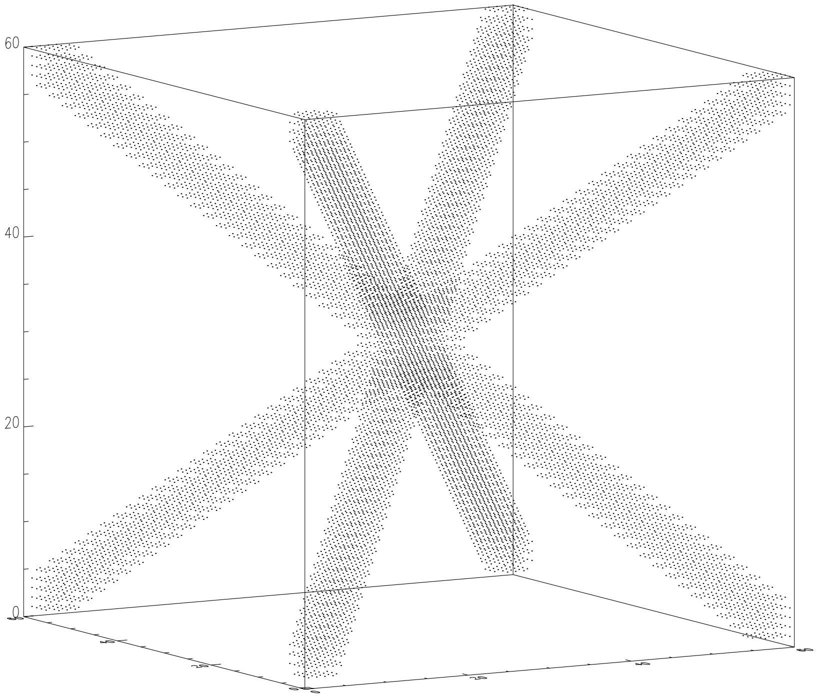

Figure 7.2: A fibrous medium based on the BCC lattice.

The random fiber mats are constructed in discretized space using a recently introduced growth algorithm [57]. Within this algorithm, fiber webs are grown by sequential random deposition of flexible fibers of rectangular cross-section on top of a flat substrate (the xy plane). Each fiber is randomly oriented either in the x or y direction, and is then let to fall in the negative z direction until it makes its first contact with the underlying structure. After this it is bent downwards without destructing the structure, and subject to the constraint

$$|z_i - z_j| \leq F. \tag{7.5}$$

Here z_i and z_j are the elevations of the fiber surface above two nearest-neighbor cells i and j, and F is an effective fiber flexibility. Notice that for long fibers the resulting web structure solid fraction, and contact area of fibers, are determined by F [111]. A large F produces a dense web while small F leads to a more porous structure.

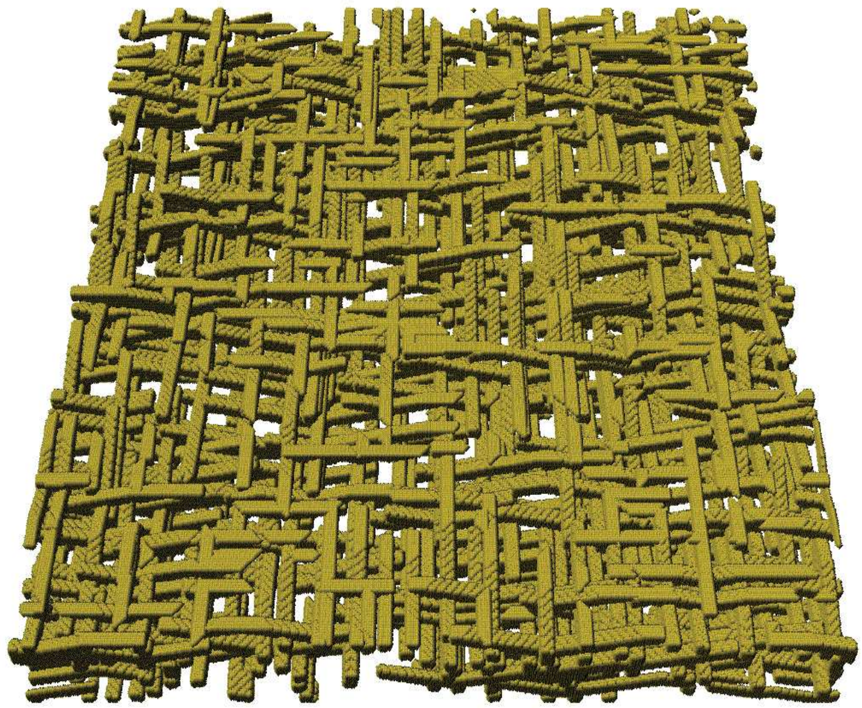

Figure 7.3: A fiber-web sample constructed with the deposition model. The fiber volume fraction of the web is 0.17.

In order to construct structures that are homogeneous in the z direction, the samples used in the simulations were extracted from inner parts of thicker webs. Based on preliminary simulations (data not shown), ten grid layers of void space were then added on the top of samples, and the system was made periodic in all directions. In Fig. 7.3 we show a sample created by this algorithm.

It has been shown that these structures closely resemble that of materials like paper (see e.g. Ref. [112]) and non-woven fabrics (restriction to the x and y directions can be relaxed and does not play an important role here).
Besides the random fiber mat we also studied fluid flow through fully disordered fibrous networks. These networks are built of overlapping cylinders that are placed randomly in a cubic volume and thus their orientation in the z-direction is not constraint by a flexibility parameter [113]. In Fig. 7.4 we show a sample created by this method. In Ref. [113] it has been shown that the generated structures are indeed statistically random. A few years ago, Clague and Philips have studied the permeability of similar disordered media using numerical slender body theory [110]. The main differences between our simulations and that of Clague and Philips is that in their approach the cylinders were not allowed to overlap due to limitations of their numerical method. Therefore their study was restricted to dilute systems, e.g. in the limit of low fiber volume fractions, $0 < \phi < 0.25$.

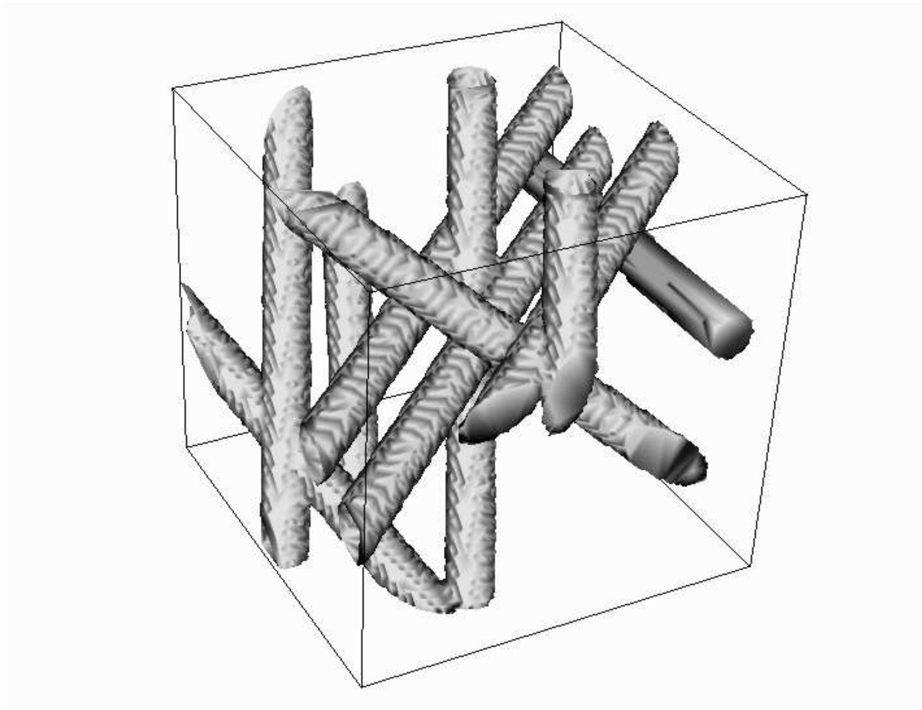

Figure 7.4: Part of a disordered fiber-network sample constructed with the random fiber generator described in Ref. [113]. The fiber volume fraction of the network is 0.1.

7.2.3 Hydraulic Permeability as a function of the fiber volume fraction

In the LBM simulations a uniform velocity field is first initialized. Next, flow is induced by applying a body force on the fluid [49]. This is accomplished simply by adding at each time step a fixed amount of momentum in the direction

of the force to all 'particles' within the void space. Unless stated otherwise the relaxation parameter in the simulations is equal to 1. The permeability of the medium is simply found by computing the total flux **q** through the sample from the stationary hydrodynamic state for a given pressure gradient and fluid viscosity and using Eq. 7.1.
It is well known that the permeability of a porous medium determined by the present method depends on grid resolution. Resolution sensitivity is caused by the bounce-back boundary condition applied to the solid-fluid interface, and by Knudsen effects in small pores (see [12, 46, 49] and chapter 3). These effects are viscosity dependent, and they determine the minimum size of obstacles and pores that can be used in simulations. We will therefore perform a few preliminary simulations to address the resolution effects.

Periodic Array of Cylinders

The hydraulic permeability for a periodic array of cylinders is shown in Fig. 7.5. In this plot we have included the semi-analytical solution of Sangani and

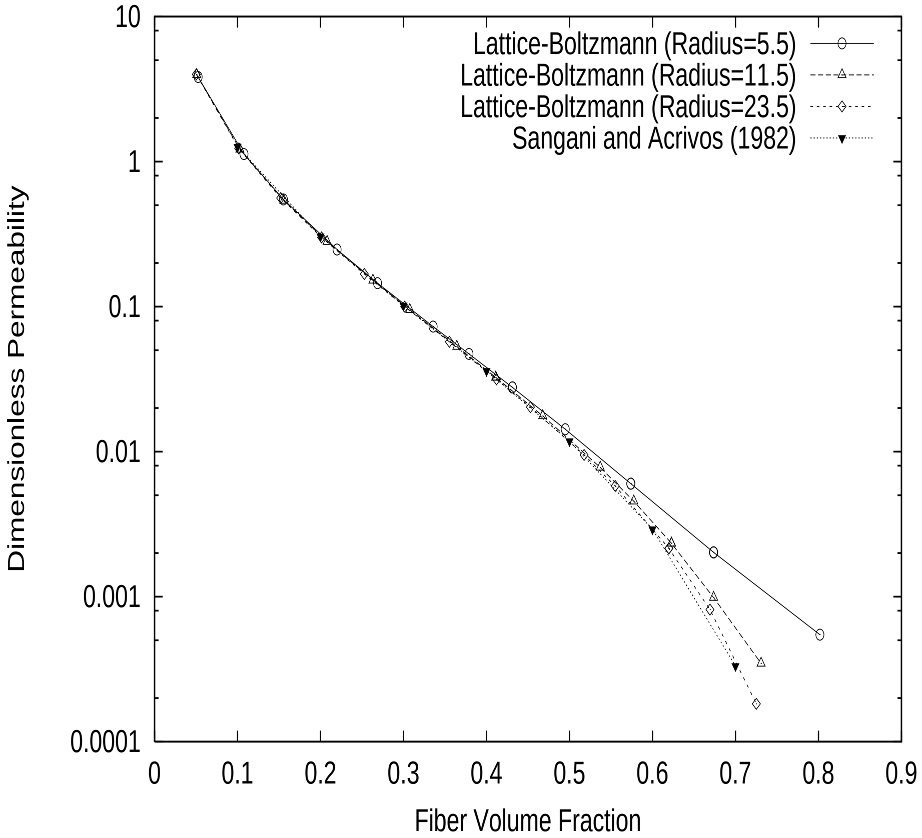

Figure 7.5: The calculated dimensionless permeability k/r^2 as a function of fiber volume fraction for different cylinder radii. The semi-analytical result of Sangani and Acrivos [105] is also included.

Acrivos[105]. The cylinders have been discretized using radii of 5.5 to 23.5 lattice points for the full range of fiber volume fractions. It is clear that there is a very good agreement between our simulations and the semi-analytical curve of Sangani and Acrivos [105] for the complete range of fiber volume fractions, as the cylinder radius is increased.

BCC Lattice Configuration

The results for the BCC lattice configurations are shown in Fig. 7.6.

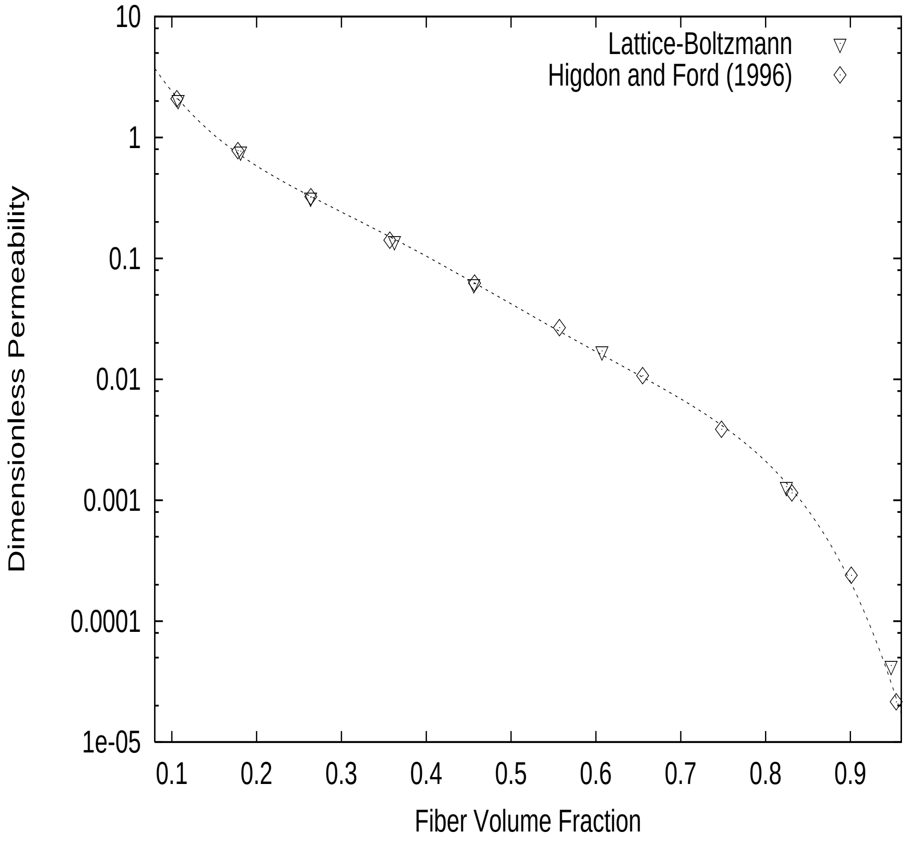

Figure 7.6: The calculated dimensionless permeability k/r^2 as a function of fiber volume fraction for the full range of solid fractions. For $\phi < 0.4$, $R = 6$ lattice points, for $0.4 < \phi < 0.6$ $R = 12$ and $R = 18$ lattice points otherwise. To guide the eye a dashed curve through the numerical results of Higdon and Ford is included [107].

From preliminary studies we found that accurate results are guaranteed when the cylinder radius is varied from 6 to 30 lattice points for increasing fiber volume fractions (data not shown). In Fig. 7.6 we have included the hydraulic permeabilities computed by Higdon and Ford using Spectral Boundary Element Methods. We clearly see that the Lattice-Boltzmann results are in excellent agreement with Higdon and Ford's calculations. A further increase of the cylinder radii does not have a significant effect on the accuracy of the results.

As noted in Ref. [114] the agreement between the LBM results for the ordered fibrous media and that described in Refs [105, 107] is important because it shows that the LBM is accurate over a larger range of fiber volume fractions compared to the results obtained by the approach based on numerical slender body theory. Moreover, its accuracy is comparable to Spectral Boundary Element methods used by Higdon and Ford for the full range of fiber volume fractions.

Disordered media I: Random Fiber Mats

Before performing flow simulations in the random fiber webs we have first conducted a convergence study in order to gain insight in the minimum grid resolutions that guarantee acceptable accuracy for different fiber volume fractions. For this we made a series of test runs using fibers of aspect ratio 10, *i.e.* of size $w_F \times w_F \times 10w_F$, with $w_F = 5$, 10 and 20 grid units. In these tests the size of the simulation lattice was $L_x \times L_y \times L_z = 20w_F \times 20w_F \times 10w_F$. Moreover, the relaxation parameter τ of the LBGK collision operator was varied from 0.668 to 2 corresponding to the dynamic viscosity $\nu = (2\tau - 1)/6$ [21] ranging from 0.056 to 0.5 (in grid units). The main reason for varying the relaxation parameter is to compare the results obtained on different grid resolutions for varying τ. It is expected that as τ approaches to 0.668 ($\nu = 0.056$, the numerical errors due to the bounce-back boundary condition will decrease [49].

In Fig. 7.7 we show the computed permeability as a function of viscosity ν for two test systems of different fiber volume fractions. The nearly linear dependence of ν on permeability [49] is clearly seen in this figure. For $\phi = 0.33$ (Fig. 7.7a), the result is already almost independent of the grid resolution for the smallest value of the viscosity. For low fiber volume fractions (with $\nu = 0.056$), resolution $w_f = 5$ can be used. For a higher fiber volume fraction finite-size effects become more pronounced. Comparing the simulated permeabilities for $\phi = 0.61$ (Fig. 7.7b) at $\nu = 0.056$, we can conclude that $w_F = 10$ is satisfactory for high fiber volume fractions.

In the actual permeability simulations fibers of aspect ratio 20, *i.e.* of size $w_F \times w_F \times 20w_F$, and a lattice of dimensions $80w_F \times 80w_F \times 10w_F$ were used. The flexibility parameter F was varied from 0 to 3 which corresponds to fiber volume fractions ϕ ranging from 0.05 to 0.58. In the simulations $\tau = 0.668$ ($\nu = 0.056$) and two different values for w_F were used. For $\phi < 0.4$, $w_F = 5$ was used, and the size of the simulation lattice was $400 \times 400 \times 60$ grid points. For $\phi > 0.4$, $w_F = 10$ and a lattice of $800 \times 800 \times 110$ grid points were used. For these discretizations, the estimated finite-size errors of the simulated permeabilities were less than 15%. This is estimated from the calculated permeabilities for the different values for the w_F parameter and $\nu = 0.056$ (see Fig. 7.7).

When 32-bit floating point numbers were used, the larger simulation lattice required 5.4 GByte of core memory. The simulations were therefore carried out using 64 nodes (300 MHz CPUs with 128 MByte of memory) on a Cray T3E system. For parallelization of the method we refer to chapter 5. The required CPU time was typically between 1 and 4 hours. Notice that we have used the IMR method described in chapter 3 to reduce the saturation times of the simulations.

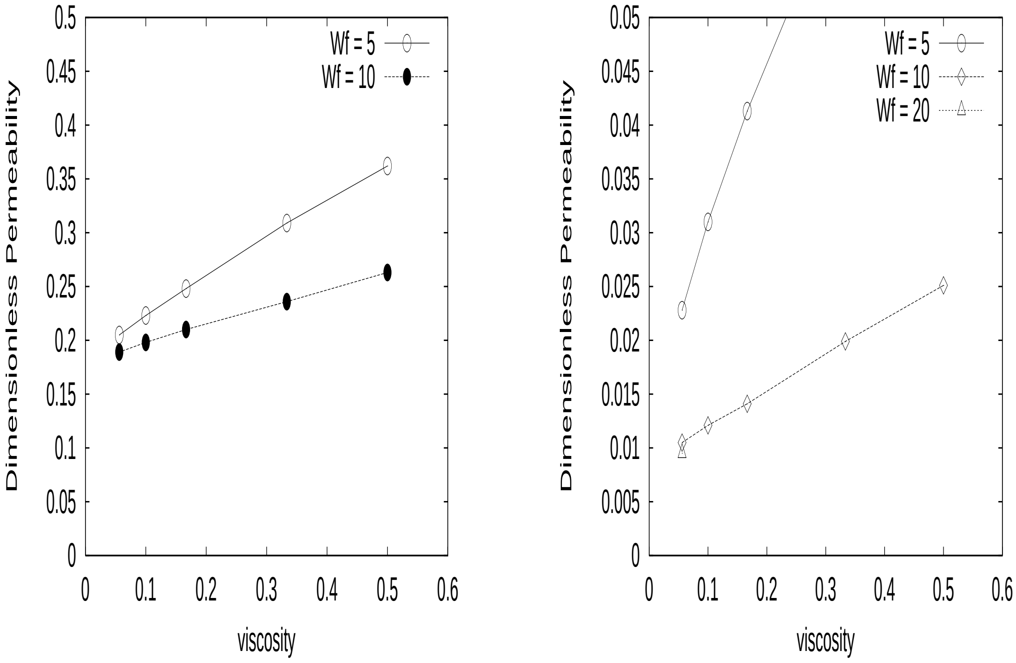

(a) (b)

Figure 7.7: Calculated dimensionless permeability k/r^2 as a function of viscosity ν for two test samples with fiber volume fraction $\phi = 0.33$ (on the left) and $\phi = 0.61$ (on the right). Here $r = w_F/2$ is the hydraulic radius of the fibers. The fiber widths (grid resolutions) are w_F=5, 10 and 20.

In Fig. 7.8 we show a simulated stationary velocity field for a flow in the z direction through the highly inhomogeneous sample shown in Fig. 7.3. It is evident that there are large fluctuations in the velocity field reflecting the variations in the local fiber volume fraction of the sample. These fluctuations, which are inherent in random porous structures, will affect the permeability, except at very low fiber volume fractions, such that it is expected to become higher than that for regular arrays of pores [102]. This effect will be seen in the results given below.

In Fig. 7.9 we show the simulated permeability of the random fiber web as a function of the fiber volume fraction. In this figure solid triangles denote the simulated values. It is evident that there are two distinct features in the simulated permeability curve. Firstly, it seems to diverge as expected when $\phi \to 0$, and, secondly, k seems to be an exponential function of the fiber volume fraction for a rather wide range of: $0.15 < \phi < 0.58$.
A fit through the last five points with lowest fiber volume fractions of the form $k/r^2 = constant \cdot \phi^{-\mu}$ gives $\mu = 1.92$. The simple capillary-tube model by Kozeny and Carman [94] gives $k/r^2 \propto (1-\phi)^3\phi^{-2}$ in this limit so that, as expected, the

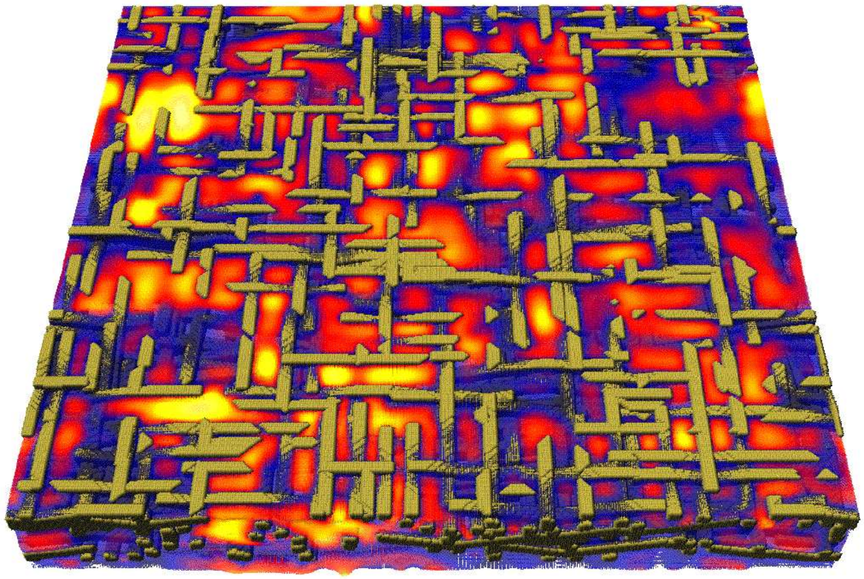

Figure 7.8: The velocity field of fluid flow through the fiber web shown in Fig. 7.3. Bright colors indicate high fluid velocity.

simulated behavior of the permeability is in rather good agreement with this model.

A fit of the form $\ln(k/r^2) = A + B\phi$ to the rest of the simulated points gives $A = -9.5$, $B = -10.4$, with a very high correlation between the simulated points and the fitted curve. So far there have been no analytical results which would have produced this kind of exponential behavior at intermediate fiber volume fractions. It will not hold near the percolation threshold at which permeability vanishes. This critical region is however beyond the present computational capabilities.

Experimental results [115, 102], shown in Fig. 7.9 as open circles and squares, conform well with the simulated points. Notice that there is no free parameter in the present model as permeability is scaled by the square of the hydraulic radius of the fibers, and the relaxation parameter τ is only used to fix the necessary grid resolution. The level of agreement is therefore astonishingly high. It also shows that the model web used here captures the essential features of the fibrous filters and compressed fiber mats used in the experiments.

Also shown in Fig. 7.9 are three curves which are results of previous analytical [102] (curve (1)), numerical [107] (curve (2)) and semi-empirical [94, 115, 116] (curve (3)) considerations. Curve (1) is given by $k/r^2 = \frac{3}{20\phi}(-\ln(\phi) - 0.931 + O(1/\ln(\phi)))$, an expression obtained in Ref. [102] for a cubic lattice model (see section 2), and curve (2) results from a numerical solution [107] for the Stokes flow in a face-centered-cubic (fcc) array of fibers. Both these curves are below the simulated points, especially for decreasing fiber volume fraction. Notice

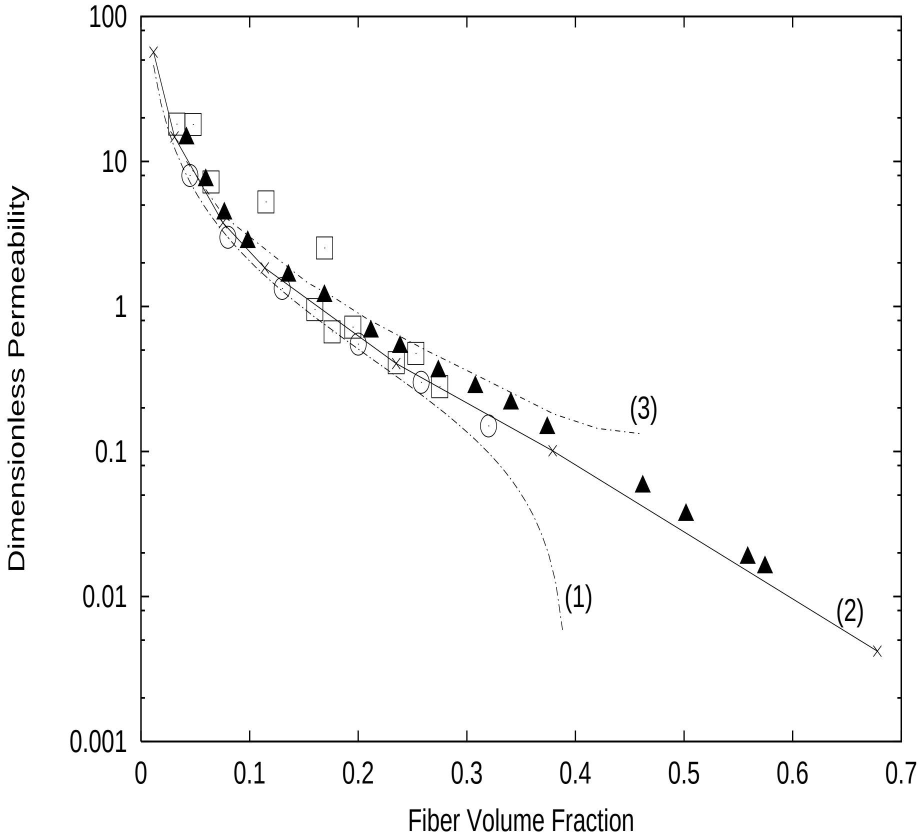

Figure 7.9: The calculated dimensionless permeability k/r^2 as a function of fiber volume fraction, ϕ (black triangles). Open squares and circles show the experimental results for fibrous filters [102] and compressed fiber mats [115, 102], respectively. Curve (1) is the analytical result for cubic lattice given in Ref. [102], curve (2) is the numerical result (crosses) for a FCC lattice from Ref. [107], and curve (3) shows the result of a fit with the Kozeny-Carman relation, Eq. (7.6).

that the fcc result also follows an exponential law at intermediate fiber volume fractions. It is 30-40% below the random fiber-web result for these volume fractions, but approaches the latter for high fiber volume fractions since the percolation threshold of the fcc lattice [107] is at a much higher fiber volume fraction. Curve (3) is the Kozeny-Carman expression [94]

$$k = (1-\phi)^3/cS^2, \tag{7.6}$$

where S is the specific surface area of the web, and c is a constant in capillary-tube models but is known to depend on fiber volume fraction in fibrous materials [116]. An empirical fit to measured fiber volume fractions of these materials gives $c = 3.5(1-\phi)^3[1+57\phi^3]/\phi^{\frac{1}{2}}$ [115, 116]. We have used this expression to get the curve (3) from Eq. 7.6. The specific surface area S was determined from the surface area of the (straight) fibers used to construct the web by subtracting the area of the inter-fiber contacts. Because of bending of the fibers this expression

gives a lower bound for S, and curve (3) is expected to overestimate the permeability. This is indeed what happens (*cf.* Fig. 7.9).
Encouraged by the exponential behavior at intermediate fiber volume fractions of the simulated permeability curve, we have made an interpolation formula that connects this behavior with the right asymptotics in the limit $\phi \to 0$. We find that the expression $k/r^2 = A[e^{B\phi} - 1]^{-1}$ with $A = 5.6$, $B = 10.1$, fits all the simulated points very well. So far we have no theoretical arguments to support this very simple form for the permeability.

Disordered Media II: Randomly placed overlapping cylinders

In the previous section we found that the permeability of the random fiber mat has a very simple exponential dependence on the fiber volume fraction for a wide range of ϕ. Moreover, the permeability of the disordered media is 30 to 40% higher compared to that of ordered media. This is due to the fluctuations in the pore sizes along the medium. In this section, we study the permeability of a second disordered medium in which the fibers are oriented randomly and are allowed to overlap freely. Our main objective is to see whether similar observations are still valid for such a medium. The random fiber network that is studied here is shown in Fig. 7.4.
From preliminary simulations of flow through these media it became clear that accurate results can only be obtained when cylinder radii of 6 lattice points are used for fiber volume fractions smaller than 0.5. On the other hand for $0.5 < \phi < 0.7$ cylinder radii of 12 lattice points are required to obtain satisfactory results (data not shown). Beside these accuracy restrictions, the dimension of a typical simulation cell is also determined by the fact that the fibrous medium itself is not periodic in this case (see Fig. 7.4), whereas in the flow simulations simple periodic boundaries are regularly used. This problem can be overcome by using more complicated velocity boundaries instead of periodic flow boundaries. However, if it can be shown that the edge effects due the periodic boundaries are small, the simple approach based on periodic boundaries can still be applied. To gain insight in this matter, we performed preliminary simulations for different simulation sample sizes. The sample dimension is expressed in units of the Brinkman screening length, α^{-1}, which is defined as $\alpha^{-1} = \sqrt{k}$. The Brinkman screening length is the typical length scale in the system in which velocity disturbances caused by the single fibers decay to the bulk flow[110]. In the remainder of this chapter we will make extensive use of this parameter for several purposes. We computed the Brinkman screening length by using Jackson and James's analytical expression for the hydraulic permeability of the cubic lattice model (see section 2). It is expected that as the simulation cell dimension is increased the edge effects become small. Moreover, it is expected that the edge effects are stronger in the dilute limit as then the permeability is relatively high. Simulations for varying cell dimensions indicate that in the dilute limit, the wall effects due to periodicity are small when the simulation cell dimension is in the order of at least $7\alpha^{-1}$. Consequently, lattices of dimensions in the order of 200x200x200 are used in the final simulations.

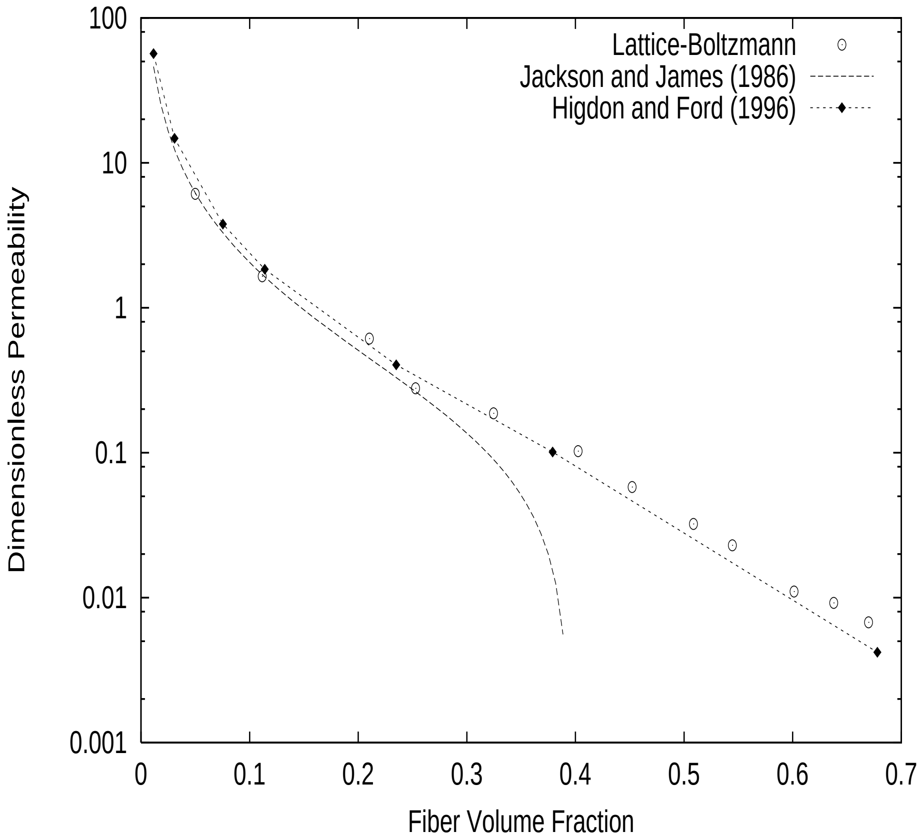

Figure 7.10: The calculated dimensionless permeability k/r^2 as a function of fiber volume fraction. We have included the numerical results of Higdon and Ford for the FCC lattice and the analytical curve of Jackson and James.

In Fig. 7.10 we show the simulated permeability curve. In this figure we included the results of the ordered FCC lattice of Higdon and Ford and the analytical curve of Jackson and James [102]. We clearly see that in the dilute limit there is a very good agreement between our results and that of Jackson and James [102]. The permeability results obtained for these disordered media are also in this case higher than that of the ordered FCC lattice, which is consistent with the behavior found for the permeability of the random fiber mats. Furthermore, the computed permeability curve also shows for this medium a simple exponential dependence for a wide range of fiber volume fractions. In this case, we do not present a detailed comparison with other experimental and numerical results.

In fact the similarity between the permeability of media I and II is obvious from the behavior of both results compared to that of the FCC lattice. It is thus clear that the remarks that have been made concerning the Kozeny Carman relation, the experimental data and the analytical curve of Jackson and James are still valid for media II. In Figure 7.11 we show the permeability results obtained for the random fiber mat and the disordered media II in one graph. We clearly see

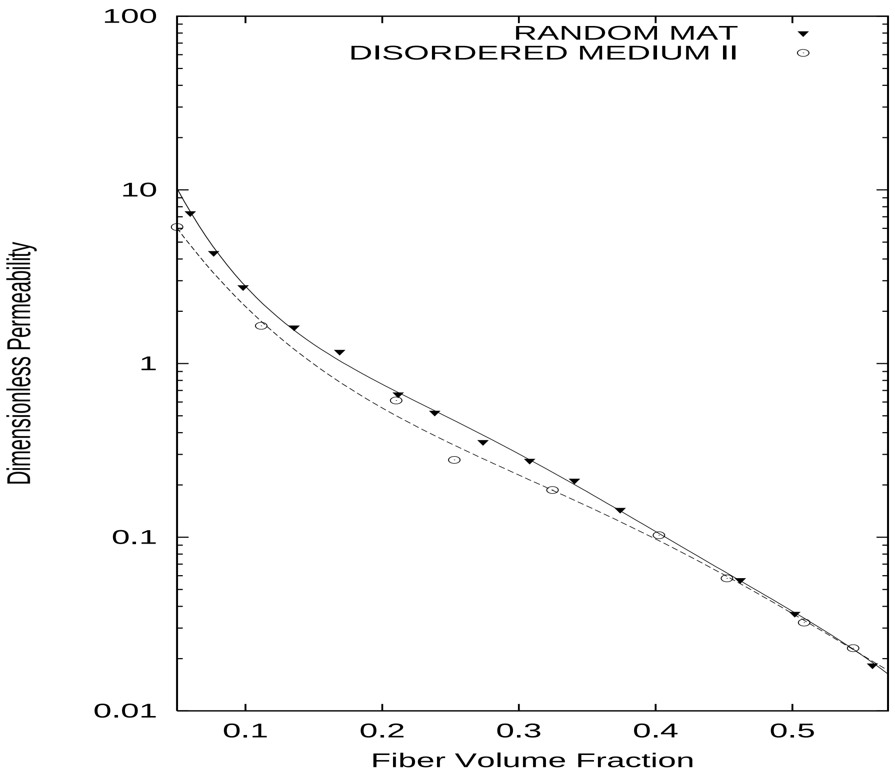

Figure 7.11: The calculated dimensionless permeability k/r^2 as a function of fiber volume fraction. We have included the results obtained for the random fiber mat and the disordered media II.

that for small fiber volume fractions the hydraulic permeability of the random fiber mat is relatively higher. This may be caused by the higher flow resistance in the disordered media II case, due to the relatively high degree of freedom in the fiber orientation. If the fiber orientation is allowed to be random in 3D, the effective surface area perpendicular to the flow direction and thus the flow resistance will be higher. For high fiber volume fractions the fiber orientation in the random mat media is quite irregular due to the fiber bending. Therefore the permeability results are quite close to each in that case.

7.3 The connection between the hydraulic permeability and the geometry of the media

In the previous section we have studied the hydraulic permeability of various fibrous media. The main objective was to obtain the behavior of the permeability as a function of the fiber volume fraction. The fiber volume fraction, ϕ, is in principle used to characterize the geometry of the media. One of the main results is that the hydraulic permeability of disordered fibrous media has an exponential dependence on the fiber volume fraction for a large range of ϕ. In this chapter we explore this relation in more detail. We first argue, using scaling

relations, that an important control parameter for the permeability is the distance between the fibers. Then we find expressions for the fiber-fiber distance for several ordered and disordered media that have been considered in the previous chapter. Next, we correlate the previously found $k(\phi)$ functionality with the behavior of the fiber-fiber distance as a function of the fiber volume fraction. This study provides some insights in the dependence of k on ϕ.
In the next subsection, we first argue that the important parameter that controls the permeability is the fiber-fiber distance. Next, we derive expressions for the fiber-fiber distance for the different media as a function of the fiber volume fraction, $\delta(\phi)$. Finally, we study the connection between the $k(\phi)$ and the $\delta(\phi)$ behavior for various fibrous media.

7.3.1 The role of the fiber-fiber distance

We argue that an important parameter that controls the permeability of fibrous media is the fiber-fiber distance. We do this by making a direct connection between the permeability curve, the flow field, and the fiber-fiber distance. For simplicity we restrict to the case of a periodic array of cylinders. First, let us recall the hydraulic permeability curve of the periodic array of cylinders (see Fig. 7.5). In this curve we clearly see that the permeability decreases as the solid fraction is increased. However, for $\phi \approx 0.5$, there is a relatively strong decrease or a rapid down-turn in the $k(\phi)$ functionality.

To correlate this behavior with the flow field around the cylinder, we analyze the velocity along the diagonal of the simulation cell. A more detailed description of the simulation cell is shown in Fig. 7.12. In fact we are mainly interested in the effect of the cylinder surface on the flow field as a function of the solid fraction and we would like to measure the disturbances caused by the cylinder surface on the flow field. From hydrodynamics it is known that in two-dimensions there is always some interaction between the cylinder and its periodic image [4]. However, the strength of the interaction depends on the distance between the cylinder and its periodic image. As this distance becomes smaller (i.e. the fiber volume fraction increases) the interaction will be more pronounced. Some insight in this matter can be gained by inspecting the velocity along the diagonal of the simulation cell. An interesting quantity here is the x_2-component of velocity, v_2. As expected, v_2 is very small close to the cylinder and increases as the distance to the cylinder surface is increased. At some location it reaches its maximum. If v_2 reaches its maximum at a greater distance, *cf* the typical length scale along which velocity disturbances decay is larger, then there is a relatively stronger interaction between the cylinder and its periodic image.

In Fig. 7.13 we show v_2 as a function of the distance to the cylinder surface in the case of the critical fiber volume fraction, $\phi = 0.5$. It is clear that for this case the

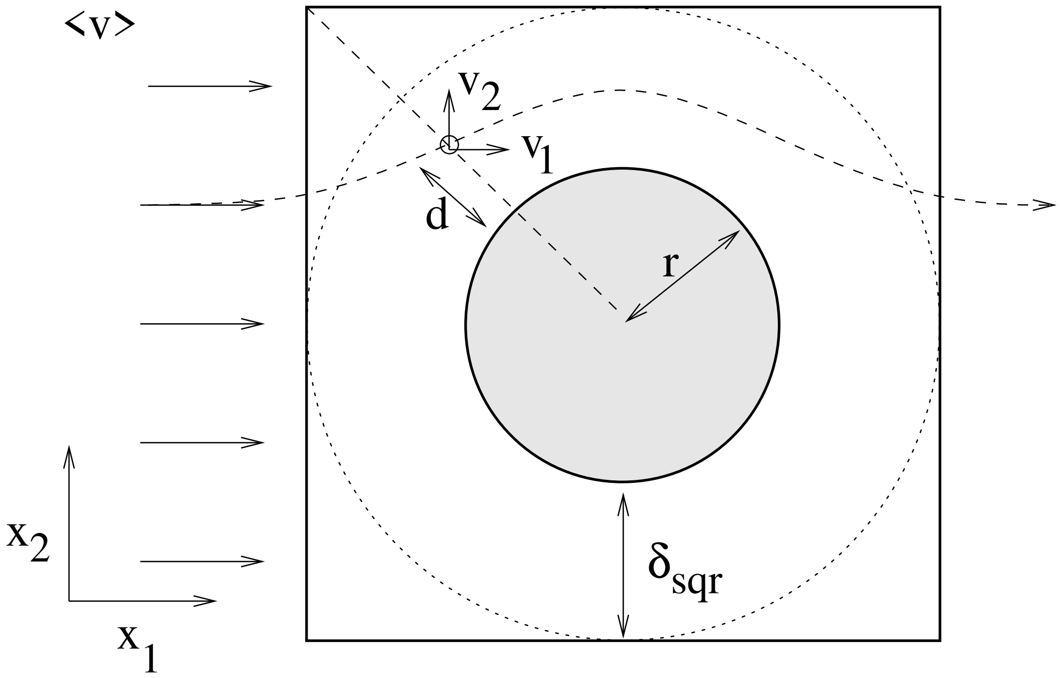

Figure 7.12: A 2D periodic array of cylinders. r is the cylinder radius, δ_{sqr} is half cylinder-cylinder distance, $< v >$ is the mean velocity imposed at the inlet, d is the distance from the cylinder surface along the diagonal of the cell. x_1 and x_2 denote the coordinate system and v_1 and v_2 are the components of the velocity along the x_1 and x_2 axes, respectively.

length scale at which v_2 reaches its maximum, $d_{v_2=max}$, is approximately equal to δ_{sqr}, the half distance between the cylinders. To further explore this behavior, we have determined $d_{v_2=max}$ for varying fiber volume fractions.

In Fig. 7.14 we show the ratio $\frac{d_{v_2=max}}{\delta_{sqr}}$ as a function of ϕ. It is clear that for $\phi < 0.5$, $d_{v_2=max}$ is smaller than δ_{sqr}. For higher fiber volume fractions, $d_{v_2=max} > \delta_{sqr}$. At the critical fiber volume fraction, $d_{v_2=max} \approx \delta_{sqr}$. If we now take δ_{sqr} as the typical length scale over which rapid fluctuations in the velocity field occurs, it is clear that close to the critical volume fraction there is a strong interaction between the cylinder and its periodic image. This is indeed the point where the rapid down-turn in the permeability curve starts.
These observations suggest that there is a strong correlation between the fiber-fiber distance (a geometric property) and the macroscopic permeability curve (a hydrodynamic property). Moreover, simple dimensionality analysis suggests that the hydraulic permeability is expressed in units of the square of some typical length scale [94] and by taking the fiber-fiber distance as the typical length scale in the system, the following relation for the permeability can be derived,

$$k \sim \delta_{sqr}^2. \tag{7.7}$$

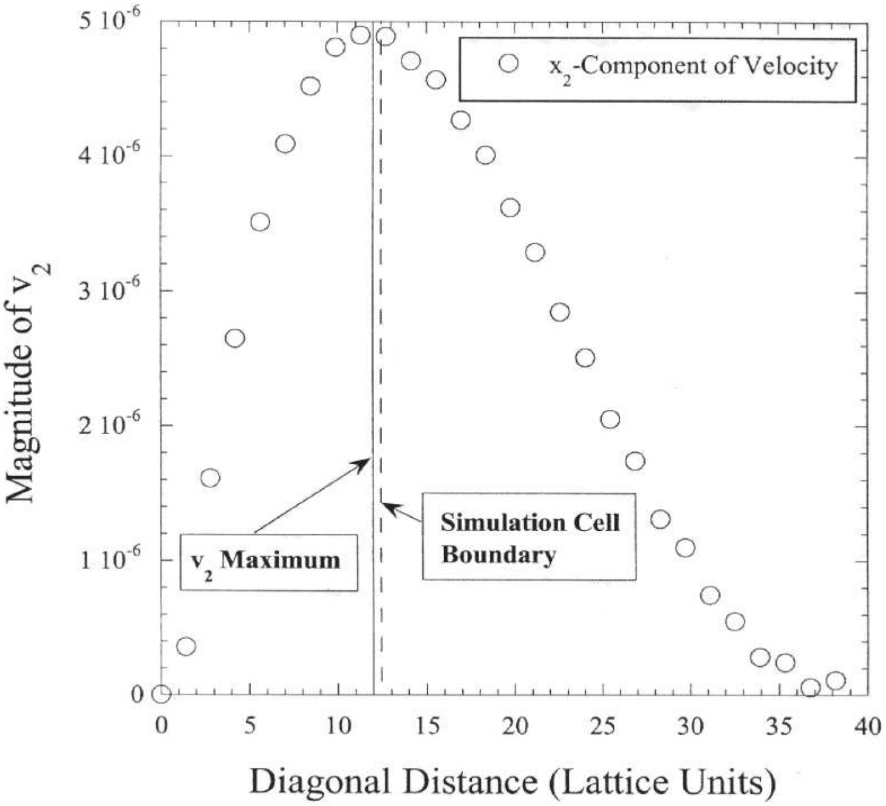

Figure 7.13: The magnitude of the x_2 component of velocity as a function of the diagonal distance from the cylinder surface is shown. The fiber volume fraction is 0.5. The distance to where v_2 goes through a maximum is identified by the vertical solid line, and the distance to the simulation cell boundary, δ_{sqr}, is denoted by the vertical dashed line.

This scaling relation can also be derived if we consider the gap between the cylinder as a tube with radius δ_{sqr}. Within this approximation the mean velocity along the flow direction, $< v_1 >$ is equal to [5],

$$< v_1 >\sim \frac{\delta_{sqr}^2}{\nu}\frac{\partial p}{\partial x_1}.$$

By simply comparing with Darcy's law [94], which can be written as $< v_1 >= -\frac{k}{\nu}\frac{\partial p}{\partial x_1}$, we can derive equation 7.7.

In fact this scaling relation can be intuitively understood as there should be a strong connection between the permeability and the available flux in the medium which in turn is determined by the gap between the cylinders. This connection has also been noted by Tsay and Weinbaum [117]. However, notice that this scaling relation is still very simple, because we do not include more

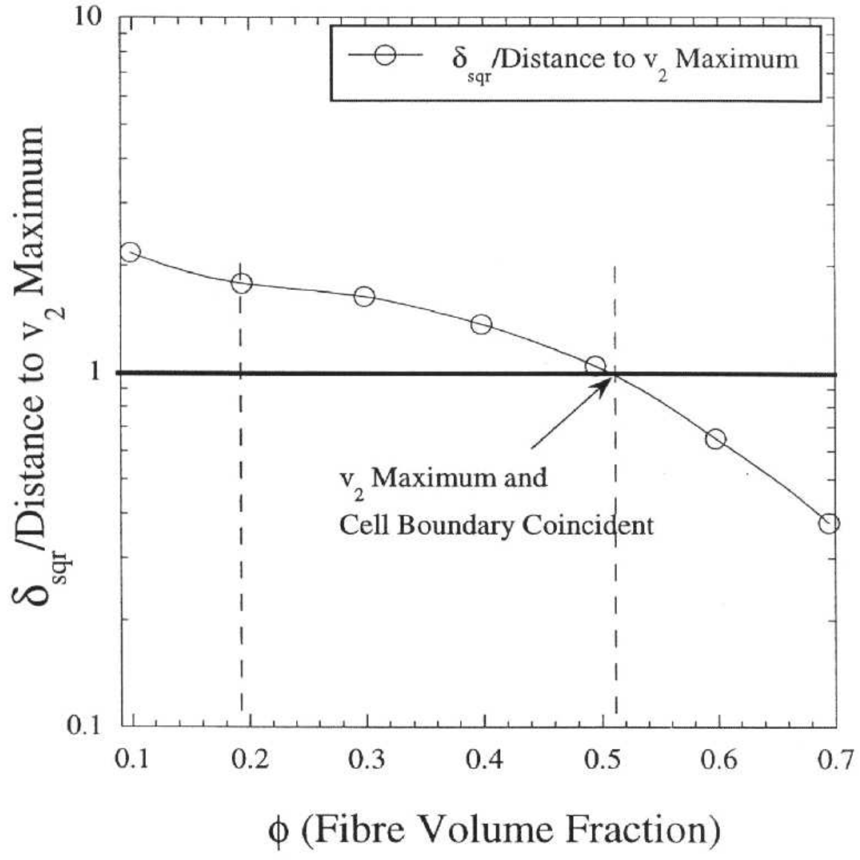

Figure 7.14: The ratio of the distance to simulation cell boundary, δ_{sqr}, and the distance to where v_2 goes through a maximum, $d_{v_2=max}$ is shown as a function of the fiber volume fraction.

complicated geometrical properties of the media like the connectivity and the tortuosity [94]. Therefore we do not expect that this relation will predict the correct values for the hydraulic permeability. But we do still hope to see that the *tendencies* in the permeability curve are correlated with the distance between the fibers.

7.3.2 The fiber-fiber distance

Here we derive expressions for the fiber-fiber distance as a function of the fiber volume fraction. We consider the periodic array of cylinders, the BCC lattice configuration and the disordered fibrous medium used in section 8.4.4. For the periodic array of cylinders we can express the cell size n as a function of the fiber volume fraction using the definition of the fiber volume fraction, $\phi = \frac{\pi r^2}{n^2}$,

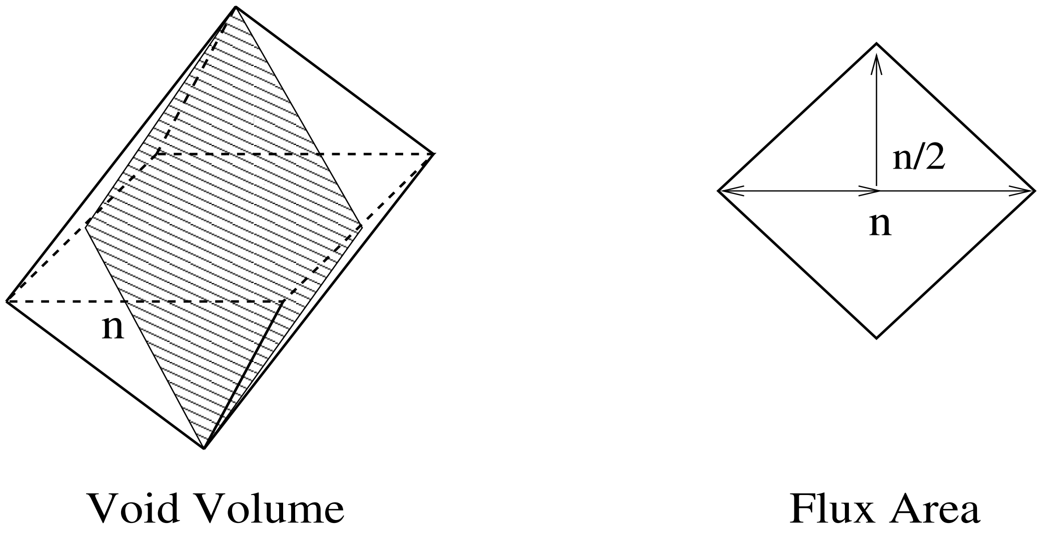

Figure 7.15: The flux area of the BCC lattice configuration. On the left, the upper part of the BCC cell and its periodic image is shown and on the right the flux area is depicted. The flux area is of rhombic shape with side $\frac{\sqrt{2}}{4}n$.

as follows

$$n = r\sqrt{\frac{\pi}{\phi}} \quad and \quad \delta_{sqr} = \frac{n}{2} - r.$$

Using these relations we derive the following result for the fiber-fiber distance, for δ_{sqr},

$$\delta_{sqr} = r(\frac{1}{2}\sqrt{\frac{\pi}{\phi}} - 1). \tag{7.8}$$

To determine the fiber-fiber distance in the case of the BCC lattice configuration we consider Fig. 7.15.

In this figure we show the upper part of the BCC cell together with its periodic image. The fiber-fiber distance is now estimated using the square root of the flux area which in fact is of rhombic shape (see Fig. 7.15),

$$\delta_{bcc} \approx \frac{\sqrt{2}}{4}n - r. \tag{7.9}$$

Notice that we have included a correction factor (the second term in the r.h.s. of Eq. 7.9) in this result to take into account for the finite thickness of the fibers. For the disordered fibrous media, the estimation of the fiber-fiber distance is more complicated. Since the distances have a large spatial variation, we consider a statistical description and we use Ogston's probability distribution for the radii of spheres that fit in the gap between the cylinders [118]. It is given by,

$$\frac{dP}{dD} = \frac{2\phi}{r^2}D\exp(-\phi\frac{D^2}{r^2}). \tag{7.10}$$

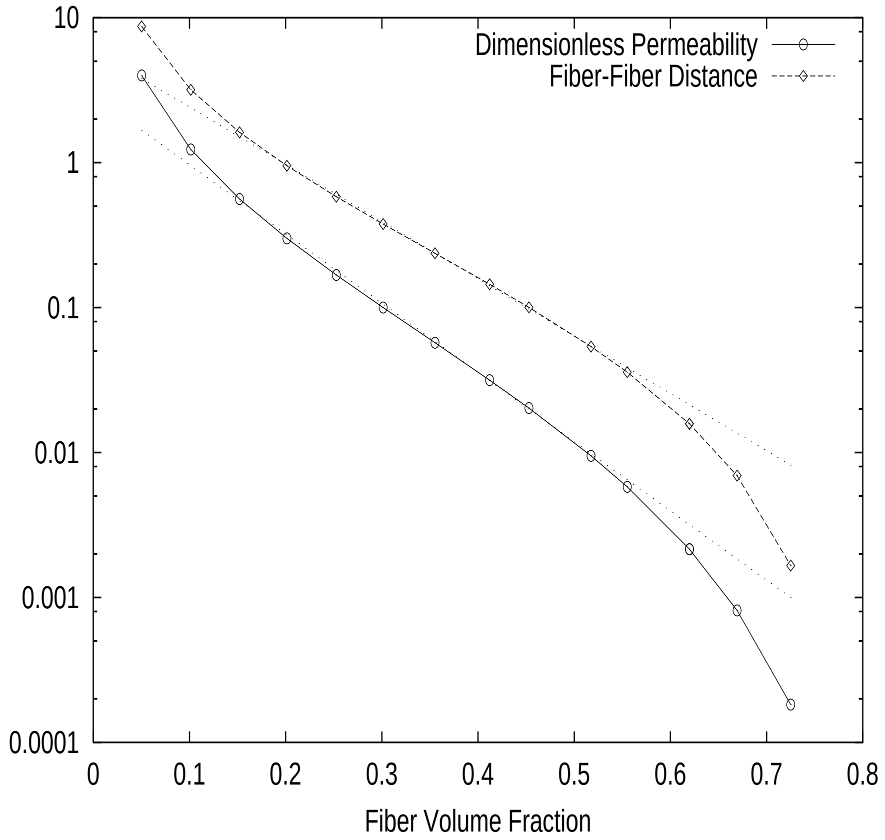

Figure 7.16: Results for a periodic array of cylinders. The hydraulic permeability and the fiber-fiber distance as a function of the fiber volume fractions. The important transitions in the permeability curve is similar to that of the fiber-fiber distance curve. Dashed lines are included to illustrate the functional behavior and its transitions.

In this equation, $\frac{dP}{dD}$ is the probability density distribution of distances, D, between the cylinders. As an estimation for the fiber-fiber distance we use the mean distance,

$$< \delta_{ran} >= \frac{r}{\phi^{\frac{1}{2}}} \frac{\sqrt{\pi}}{2} - r. \tag{7.11}$$

The standard deviation,

$$std = \frac{r}{\phi^{\frac{1}{2}}}(1 - \frac{\sqrt{\pi}}{2}), \tag{7.12}$$

is used to characterize the spatial variation in the gap sizes [114]. Notice that this distribution has been modified to take into account the effect of the finite radii of the cylinders.

7.3.3 Results

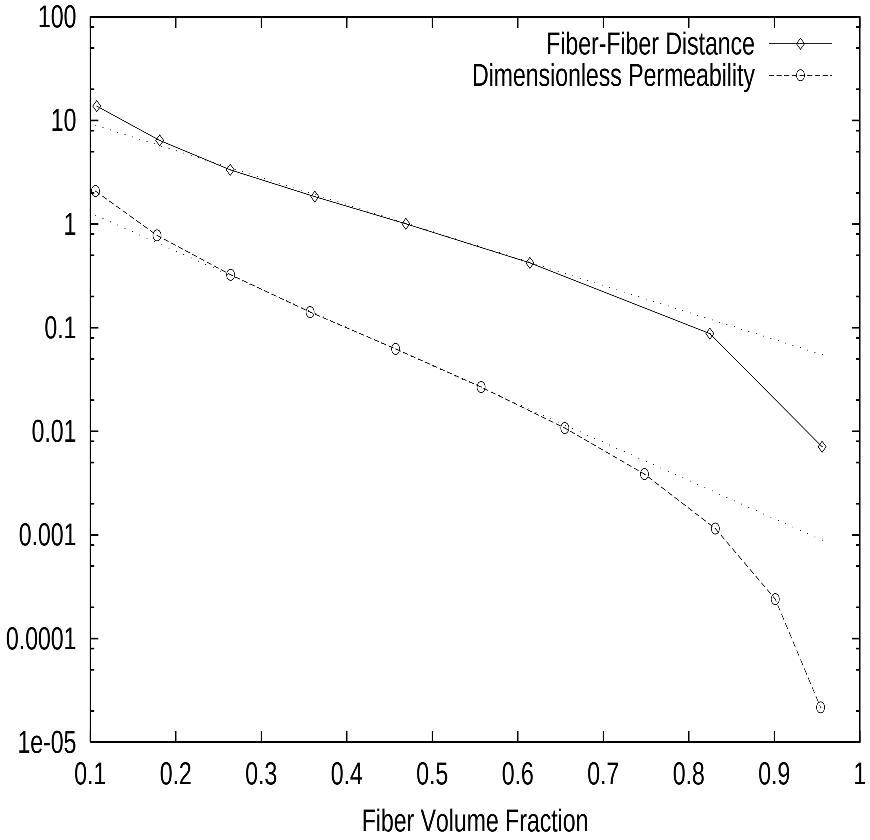

Figure 7.17: Results for the BCC lattice. The hydraulic permeability and the fiber-fiber distance as a function of the fiber volume fractions. The important transitions in the permeability curve is similar to that of the fiber-fiber distance curve. Dashed lines are included to illustrate the functional behavior and its transitions.

In Fig. 7.16 we show the $k(\phi)$ and the $\delta_{sqr}(\phi)$ in the case of the periodic array of cylinders. It is evident that there is indeed a strong similarity between $k(\phi)$ and $\delta_{sqr}(\phi)$ over the entire range of fiber volume fractions. The important transitions in the permeability curve are similar to the transitions in the fiber-fiber distance curve. Although there is no clear linear relationship between $k(\phi)$ and $\delta^2_{sqr}(\phi)$, the scaling estimate can still be used to predict the transitions that occur in the permeability curve.

The results for the BCC lattice configuration are shown in Fig. 7.17. We observe that the scaling estimate captures the trend of the permeability curve. Even in this case, the scaling estimate can still be used to predict the transitions that occur in the permeability curve.

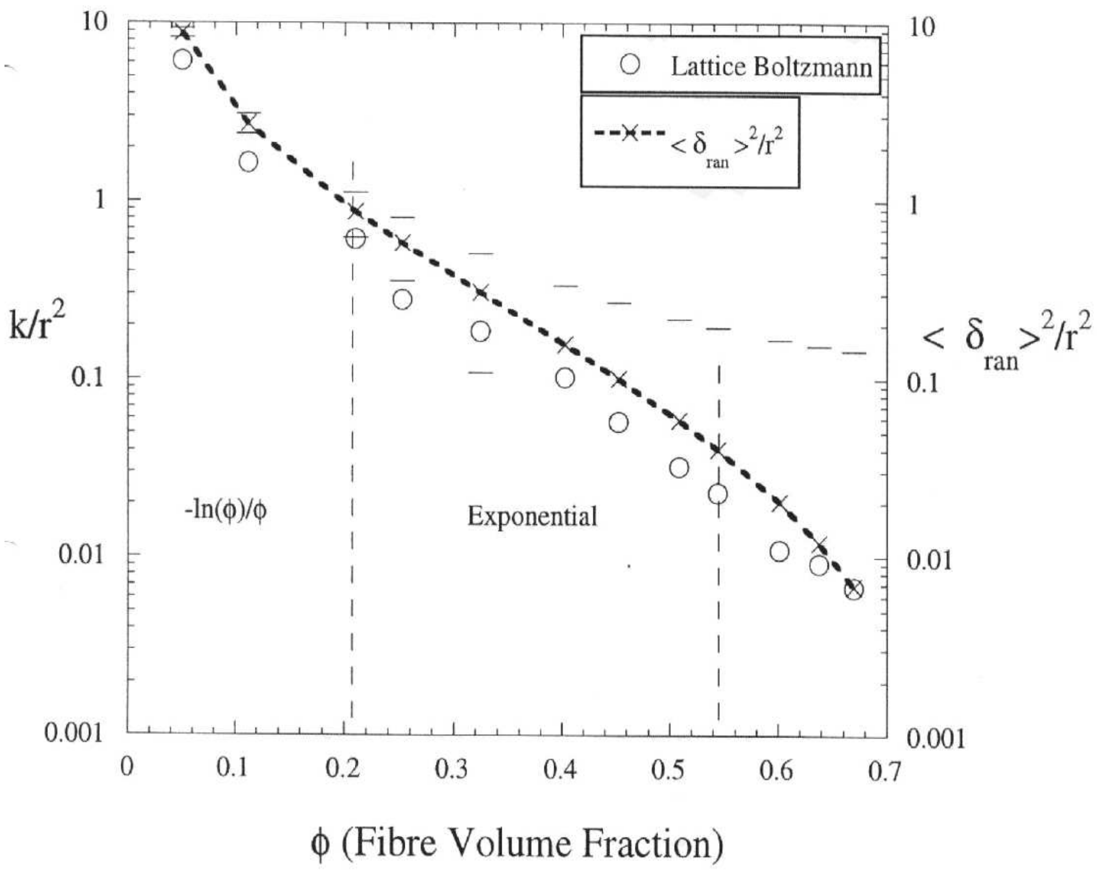

Figure 7.18: Results for disordered media II. The hydraulic permeability and the fiber-fiber distance as a function of the fiber volume fractions. The important transitions in the permeability curve is similar to that of the fiber-fiber distance curve. Dashed lines are included to illustrate the functional behavior and its transitions.

The results for the disordered medium are shown in Fig. 7.18. We observe that even in this case, the scaling estimate captures the trend of the permeability curve. Moreover, the estimated permeabilities are of the proper order of magnitude. The interesting observation is that the simple exponential dependence of the hydraulic permeability is very similar to the $\delta_{ran}(\phi)$ functionality.
Our results suggest that the $k(\phi)$ behavior is strongly correlated with that of $\delta(\phi)$. The characteristics of the hydraulic permeability curve can therefore be at least partly explained by that of the fiber-fiber distance as a function of ϕ.

7.4 The permeability of bounded fibrous media

In the previous sections we studied the hydraulic permeability of various fibrous media. We considered the functional behavior of the permeability and the fiber volume fraction for a large range of fiber volume fractions and a wide variety of fibrous media. We compared our results with existing analytical, nu-

merical and experimental data. Besides this it is shown that there is a distinct connection between the hydraulic permeability and the distance between the fibers. This connection is explored and used to explain the behavior of the permeability curve as a function of the fiber volume fraction.
Although these studies already provide much relevant insight in the physics of fluid flow through fibrous media, we will additionally consider in this section another important aspect related to this topic. It is obvious that all the media studied in the previous section are unbounded. We studied configurations with periodic geometries. However, many fibrous media in practice are bounded. Typical examples are ultra-filtration, gel permeation chromatography and filtration of blood. It is therefore very important to investigate the effect of the wall boundaries on the permeability. In this section, we focus our attention on fibrous media placed between two parallel plates and calculate the $k(\phi)$ behavior as a function of the distance between the parallel plates for ordered and disordered 3D fibrous media. Our aim is to explore the effect of the wall boundaries on the hydraulic permeability and to compare the results with existing data. We therefore first study in section 8.4.1 a bi-periodic array of cylinders and next consider a disordered fibrous media in section 8.4.2.

7.4.1 A bi-periodic array of cylinders

The cell configuration for a bi-periodic array of cylinders is shown in Fig.7.19.

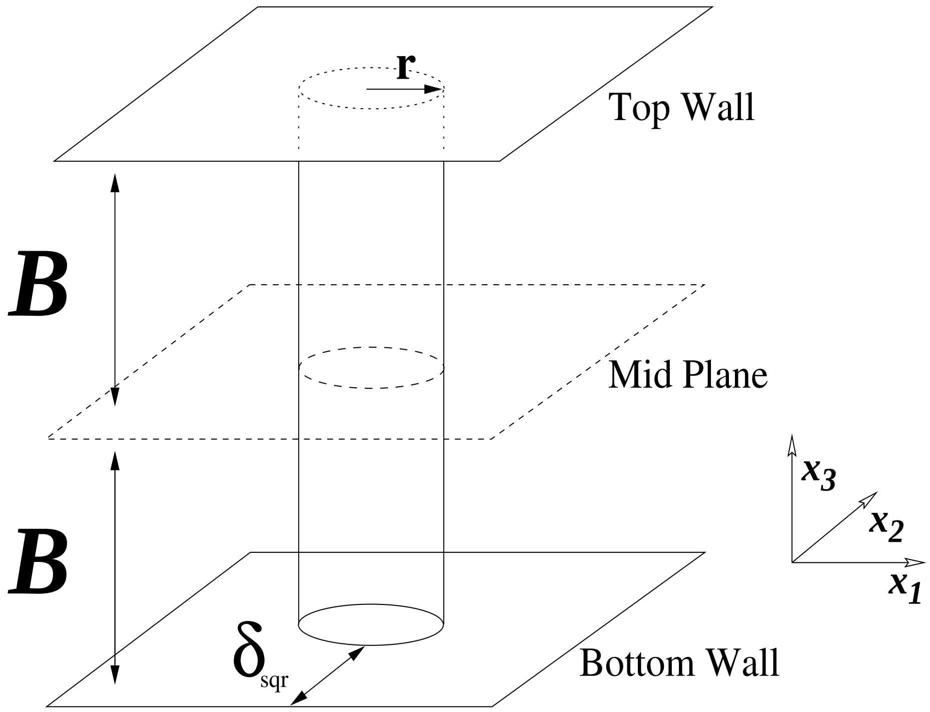

Figure 7.19: A bi-periodic array of cylinders. This cylinder is placed between two parallel plates. r is the radius of the cylinder and δ_{sqr} is the distance between the cylinders and B is the half-distance between the parallel plates.

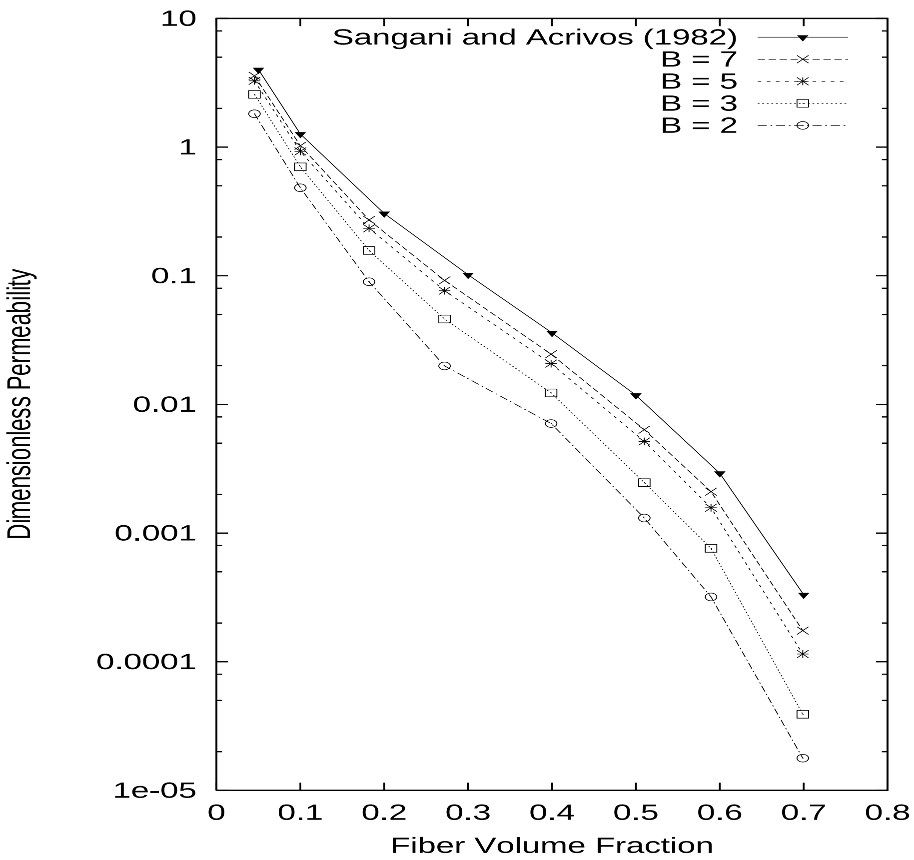

Figure 7.20: Results for a bi-periodic array of cylinders. The hydraulic permeability as a function of the fiber volume fractions for $B = 2, 3, 5$ and 7 Brinkman screening lengths.

In this setup a cylinder is placed between two parallel plates, the top and the bottom wall, respectively and the remaining boundaries of the simulation cell are periodic. The flow is directed from left to right. The important parameter here is the half-distance between the parallel plates, B, which can be expressed in terms of the Brinkman screening length, α^{-1}, defined as $\alpha^{-1} = \sqrt{k}$. As stated in section 8.2, the Brinkman screening length is the typical length scale over which fluctuations decay to the bulk flow. It is therefore the logical choice for the unit length scale in studies aiming to explore the effect of boundaries on the permeability.
We determine the hydraulic permeability as a function of the fiber volume fraction for B varying from 2 to 7 Brinkman screening lengths. The Brinkman screening length is computed using the semi-analytical results of Sangani and Acrivos (see section 8.2 and Ref. [105]).

The results are shown in Fig. 7.20. As expected, we see that the permeability of the bounded cell approaches to that of the unbounded configuration as B is increased. Moreover, the rate at which the permeability decreases for a specific

change in B, is approximately constant for all the fiber volume fractions. The percent differences between the calculated permeability and the unbounded result are 38%, 47%, 66% and 80% on average for 7, 5, 3, and 2 Brinkman screening lengths respectively. This is consistent with the notion that the bounding walls behave like an *effective medium* which causes a uniform reduction in k over a large range of fiber volume fractions.
In the literature only a few studies reported on bounded fibrous media. The most notable one is the effective medium theory of Tsay and Weinbaum [117]. They solved Brinkman's equation [3] and derived the following equation for the permeability of bounded fibrous media,

$$k_{bounded} = k\left(1 - \frac{\tanh \frac{B}{\alpha^{-1}}}{\frac{B}{\alpha^{-1}}}\right), \tag{7.13}$$

where $k_{bounded}$ is the permeability of the bounded medium and k is the permeability of its unbounded instance. This estimate is expected to be only valid in the dilute limit as then the Brinkman approximation is also valid [113].

In Fig. 7.21 we show the permeability as a function of the fiber volume fraction for the case $B = 5\alpha^{-1}$. In this figure we included the analytical result of Tsay and Weinbaum (Eq. 7.13). We observe a good agreement between our results and that of Tsay and Weinbaum for fiber volume fractions smaller than 0.25 (dilute limit). Similar results are found for B is 2, 3 and 7 Brinkman screening lengths (data not shown). This result is important, because it confirms the range of validity of the effective medium theory of Tsay and Weinbaum which is based on several approximations and is not expected to be valid for the entire range of fiber volume fractions as noted above. Based on the connection between the permeability and the fiber-fiber distance that is discussed in the previous section, Clague et al. [114], proposed a new phenomenological estimate for the permeability of bounded media. This estimate is in good agreement with our simulation results and can be used for rapid prediction of the hydraulic permeability of bounded fibrous media (data not shown). For details we refer the interested reader to Ref. [114].

7.4.2 Disordered media

The results for the disordered media are shown in Fig. 7.22. To guarantee accurate results we used cylinder radii of 6 lattice points for $\phi < 0.4$, 12 lattice points for $0.4 < \phi < 0.6$ and 18 lattice points. Moreover, we performed on the order of 5 simulations for each fiber volume fraction, because in this case the bounded medium is heterogeneous due to the disorder of the medium and the relatively small simulation cell dimensions. It is clear that for the disordered medium the effect of the walls is stronger compared to the ordered case. For example, for $B = 5\alpha^{-1}$, at $\phi = 0.2$ there is a 61% difference between the calculated result

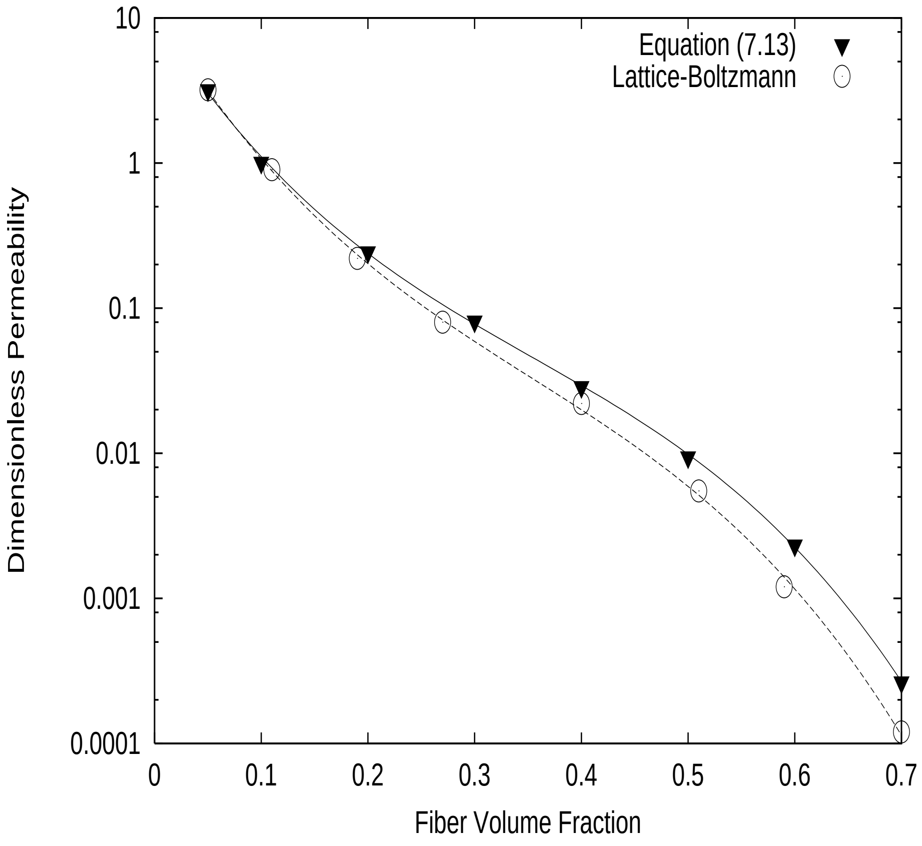

Figure 7.21: Results for a bi-periodic array of cylinders. The hydraulic permeability as a function of the fiber volume fractions for $B = 5$ Brinkman screening lengths. The effective medium theory result of Tsay and Weinbaum [117] is also included in the figure.

and the unbounded results. For $\phi > 0.2$, the percent difference relative to the unbounded result is approximately 75% on average. Also, unlike the ordered media, the slope in the calculated hydraulic permeabilities steepens as B is reduced below 4 Brinkman screening lengths. The transition between the dilute and the intermediate regions, however, appears to occur at similar fiber volume fraction, $\phi \approx 0.2$.

Finally, we compare the hydraulic permeabilities calculated using the Lattice-Boltzmann method with the Brinkman approximation given in Eq. 7.13 (see Fig. 7.23). In this particular system, the wall to mid-plane separation, B, equals $5\alpha^{-1}$. The unbounded hydraulic permeabilities used in Eq. 7.13 are taken from our Lattice-Boltzmann result for the associated unbounded, disordered media presented in section 8.2 (disordered media II). In this case, it is evident that the effective medium theory of Tsay and Weinbaum [117], overpredicts the hydraulic permeabilities calculated using the LB method. Furthermore, for higher fiber volume fractions, the difference between the effective medium

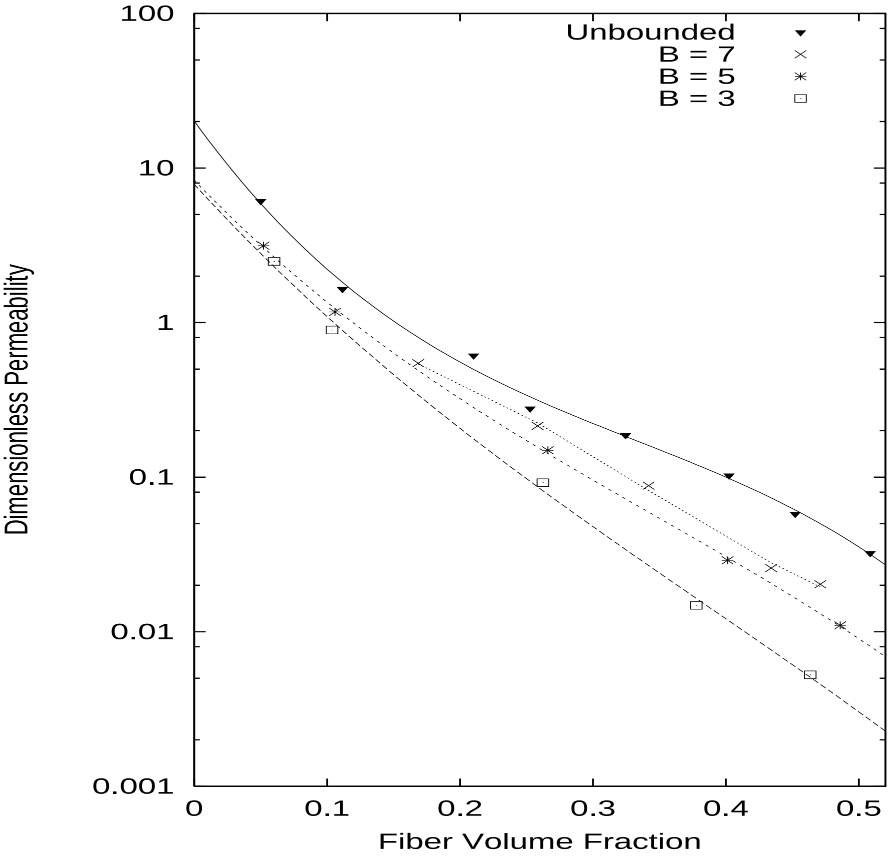

Figure 7.22: Results for the disordered medium II. The hydraulic permeability as a function of the fiber volume fractions for $B = 2, 5$ and 7 Brinkman screening lengths.

theory of Tsay and Weinbaum [117] and hydraulic permeabilities calculated using the LB method is higher compared to the dilute limit. Similar behavior is observed for systems where $B = 2$ and 7 Brinkman screening lengths as well. As we mentioned in the previous section, Clague et al. [114], proposed a new phenomenological estimate for the permeability of bounded media, based on the connection between the permeability and the fiber-fiber distance. This estimate is also in the case of bounded disordered media in good agreement with the simulation results and can be used for rapid prediction of the hydraulic permeability of bounded fibrous media (data not shown). For details we refer the interested reader to Ref. [114].

7.5 Conclusions

We used the lattice-Boltzmann method on a massively parallel computer to solve the permeability of several ordered and disordered models of fibrous media. The simulations have been performed as a function of the fiber volume fraction of the media in a large range. The simulated results were found to be

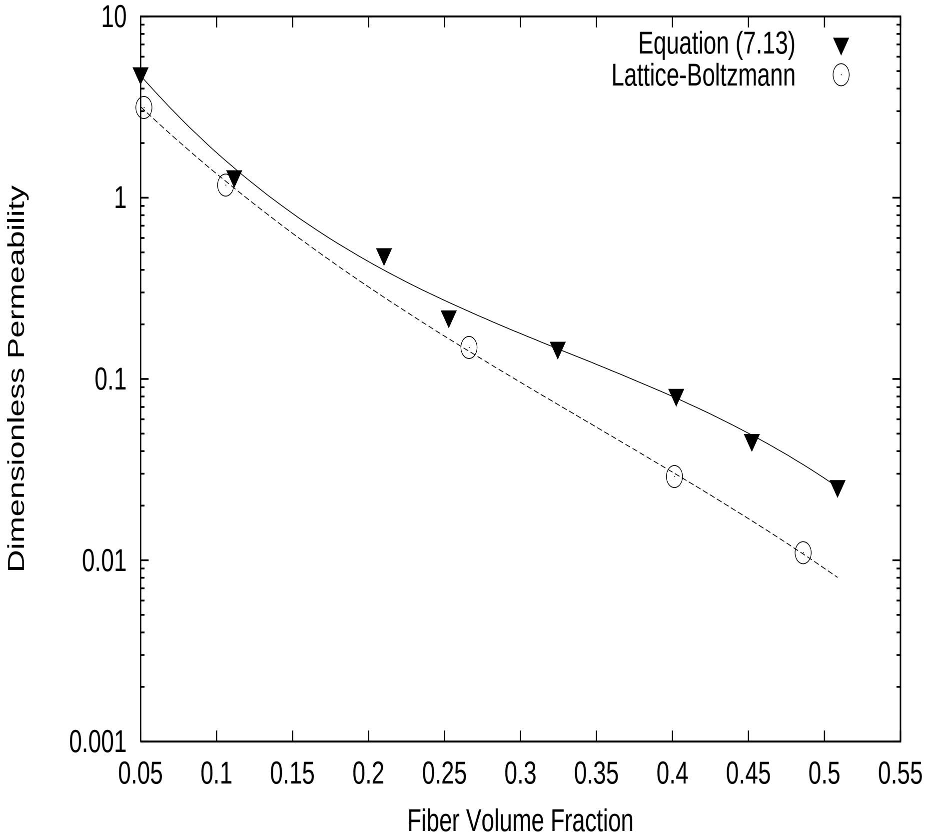

Figure 7.23: Results for disordered medium II. The hydraulic permeability as a function of the fiber volume fractions for $B = 5$ Brinkman screening lengths. The effective medium theory result of Tsay and Weinbaum [117] is also included in the figure.

in excellent agreement with available analytical, numerical and experimental data. Our results suggest an exponential dependence of permeability on fiber volume fraction in a wide range and this functionality seems to be a generic feature of fibrous porous materials, independent of whether they are random or not.

It was argued that there is a correlation between the hydraulic permeability and the distance between the fibers. This correlation was further explored and used as a possible explanation of the behavior of the hydraulic permeability as a function of the fiber volume fraction.

Finally the effect of walls on the hydraulic permeability was investigated. For various wall separation distances the hydraulic permeability is computed for a bi-periodic array of cylinders and a disordered medium as a function of the fiber volume fraction. These results were compared with the effective medium theory of Tsay and Weinbaum [117]. In the dilute limit $\phi < 0.25$ a reasonably good agreement was found for bounded ordered media. For higher fiber volume fraction the effective medium theory of Tsay and Weinbaum [117] over predicts the permeability. Moreover, for the same wall separation distances the effect of the walls is found to be stronger in the case of disordered media and the effective medium theory overpredicts the hydraulic permeability.

Chapter 8

General discussion

In this thesis we studied several aspects of the lattice-Boltzmann method. In fact we demonstrated that the lattice-Boltzmann method is indeed a versatile tool for the numerical simulation of fluid flow in complex geometries. Briefly stated, several new ideas have been proposed useful for efficient and accurate lattice-Boltzmann simulations. These include an analysis of the commonly used boundary conditions and 3D models, parallelization of lattice-Boltzmann simulations, formulation of a new technique to reduce the number of time steps to reach the stationary state and generalization of the lattice-Boltzmann method on nested grids. Moreover, for a nontrivial benchmark case the lattice-Boltzmann method has been compared thoroughly with the state-of-the-art finite-element method. Finally, the transport properties of various models of (dis)ordered (un)bounded fibrous porous media have been studied in detail. We compared the lattice-Boltzmann results with existing theoretical, numerical and experimental data and made a direct connection between the macroscopic fluid flow and the geometry of the media. The main conclusions are stated separately at the end of each chapter and can also be found in the summary of the thesis.
In this chapter we briefly discuss some interesting and hopefully feasible research topics to be studied in the near future. In Fig. 2.2 of chapter 2 we have summarized the recent developments of the lattice-Gas automata and the lattice-Boltzmann method. In fact there are three main directions in the research of this field. The first one is related to computational aspects, e.g. the extension of lattice-Boltzmann models to non-uniform grids. The second one is about novel lattice-Boltzmann simulations and formulation of new models capable of simulating complex hydrodynamics. And finally, studies on fundamental issues like the theory of lattice-Boltzmann models are still in progress. The following suggestions are quite natural steps to proceed with:

- Application of different formulations of LBM on non-uniform grids to realistic three-dimensional problems. In recent years, several studies have been reported for extending the lattice-Boltzmann method to non-uniform lattices. All these efforts including that of our own are thus far only applied to rather simple geometries. The challenge now is to apply these techniques to realistic cases. Important issues like grid or mesh generation and efficient parallelization will be major difficulties.

- Boundary conditions. Much debate is still going on about boundary conditions for LBM. In fact the major problem of the boundary conditions is that the number of unknown particle densities is higher then the number of constraints (the prescribed density or momentum). Several models have been proposed in the past to deal with this problem consistently. As we have shown in chapter 3 more sophisticated methods may be required in some cases.

- Fast lattice-Boltzmann schemes. One major problem of the LBM is the relatively large number of time steps sometimes required to reach the stationary state. In chapter 4 we proposed an alternative method for reaching a faster convergence. However, this technique is limited to body-force driven flows. Methods based on the numerical solution of the Boltzmann transport equation, as recently been studied by Verberg and Ladd [119], are very promising and must be stimulated.

- Moving boundaries. There are many applications related to fluid flow in dynamically changing geometries. Typical example are suspension flow and blood flow in arteries. Extension of lattice-Boltzmann models to these cases may open a very wide range of potential applications.

- Fluid flow in porous media. The most successful application of the lattice-Boltzmann method is fluid flow in porous media. However, most of the studies are dealing with systems far from the percolation threshold. This is mainly due to computational limitations. The study of fluid flow near the percolation threshold is of fundamental physical interest. For two-dimensional systems these problems might still be feasible using current state-of-the-art parallel computing technology.

- Complex hydrodynamics. Different models have been proposed in the past for simulation of complex hydrodynamics, e.g. multi-phase , thermal and viscoelastic models. In this thesis we studied fluid flow in the SMRX static mixer reactor. We restricted to single-phase, isothermal and Newtonian fluid mechanics. However, in real engineering processes these restrictions may not be appreciated. It is interesting to apply the existing lattice-Boltzmann models for complex hydrodynamics to simulate complex flow in for instance the SMRX reactor. As all existing lattice-Boltzmann models have their limitations, the only way to really see whether these efforts will be successful is by doing it.

- Theory of lattice-Boltzmann models. As we have already noticed in chapter 2 it has been argued by several authors that the lattice-Boltzmann equation is a specific discretization of the Boltzmann transport equations. Existing knowledge of kinetic theory may therefore be very useful in extending the lattice-Boltzmann method to models for simulating complex hydrodynamics and for other methodological improvements.

Addendum A

Finite-Difference Lattice-BGK Methods on Nested Grids

A.1 Introduction

In recent years the Lattice-Boltzmann method [12, 28, 80] has attracted much attention in the simulation of complex fluid flow problems. Typical examples are fluid flow in porous media, multi-phase flow and particle suspension flow (see e.g. Refs. [12, 16, 40]). The success of this method can be partly attributed to the particle based approach which is directly inherited from its predecessor, the lattice-Gas model [13].

Although the scheme has proven to be very promising, it has some potential shortcomings compared to traditional state of the art numerical methods, like the Finite-Element method. The uniformity of the lattice is argued to be one of them (see e.g. Ref. [29]). From a computational point of view non-uniform grids can be efficient for computing fluid flows because the grid resolution can be adapted to the spatial complexity of the flow dynamics.

The lattice-Boltzmann method evolved from the early lattice-Gas model where particles hop from one lattice site to one of its neighbors, constrained to mass and momentum conservation. In these models a discrete set of velocities is used that is directly connected with the topology of the computational lattice. Correct macroscopic behavior is only guaranteed when the symmetry properties of the computational lattice are such that the transport coefficients are isotropic. The lattice-Boltzmann model automatically inherited this constraint imposed on the lattice from its predecessor.

In this addendum we introduce an alternative approach, allowing LBM simulations on non-uniform grids. In our approach, the computational grid consists of multiple nested grids with increasing spatial resolution. Basically, the discrete velocity Boltzmann equation (see next section) is solved numerically on each sub-lattice and interpolation between the interfaces is carried out in order to couple the sub-grids consistently. The approach is validated for the Taylor vortex flow problem.

A.2 Background

In this section we present a brief overview of the main developments related to non-uniform grids for the Lattice-Boltzmann method. One of the first attempts to generalize the lattice-Boltzmann scheme to non-uniform grids has been reported by Nanneli and Succi [69]. In their approach a finite volume strategy is studied. The non-uniform grid consists of cells corresponding to several grid points in the original lattice. For each cell, a volume-average particle distribution is defined. By using piece-wise constant or linear interpolation methods the coarse grain distribution is approximated. Using this approach reasonable results were found for laminar flow in a channel.
More recently, a different approach for handling non-uniform grids has been proposed by He and Luo [86]. In their method the grids on which the propagation step is performed is decoupled from that of the collision phase. After each propagation step the particle densities are interpolated to the original mesh or grid and then the collision phase in carried out. It was shown, that the quality of this approach is highly determined by the interpolation scheme used [86].
A few years ago, Cao et al. [29] argued that although the physical symmetry (related to the collision phase) and the lattice symmetry (related to the propagation phase) are equivalent for LGA they may be different for Lattice-Boltzmann Models (LBM). LBM can be viewed as a special finite-difference discretization of the single time relaxation approximation of the Boltzmann equation for discrete velocities,

$$\frac{\partial f_i}{\partial t} + \mathbf{e}_i \cdot \nabla f_i = \Omega_i \qquad (i = 1, 2, ..., N), \tag{A.1}$$

where f_i is the particle velocity distribution, $\mathbf{e}_i$ is the velocity along the i-th direction, N is the number of different velocities, and Ω_i represents the collision operator. By applying a first-order Euler time differencing scheme, a first-order upwind space discretization for the convection term in Eq. A.1, splitting the collision and convection process into two separate steps, and setting the lattice spacing Δx equal to the time step Δt, the standard Lattice-BGK (LBGK) model can be derived [29]. Although both the time and space discretization schemes are first-order the LBGK model is second-order both in time and space, because the numerical viscosity has a special form which can be included in the fluid viscosity.
The important consequence is that in the LBGK model one can now incorporate arbitrary grids in the scheme by exploiting a different time and space discretization then the ones used above (the so-called Finite Difference Lattice-Boltzmann method). Based on this idea Cao et al. [29] proposed the LBGK method on cylindrical coordinates using central difference methods for the space discretization. Later, Mei and Shyy extended these studies to more complicated body fitted coordinates [120]. And recently, Peng et al. formulated a finite volume scheme for the lattice-Boltzmann method on unstructured meshes based on the Boltzmann equation for discrete velocities [121].
In this addendum we discuss a generalization of the method proposed by Cao

et al. [29] to nested grids. The computational grid is basically built up of a number of sub-domains which can have different grid resolutions. On each sub-domain the discrete velocity Boltzmann equation is solved and the adjacent sub-domains are coupled which each other by appropriate interpolation at the boundaries of the sub-domains. We think that such a generalization might be very useful, because the method is still closely related to the spirit of standard LBGK algorithm and thus it is expected that more complex LBM models (multiphase- or thermal models) can still be used in this framework.
We also point out that the formulation of LBM on nested grids has been studied by Fillipova and Hanel [122]. Their approach is based on the LBGK method, whereas we start from the Boltzmann equation for discrete velocities. We will discuss their method in some more detail in section IV.
We first discuss, in section II, the discretization of Eq. A.1. Next, in section III, we introduce the extension of the Lattice Boltzmann scheme on nested grids. We discuss the data structures and a consistent coupling between the different grids. Finally, in section IV, we present some preliminary numerical results.

A.3 Numerical Discretization of the Boltzmann Equation

As argued in the previous section, in our approach the Boltzmann equation for a discrete set of velocities (Eq. A.1) is solved numerically. The numerical discretization consists of a spatial discretization of the convection operator and a time integration of Eq. A.1. The collision operator is defined locally on each lattice point analogous to the standard LBM method. For the spatial discretization we use second-order central-difference and upwind schemes and for the temporal discretization a second-order Runge Kutta method is used.
In this section we review the finite difference schemes. For simplicity we only consider the equation for the velocity pointing to the right neighbor, denoted by index 1. The second-order upwind scheme for link 1 is given by,

$$\frac{\partial f_1}{\partial x} = \frac{(3f_1(x,y) - 4f_1(x-\Delta x,y) + f_1(x-2\Delta x,y))}{2\Delta x}, \tag{A.2}$$

where Δx is the lattice spacing in the x-direction. The central difference scheme is given by,

$$\frac{\partial f_1}{\partial x} = \frac{(f_1(x+\Delta x,y) - f_1(x-\Delta x,y))}{2\Delta x}. \tag{A.3}$$

The molecular velocities, $\mathbf{e}_i$ are in fact free but restricted by stability constraints. In the standard LBGK method they are defined as $\mathbf{e}_i = (cos(\frac{\pi}{2}(i-1)), sin(\frac{\pi}{2}(i-1)))\frac{\Delta x}{\Delta t}$ for $i = 1,2,3,4$ and $\mathbf{e}_i = \sqrt{2}(cos(\frac{\pi}{2}(i-5)+\frac{\pi}{4}), sin(\frac{\pi}{2}(i-5)+\frac{\pi}{4}))\frac{\Delta x}{\Delta t}$ for $i = 5,6,7,8$. Notice that in the standard LBGK method, the velocities $\mathbf{e}_i$ are such that after a single time-step the particles travel to the neighboring lattice point along link i. In our current formulation this is not necessarily the case. In section IV we will discuss this point in some more detail. The convection operation, A_i can be now simply rewritten into the following form,

$$A_i = \mathbf{e}_i \cdot \nabla f_i = e_{ix}\frac{\partial f_i}{\partial x} + e_{iy}\frac{\partial f_i}{\partial y}.$$

By substituting the appropriate finite-difference expressions, we get a fully discrete formulation for A_i.
The time update is performed using a second-order Runge-Kutta scheme. Here we first calculate at each time step, t, the particle densities at time-step $t+\frac{1}{2}$, as follows,

$$f_i(t+\frac{1}{2}) = f_i(t) + \frac{\Delta t}{2}(-A_i(t) + \Omega_i(t)). \tag{A.4}$$

The particle densities at time-step $t+1$ are computed by combining the solutions of time-steps t and $t+\frac{1}{2}$,

$$f_i(t+1) = f_i(t) + \frac{\Delta t}{2}(-A_i(t+\frac{1}{2}) + \Omega_i(t+\frac{1}{2})). \tag{A.5}$$

The collision operator is defined as,

$$\Omega_i(t) = -\frac{1}{\tau}(f_i - f_i^{eq}), \tag{A.6}$$

and in the case of the standard nine-speed LBGK method the equilibrium distribution, f_i^{eq}, is defined as,

$$f_i^{eq} = \rho\, w_i(1 + \frac{3(\mathbf{e}_i\cdot\mathbf{u})}{c^2} + \frac{9(\mathbf{e}_i\cdot\mathbf{u})^2}{2c^4} - \frac{3\mathbf{u}^2}{2c^2}), \tag{A.7}$$

where $c = \frac{\Delta x}{\Delta t}$, w_i is $\frac{4}{9}$ for the rest-particle, $\frac{1}{9}$ for the horizontal and vertical links and $\frac{1}{36}$ for the diagonal links, respectively. The hydrodynamic moments, density ρ, and velocity $\mathbf{u}$ are defined as,

$$\rho = \sum_{i=0}^{N} f_i \qquad\qquad \mathbf{u} = \frac{\sum_{i=1}^{N} f_i\mathbf{e}_i}{\rho}.$$

For the nine-speed LBGK method the speed of sound, c_s, and the kinematic viscosity, ν, are given by $c_s = \sqrt{\frac{1}{3}\frac{\Delta x}{\Delta t}}$ and $\nu = \frac{\tau-\frac{1}{2}}{3}\frac{\Delta x^2}{\Delta t}$, respectively [80]. The term $-\frac{\frac{1}{2}}{3}\frac{\Delta x^2}{\Delta t}$ in the expression for the kinematic viscosity of LBGK accounts for numerical viscosity. Due its special form it can be included as a correction factor in the simulated viscosity provided that the molecular velocities are such that particles travel to one of their neighboring points at each time step. Consequently the Lattice-BGK method is second-order accurate in space and time although it is based on first-order discretization schemes. However, if the molecular velocities are decoupled from the lattice one has to use second-order space and time discretization schemes to guarantee second-order accuracy, and the kinematic viscosity is then given by, $\nu = \frac{\tau}{3}\frac{\Delta_x^2}{\Delta t}$ [29].

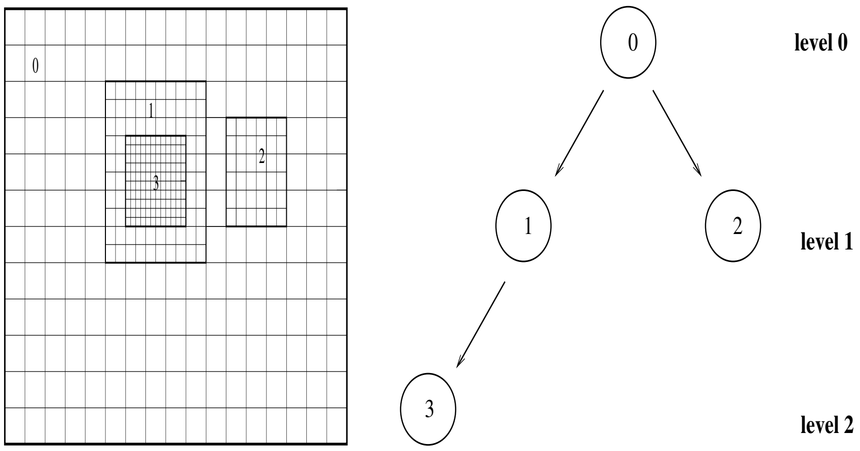

(a) (b)

Figure A.1: On the left an example of a nested grid is shown and on the right the corresponding hierarchical structure is depicted

A.4 Nested grids

A.4.1 Algorithm

The nested grid method is organized in a hierarchical way. The parent grid (with the coarsest grid resolution) may contain a number of child nodes with finer resolutions. These child nodes can be parent nodes of sub-grids with a finer grid resolution (see Fig. A.1). In the following we assume that the composite grid is built up of N different levels ($0..N-1$). The coarsest grid is the parent node and the grids with the finest resolution are the leaves of the tree. In the beginning of the simulations all the sub-grids are initialized to a uniform flow field. The time evolution of the Boltzmann scheme for the composite grid consists of the following phases (top down fashion),

1. The solution on the coarsest grid is first computed (level 0);

2. then the boundary conditions for the level 1 grids are interpolated from their parent sub-grid. We call this step 'the coarse to fine interpolation' and the solution on this level is advanced in time;

3. step 2 is repeated for levels 2 to $N-1$ recursively;

4. subsequently the boundary conditions for the level $N-2$ sub-grids are interpolated from the computed flow field of the $N-1$ grid ('fine to coarse interpolation') and the new values are computed as described in the previous step;

5. finally the same procedure is applied for level $N-2$ to level 0.

For simplicity, we use linear interpolation for computing the boundaries on the sub-grids. Another important aspect of this algorithm is a consistent coupling of the different sub-grids. In the next section we will discuss this issue.

A.4.2 Grid coupling

Besides the correct order of the different steps in the update scheme, there are physical constraints that should be satisfied in order to guarantee physical consistency between the different sub-grids, namely

- the speed of sound on all the sub-grids should be equivalent;
- the kinematic viscosity of the simulated fluid should be equivalent on all sub-grids.

One way to satisfy these constraints is by performing multiple time steps on the fine grids. For example if we consider two levels of refinements, a coarse and a fine one, with $\Delta x^{fine} = \frac{\Delta x^{coarse}}{2}$ (refinement factor is 2), then in order to simulate the same speed of sound on both grids we can take $\Delta t^{fine} = \frac{\Delta t^{coarse}}{2}$. Consequently, the relaxation parameter should also be rescaled such that the viscosity is the same on both grids. Additionally, the distribution functions also need to be rescaled. This approach has been proposed by Fillipova and Hanel [122].
An alternative way to couple the grids consistently is by making the molecular velocities $\mathbf{e}_i$ grid dependent (in lattice units)

$$\mathbf{e}_i = \alpha(cos(\frac{\pi}{2}(i-1)), sin(\frac{\pi}{2}(i-1)))\frac{\Delta x}{\Delta t}$$

for $i = 1,2,3,4$ and

$$\mathbf{e}_i = \alpha\sqrt{2}(cos(\frac{\pi}{2}(i-5)+\frac{\pi}{4}), sin(\frac{\pi}{2}(i-5)+\frac{\pi}{4}))\frac{\Delta x}{\Delta t}$$

for $i = 5,6,7,8$, where the α-parameter allows for an equal scaling of all discrete velocities.
Using mass and momentum conservation, $\rho\mathbf{u} = \sum_{i=0}^{N} f_i^{eq}$ and $\rho\mathbf{u} = \sum_{i=0}^{N} f_i^{eq}\mathbf{e}_i$, one can show that the equilibrium state should now be defined as,

$$f_i^{eq} = \rho\, w_i(1 + \frac{3(\mathbf{e}_i\cdot\mathbf{u})}{c^2\alpha^2} + \frac{9(\mathbf{e}_i\cdot\mathbf{u})^2}{2c^4\alpha^4} - \frac{3\mathbf{u}^2}{2c^2\alpha^2}). \tag{A.8}$$

This idea has similarities to the method first proposed by Koelman [123]. The speed of sound and the kinematic viscosity are given by [123],

$$c_s = \sqrt{\frac{1}{3}\frac{\alpha\Delta x}{\Delta t}} \tag{A.9}$$

$$\nu = \frac{\tau}{3}\frac{\alpha^2\Delta x^2}{\Delta t^2}. \tag{A.10}$$

Keeping the speed of sound and the kinematic viscosity equal on each grid resolution is simply accomplished by taking $\alpha\Delta x$ constant on each grid. Notice that the molecular velocities and the time step are completely determined by stability constraints on the fine grids.

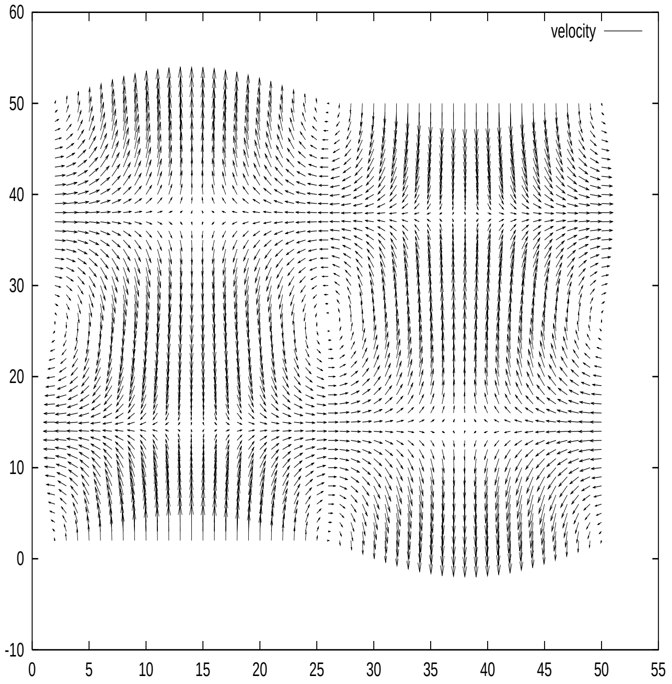

Figure A.2: The initial velocity u_x in the Taylor Vortex benchmark.

A.5 Preliminary results

We study the time dependent two-dimensional Taylor vortex problem (see Fig. A.2). In this benchmark the velocity (u_x, u_y) is initialized as follows,

$$u_x(x,y) = -u_0 cos(k_1 x) sin(k_2 y) \qquad and \qquad u_y(x,y) = u_0(\frac{k_1}{k_2}) sin(k_1 x) cos(k_2 y),$$

where k_1 and k_2 are given by $k_1 = \frac{2\pi m}{L}$ and $k_2 = \frac{2\pi n}{W}$. Here L and W are the dimensions of the systems. In this test case there is no driving force and the flow boundaries are periodic. It can be shown that the velocities will decay as follows

$$u_x(x,y,t) = -u_0 exp^{(-\nu t(k_1^2+k_2^2))} cos(k_1 x) sin(k_2 y), \tag{A.11}$$

$$u_y(x,y,t) = u_0(\frac{k_1}{k_2}) exp^{(-\nu t(k_1^2+k_2^2))} sin(k_1 x) cos(k_2 y). \tag{A.12}$$

We first verify the relation between the viscosity and the scaling factor α (Eq. A.10). These tests are performed on a single grid. The relaxation parameter $\tau = 1$ and $L = W = 50$. In Fig. A.3 we show the velocity at point $(\frac{L}{4}, \frac{W}{2})$ in the grid as a function of time for $\alpha = 0.1, 0.2, 0.3$ and 0.4. We clearly see that there is an exponential decay in time for each α. Moreover, the computed value of the decay exponent is in 1% agreement with the analytical value. In this figure we included the results obtained by the second-order central difference/Runge-Kutta methods. Similar results have been found for the second-order upwind/Runge-Kutta schemes (data not shown).

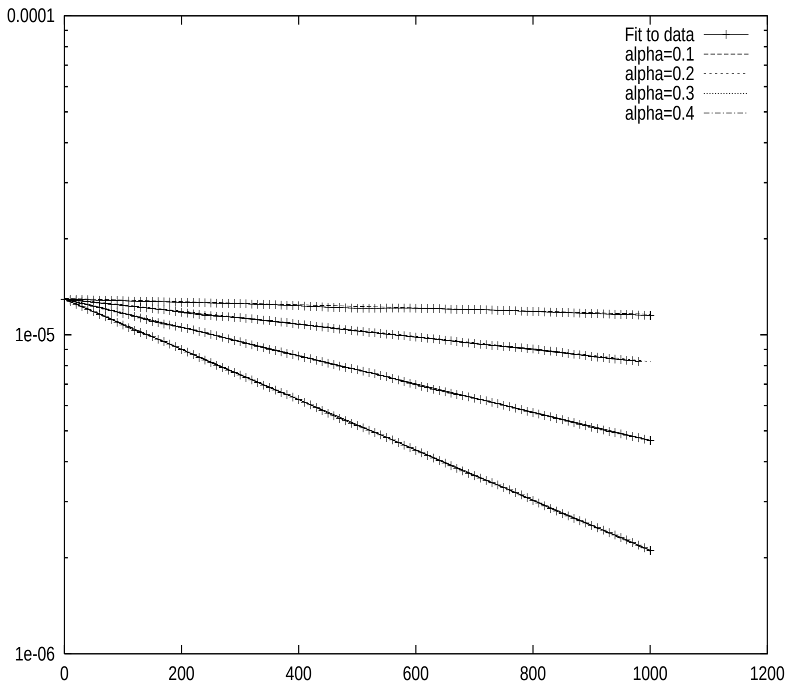

Figure A.3: The decay of the velocity in time at coordinate $(\frac{L}{4}, \frac{W}{2})$ for different values of α.

As a first validation of the method on nested grids, we studied the Taylor vortex evolution on computational lattice built up of a coarse and a fine grid. The fine grid is placed at the center of the domain. This choice is rather arbitrary because in this problem there are no clear regions with large differences in the computational error. However, this benchmark is still useful because it can demonstrate the consistency of the grid coupling and provide some insight in the error due to the first-order interpolation techniques used to compute the boundaries of the sub-grids. In these simulations we only allow coupling between the coarse to fine grid. In Fig. A.4.a we show the velocity profiles after 100 time steps at three lines parallel to the horizontal axes. We clearly see that there is a very good agreement between the solutions obtained on the fine and coarse grids. The error which is defined as the difference between the computed and the analytical value is shown in Fig. A.4.b. In the ideal case it is expected that the error is approximately four times smaller on the fine grid. However, we found that the error obtained on both grid resolutions are very close to each other. This might be due to the first-order interpolation schemes and the fact that in this test-case we do not refine in regions with high errors. These results still show that the physical behavior on the different grids is consistent. Similar results are found for other time steps $t = 1000$ and $t = 2000$ time-steps (see Figs. A.5 and A.6).

As argued above in this test case there are no clear regions with sharp error gradients. Moreover the test-case itself is simple. Thus more simulations including nonlinear flow problems need to be performed in order to demonstrate the computational efficiency and accuracy of our approach.

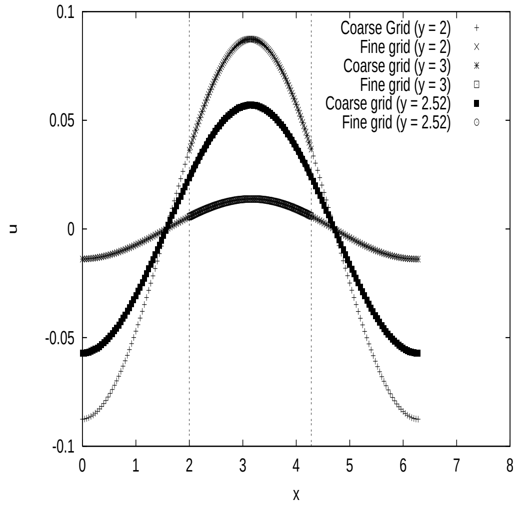

(a)

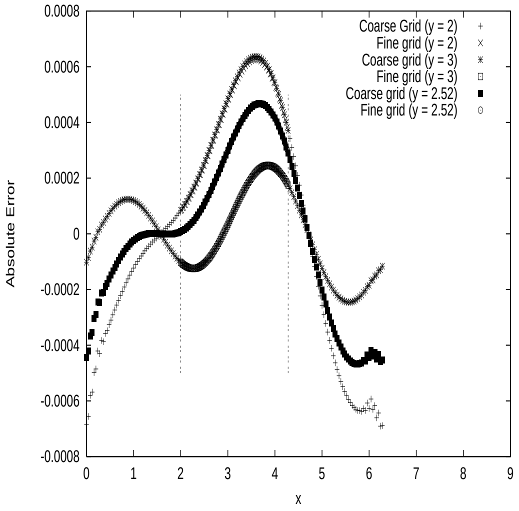

(b)

Figure A.4: The velocity at three lines parallel to the x-axis on both grid resolutions and the corresponding absolute errors at $t = 100$. The region between the dashed lines contains the fine grid.

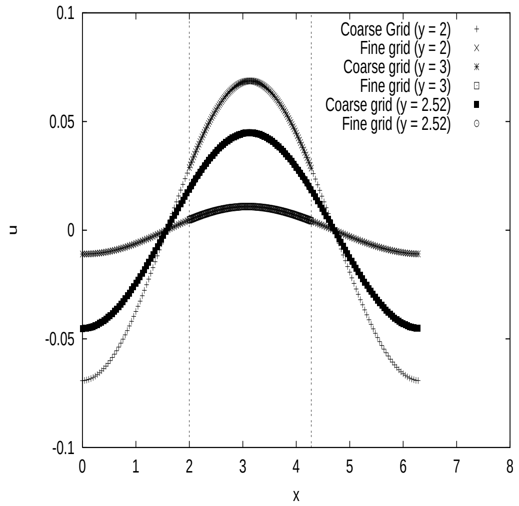

(a)

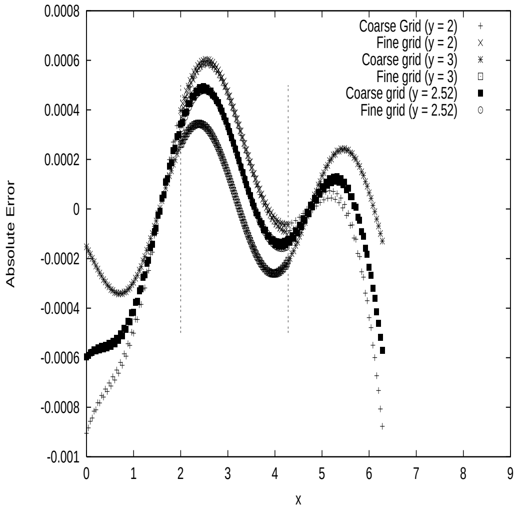

(b)

Figure A.5: The velocity at three lines parallel to the x-axis on both grid resolutions and the corresponding absolute errors at $t = 1000$. The region between the dashed lines contains the fine grid.

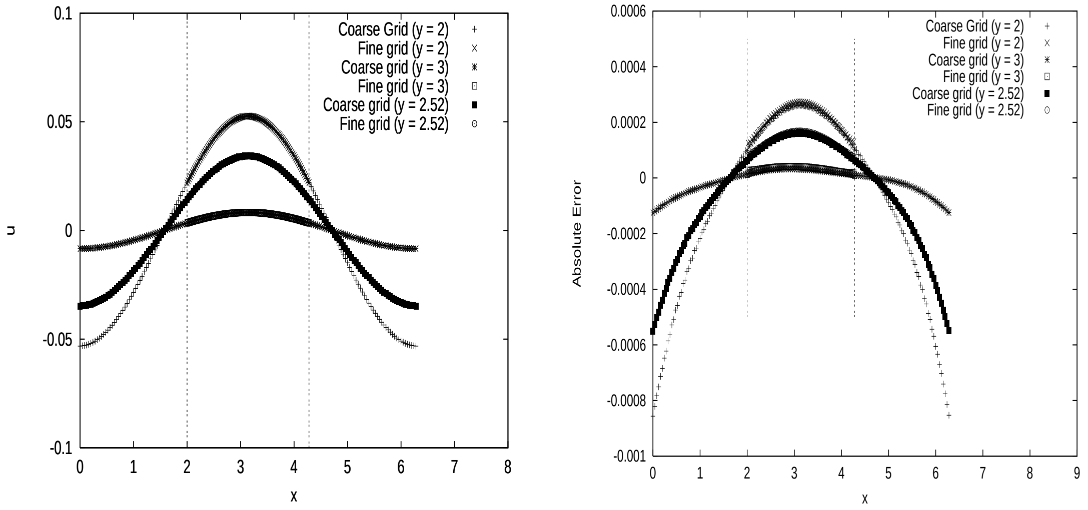

(a) (b)

Figure A.6: The velocity at three lines parallel to the x-axis on both grid resolutions and the corresponding absolute errors at $t = 2000$.The region between the dashed lines contains the fine grid.

A.6 Conclusion and Future Work

In this work we studied Lattice Boltzmann models on nested grids in 2D. The basic idea is to start from the continuous Boltzmann transport equation for a discrete set of velocities and to introduce a finite-difference approximation in space and time. The nested grid is built up of grids with an increasing resolution at different levels. The coupling between the different grid levels can be done by performing multiple time steps on the finer grids and rescaling the relaxation parameter, or by rescaling the lattice vectors and keeping the speed of sound and the kinematic viscosity constant on all the grids. The approach has been verified for the Taylor vortex benchmark. In the near future we will study more complicated flows, such as nonlinear flow in a backward facing step geometry, to verify our approach.

Bibliography

[1] L.D. Landau and E.M. Lifshitz. *Fluid Mechanics*. Pergamon Press Oxford, 1959.

[2] R.B. Bird, W.E. Stewart, and E.N. Lightfoot. *Transport Phenomena*. John Wiley & Sons, 1960.

[3] G.K. Batchelor. *An Introduction to Fluid Dynamics*. Cambridge University Press, 1967.

[4] D.J. Tritton. *Physical Fluid Dynamics*. Oxford Science Publications, 1988.

[5] F. M. White. *Fluid Mechanics*. McGraw-Hill Inc., 1994.

[6] J.A. Kaandorp, C. Lowe, D. Frenkel, and P.M.A. Sloot. The effect of nutrient diffusion and flow on coral morphology. *Phys. Rev. Lett.*, 77(11):2328, 1996.

[7] U. Frisch. *Turbulence*. Cambridge University Press, 1995.

[8] P.J. Roache. *Computational Fluid Dynamics*. Hermosa Publishers, 1976.

[9] R. Peyret and T.D. Taylor. *Computational Methods for Fluid Flow*. Springer-Verlag, 1983.

[10] L.G. Richardson. *Weather Prediction by Numerical Process*. Cambridge University Press, 1922.

[11] G.J. Haltiner and R.T. Williams. *Numerical Prediction and Dynamical Meteorology*. John Wiley & Sons, New-York, 1980.

[12] D. H. Rothman and S. Zaleski. *Lattice gas cellular automata*. Cambridge University Press, 1997.

[13] U. Frish, B. Hasslacher, and Y. Pomeau. Lattice-gas automata for the navier-stokes equation. *Phys. Rev. Lett.*, 56:1505, 1986.

[14] J. Hardy, Y. Pomeau, and O. de Pazzis. Time evolution of a two-dimensional model system. i. invariant states and time correlation functions. *J. Math. Phys.*, 14:1746, 1973.

[15] J. Hardy, O. de Pazzis, and Y. Pomeau. Molecular dynamics of a classical lattice gas: Transport properties and time correlation functions. *Phys. Rev. A*, 13:1949, 1976.

[16] B. Chopard and M. Droz. *Cellular Automata Modeling of Physical Systems*. Cambridge University Press, 1998.

[17] K. Huang. *Statistical Mechanics*. John Wiley and Sons, New York, second edition, 1987.

[18] P. Grosfils, J.P. Boon, and P. Lallemand. Spontaneous fluctuation correlations in thermal lattice-gas automata. *Phys. Rev. Lett.*, 68:1077, 1992.

[19] M.A. van der Hoef. *Simulation study of diffusion in lattice-gas fluids and colloids*. PhD thesis, University Utrecht, december 1992.

[20] P. Résibois and M. Leener. *Classical Kinetic Theory of Fluids*. John Wiley, 1977.

[21] Y.H. Qian, D.d'Humieres, and P. Lallemand. Lattice bgk models for the navier-stokes equation. *Europhys. lett.*, 17(6):479, 1992.

[22] S. Chen, Z. Wang, X. Shan, and G. Doolen. Lattice-boltzmann computational fluid dynamics in three dimensions. *J. Stat. Phys.*, 68(3/4):379, 1992.

[23] X. He and L.S. Luo. A *priori* derivation of the lattice boltzmann equation. *Phys. Rev. E*, 55(6):R6333, 1997.

[24] S. Hou, Q. Zou, S. Chen, G. Doolen, and A. C. Cogley. Simulation of cavity flow by the lattice-boltzmann method. *J. Comp. Phys.*, 118:329, 1995.

[25] G. McNamara and G. Zanetti. Use of the boltzmann equation to simulate lattice-gas automata. *Phys. Rev. Lett.*, 61:2332, 1988.

[26] F.J. Higuera and J. Jimenez. Boltzmann approach to lattice-gas simulations. *Europhys. lett.*, 9(7):663, 1989.

[27] F.J. Higuera, S. Succi, and R. Benzi. Lattice gas dynamics with enhanced collision. *Europhys. lett.*, 9:345, 1989.

[28] R. Benzi, S. Succi, and M. Vergassola. The lattice-boltzmann equation: Theory and applications. *Phys. Rep.*, 222(3):145, 1992.

[29] N. Cao, S. Chen, S. Jin, and D. Martinez. Physical symmetry and lattice symmetry in the lattice boltzmann method. *Phys. Rev. E*, 55(1):55, 1997.

[30] B.M. Boghosian, J. Yepez, F.J. Alexander, and N.H. Margolus. Integer lattice gases. *Phys. Rev. E*, 55:4137, 1997.

[31] P.A. Skordos. Initial and boundary conditions for the lattice-boltzmann method. *Phys. Rev. E*, 48(6):4823, 1993.

[32] D. Noble, J. Georgiadis, and R. Buckius. Direct assessment of lattice boltzmann hydrodynamics and boundary conditions for recirculating flows. *J. Stat. Phys*, 81:17, 1995.

[33] D. Noble, S. Chen, J. Georgiadis, and R. Buckius. A consistent hydrodynamic boundary condition for the lattice boltzmann method. *Phys. Fluids*, 203:7, 1995.

[34] S. Chen, D. Martinez, and R. Mei. On boundary conditions in lattice boltzmann methods. *Phys. Fluids*, 8:2527, 1996.

[35] R.S. Maier, R.S. Bernard, and D.W. Grunau. Boundary conditions for the lattice-boltzmann method. *Phys. Fluids*, 8(7):1788, 1996.

[36] D.R. Noble, J.G. Georgiadis, and R.O. Buckius. Comparison of accuracy and performance for lattice-boltzmann and finite difference simulations of steady viscous flow. *Int. J. Numer. Meth. Fluids*, 23:1, 1996.

[37] O. Filippova and D. Hänel. Lattice boltzmann simulation of gas-particle flow in filters. *Computers & Fluids*, 697:26, 1997.

[38] M.A. Gallivan, D.R. Noble, J.G. Georgiadis, and R.O. Buckuis. An evaluation of the bounce-back boundary condition for lattice boltzmann simulations. *Int. J. Numer. Meth. Fluids*, 25:249, 1997.

[39] L.S. Luo X. He, Q. Zou and M. Dembo. Analytical solutions of simple flow and analysis of non-slip boundary conditions for the lattice boltzmann bgk model. *J. of Stat. Phys.*, 87:115, 1996.

[40] A.J.C. Ladd. Numerical simulations of particulate suspensions via a discretized boltzmann equation. part 1. theoretical foundation. *J. Fluid Mech.*, 271:285, 1994.

[41] A. J.C. Ladd. Numerical simulations of particulate suspensions via a discretized boltzmann equation. part 2. numerical results. *J. Fluid Mech.*, 271:311, 1994.

[42] C.L. Aidun and Y. Lu. Lattice-boltzmann simulations of solid particles suspended in fluid. *J. Stat. Phys.*, 81(1):49, 1995.

[43] O.Behrend. Solid-fluid boundaries in particle suspension simulations via the lattice-boltzmann method. *Phys. Rev. E*, 52(1):1164, 1995.

[44] I. Ginzbourg and P. Adler. Boundary flow condition analysis for the three-dimensional lattice boltzmann method. *J. Phys. II France*, 4:191, 1994.

[45] M. Yoshino T. Inamuro and F. Ogino. A non-slip boundary condition for lattice boltzmann simulations. *Phys. Fluids*, 7:2928, 1995.

[46] I. Ginzbourg and D. d'Humiéres. Local second-order boundary methods for lattice boltzmann models. *J. Stat. Phys.*, 84:927, 1996.

[47] L. Wagner. Pressure in lattice boltzmann simulations of flow around a cylinder. *Phys. Fluids*, 6:3516, 1994.

[48] A. Koponen, D. Kandhai, E. Hellén, M. Alava, A. Hoekstra, M. Kataja, K. Niskanen, P. Sloot, and J. Timonen. Permeability of three-dimensional random fiber webs. *Phys. Rev. Lett.*, 80:716, 1998.

[49] B. Ferréol and D. H. Rothman. Lattice-boltzmann simulations of flow through fontainebleau sandstone. *Transp. Porous Media*, 20:3, 1995.

[50] D. Koch and A. Ladd. Moderate reynolds number flows through periodic and random arrays of aligned cylinders. *J. Fluid Mech.*, 31:439, 1997.

[51] L.-S. Luo. Symmetry breaking of flow in 2d symmetric channels: Simulations by lattice-boltzmann method. *International Journal of Modern Physics C*, 8(4):859, 1997.

[52] Y.H. Qian, S. Succi, and S.A. Orszag. Recent advances in lattice-boltzmann computing. *Annu. Rev. Comp. Phys. III*, page 195, 1995.

[53] W. Miller. Flow in the driven cavity calculated by the lattice boltzmann method. *Phys.Rev. E*, 51:3659, 1995.

[54] D. Kandhai, D. Vidal, A. Hoekstra, H. Hoefsloot, P. Iedema, and P.M.A. Sloot. Lattice-boltzmann and finite element simulations of fluid flow in a smrx mixer. *Int. J. Numer. Meth. Fluids*. In press.

[55] D. Kandhai, A. Koponen, A. Hoekstra, M. Kataja, J. Timonen, and P.M.A. Sloot. Implementation aspects of 3d lattice-bgk: Boundaries, accuracy and a new fast relaxation method. *J. Comp. Phys.*, 150:482, 1999.

[56] E.S. Mickaily-Huber, F. Bertrand, P. Tanguy, T. Meyer, Albert Renken, Franz S. Rys., and Marc Wehrli. Numerical simulations of mixing in an smrx static mixer. *Chem. Eng. J.*, 63:117, 1996.

[57] K.J. Niskanen and M.J. Alava. Planar random networks with flexible fibers. *Phys. Rev. Lett.*, 73:3475, 1994.

[58] J.P. Barford. A mathematical model for cell separation technique of centrifugal elutration. *Biotechnology and Bioengineering*, XXVIII:570, 1986.

[59] J. Haataja and S. Saarinen. *Cray T3E User's Guide*. Center for Scientific Computing, Finland, 1997.

[60] G.C. Fox, R.D. Williams, and P.C. Messina. *Parallel Computing Works!* Morgan Kaufmann Publishers, Inc., 1994.

[61] P.A. Skordos. Parallel simulation of subsonic fluid dynamics on a cluster of workstations. In *Proceedings of High Performance Distributed Computing 95*, number 4th IEEE International Symposium, 1995.

[62] P. Giovanni, F. Massaioli, and S. Succi. High-resolution lattice-boltzmann computing on the ibm sp1 scalable parallel computer. *Comp. Phys.*, 8(6):705, 1994.

[63] D.R. Noble, S. Chen J.G. Georgiadis, and R.O. Buckius. A consistent hydrodynamic boundary condition for the lattice-boltzmann method. *Phys. Fluids*, 7(1):203, 1995.

[64] P. S. Pachero. *Parallel Programming with MPI.* Morgan Kaufmann Publishers, Inc., 1997.

[65] P.M.A. Sloot, M.J. Carels, P. Tensen, and C.G. Figdor. Computer assisted centrifugal elutriation i:1 detection system and data acquisition equipment. *Comp. Meth. Prog. Biomed.*, 8:179, 1987.

[66] P.M.A. Sloot, E.H.M. van der Donk, and C.G. Figdor. Computer assisted centrifugal elutriation ii: Multiparametric statistical analysis. *Comp. Meth. Prog. Biomed.*, 27:37, 1988.

[67] C.G. Figdor. *Separation of human leukocytes by physical methods.* PhD thesis, University of Amsterdam, 1982.

[68] J.F. de Ronde, A. Schoneveld, and P.M.A. Sloot. Load balancing by redundant decomposition and mapping. *Future Generation Computer Systems*, 12(5):391, 1997.

[69] F. Nannelli and S. Succi. The lattice-boltzmann equation on irregular lattices. *J. Stat. Phys.*, 68:401, 1992.

[70] A. Schoneveld and J.F. de Ronde. P-cam: A framework for parallel complex systems simulations. to appear in FGCS (special issue on Cellular Automata).

[71] B.J. Overeinder, P.M.A. Sloot, R.N. Heederik, and L.O. Hertzberger. A dynamic load balancing system for parallel cluster computing. *Future Generation Computer Systems*, 12:101, 1996.

[72] M. Mutsakis, F.A. Streiff, and G. Schneider. Advances in static mixing technology. *Chem. Eng. Prog.*, 82:42, 1986.

[73] Gary D. Doolen, editor. *Lattice Gas Methods For Partial Differential Equations*, volume IV of *Studies in the Sciences of Complexity*. Santa Fe Institute, Addison-Wesley Publishing Company, 1990.

[74] L.A.J. van Dijck and L.L van Dierendonck. Sulzer mixer reactor: Experimental verification of the computer simulations of the hydrodynamic behavior. *Project Report, Ecole Polytechnique Fédérale de Lausanne*, 1992.

[75] J. Gyenis and T. Blickle. Simulations of mixing during nonsteady state particle flow in static mixer tubes. *Acta Chim. Hung.*, 129:647, 1992.

[76] A. Bakker and R. LaRoche. Flow and mixing with kenics static mixers. *Cray Channels*, 15:25, 1993.

[77] F. Bertrand, P.A. Tanguy, and F. Thibault. A numerical study of the residence time distribution in static mixing. *Int. Chem. Eng. Symposium Series*, 136:163, 1994.

[78] P.A. Tanguy, F. Betrand, R. Lacroix, L. van Dijck, T. Meyer, and A. Renken. Finite element flow simulations in an smrx static mixer. In *Engineering Foundation Conferences: Mixing XIV*, Santa Barbara, CA, 1996.

[79] T. Avalosse and M.J. Crochet. Finite-element simulation of mixing: Three-dimensional flow through a kenics mixer. *AIChE Journal*, 43:588, 1997.

[80] S. Chen and G.D. Doolen. Lattice boltzmann method for fluid flows. *Annu. Rev. Fluid Mech.*, 30:329, 1998.

[81] S. Segal C. Cuvelier and A. A. van Steenhoven. *Finite Element Methods and Navier-Stokes Equations*. Reidel Publishing Company, Dordrecht, 1986.

[82] M.P. Robichaud, P.A. Tanguy, and M. Fortin. An iterative implementation of the uzawa algorithm for 3-d fluid flow problems. *Int. J. Numer. Meth. Fluids*, 10:429, 1990.

[83] P.A. Tanguy, M. Fortin, and L. Choplin. Finite element simulation of dip coating, ii: Non-newtonian fluids. *Int. J. Numer. Meth. Fluids*, 4:441, 1984.

[84] M. Fortin. Old and new finite elements for incompressible flows. *Int. J. Numer. Meth. Fluids*, 1:347, 1981.

[85] F. Bertrand, M. Gadbois, and P.A. Tanguy. Tetrahedral elements for fluid flow problems. *Int. J. Numer. Meth. Eng.*, 33:1251, 1992.

[86] X. He, L.S. Luo, and M. Dembo. Some progress in lattice-boltzmann methods. part i. nonuniform mesh grids. *Journal of Computational Physics*, (129):357, 1996.

[87] F.M. White. *Viscous Fluid Flow*. McGraw-Hill, 1974.

[88] D. Kandhai, A. Koponen, A. Hoekstra, M. Kataja, J. Timonen, and P.M.A. Sloot. Lattice-boltzmann hydrodynamics on parallel systems. *Computer Physics Communications*, 111:14, 1998.

[89] F. Bertrand, P.A. Tanguy, and F. Thibault. A three-dimensional fictitious domain method for incompressible fluid flow problems. *Int. J. Numer. Meth. Fluids*, 25:1, 1997.

[90] R. Glowinski, T. Pan, and J. Périaux. A fictitious domain method for external incompressible viscous flow problems modelled by navier-stokes equation. *Comp. Meth. Appl. Eng.*, 112:133, 1994.

[91] Y.H. Qian and Y.F. Deng. A lattice bgk model for viscoelastic media. *Phys. Rev. Lett.*, 79:2742, 1997.

[92] S. Hou, J. Sterling, S. Chen, and G.D. Doolen. A lattice subgrid model for high reynolds number flows. *Fields Institute Communications*, 6:151–166, 1996.

[93] D. Grunau, S. Chen, and K. Eggert. A lattice-boltzmann model for multiphase fluid flow. *Phys. Fluids A*, 5:2557, 1993.

[94] J. Bear. *Dynamics of Fluids in Porous Media*. Dover, 1972.

[95] M. Sahimi. *Flow and Transport in Porous Media and Fractured Rock*. VCH, Weinheim, 1995.

[96] S. Kostek, L. M. Schwartz, and D. L. Johnson. Fluid permeability in porous media: Comparison of electrical estimates with hydrodynamical calculations. *Phys. Rev. B*, 45:186, 1992.

[97] A. H. Thompson, S. W. Sinton, S. L. Huff, A. J. Katz, R. A. Raschke, and G. A. Gist. Deuterium magnetic resonance and permeability in porous media. *J. Appl. Phys.*, 65:3259, 1989.

[98] D.L. Johnson, D.L. Hemmick, and H. Kojima. Probing porous media with first and second sound. i. dynamic permeability. *J. Appl. Phys.*, 76:104, 1994.

[99] U. Frisch, D. d'Humiéres, B. Hasslacher, P. Lallemand, Y. Pomeau, and J.-P. Rivet. Lattice gas hydrodynamics in two and three dimensions. *Comples Syst.*, 1:649, 1987.

[100] A. Cancelliere, C. Chang, D.H. Rothman E. Foti, and S. Succi. The permeability of a random medium: comparison of simulation with theory. *Phys. Fluids A*, 2:2085, 1990.

[101] N.S. Martys and H. Chen. Simulation of multicomponent fluids in complex three-dimensional geometries by the lattice boltzmann method. *Phys. Rev. E*, 53:743, 1996.

[102] G.W. Jackson and D.F. James. Permeability of fibrous media. *Can. J. Chem. Eng.*, 64:364, 1986.

[103] I. Langmuir. Report of smokes and filters. In Rodebush et al., editor, *Filtration of Aerosols and the development of Filter Materials*, volume 865 of *Part IV of a report for the office of scientific research and development*. 1942.

[104] J. E. Drummond and M.I. Tahir. Laminar viscous flow trough regular arrays of parallel solid cylinders. *Int. J. Multiphase Flow*, 10:515, 1984.

[105] A.S. Sangani and A. Acrivos. Slow flow past periodic arrays of cylinders with application to heat transfer. *Int. J. Multiphase Flow*, 8:193, 1982.

[106] G.W. Jackson and D.F. James. The hydrodynamic resistance of hyaluronic acid and its contribution to tissue permeability. *Biorheology*, 19:317, 1982.

[107] J.J.L. Higdon and G.D. Ford. Permeability of three-dimensional models of fibrous porous media. *J. Fluid Mech.*, 308:341, 1996.

[108] C.K. Ghaddar. *Phys. Fluids*, 7:2563, 1995.

[109] I.L. Clayes and J.F. Brady. Suspensions of prolate spheroids in stokes flow. *J. Fluid Mech.*, 251:443, 1993.

[110] D.S. Clague and R.J. Philips. A numerical calculation of the hydraulic permeability of 3-dimensional disordered fibrous media. *Phys. Fluids*, 9(6):1562, 1997.

[111] E. Héllen, M.J. Alava, and K.J. Niskanen. Porous structure of thick fiber webs. *J. Appl. Phys.*, 81:6425, 1997.

[112] K. Niskanen, N. Nilsen, E. Hellen, and M. Alava. In C.F. Baker, editor, *The Fundamentals of Papermaking Materials*, Leatherhead, UK, 1997. Pira Int.

[113] D.S. Clague and R.J. Philips. Hindered diffusion of spherical macromolecules in dilute fibrous media. *Phys. Fluids*, 8:1720, 1996.

[114] D.S. Clague, D. Kandhai, R. Zhang, and P.M.A. Sloot. On the hydraulic permeability of (un)bounded fibrous media using the lattice-boltzmann method. *Phys. Rev. E*. Submitted.

[115] W.L. Ingmanson, B.D. Andrews, and R.C. Johnson. *TAPPI*, 42:840, 1959.

[116] S. T. Han. Compressibility and permeability of fibre mats. *Pulp Paper Mag. Can.*, 70:T134, 1969.

[117] R. Tsay and S. Weinbaum. Viscous flow in a channel with periodic croos-bridging fibres: exact solutions and brinkman approximation. *J. Fluid Mech.*, 226:125, 1991.

[118] A.G. Ogston. The spaces in uniform random suspension of fibers. *Trans. Faraday Soc.*, 54:1754, 1958.

[119] R. Verberg and A.J.C. Ladd. Simulation of low-reynolds-number flow via a time-independent lattice-boltzmann method. *Phys. Rev. E*, 60(3):3366, 1999.

[120] Renwei Mei and Wei Shyy. On the finite difference-based lattice boltzmann method in curvilinear coordinates. *J. Comp. Phys.*, 143:426, 1998.

[121] Gongwen Peng, Haowen Xi, Comer Duncan, and So-Hsiang Chou. Finite volume scheme for the lattice boltzmann method on unstructured meshes. *Phys. Rev. E*, 59(4):4675, 1999.

[122] O. Filippova and D. Hanel. Boundary-fitting and local grid refinement for lattice-bgk models. *Int. J. Mod. Phys. C*, 9(8):1271, 1998.

[123] J.M.V. A Koelman. A simple lattice boltzmann scheme for navier-stokes fluid flow. *Europhys. Lett.*, 15(6):603, 1991.

Summary

A wide variety of applications stemming from the natural sciences and engineering are strongly related with the motion of fluids. Some typical examples are, the atmospheric circulation processes, flow of blood through complex capillary vessels, ground water pollution, compressible flow around an airfoil, and numerous other interesting problems which are of great relevance for the industrial and academic community. A good understanding of the dynamics of fluids is therefore extremely useful in improving several industrial processes and designs, e.g. the wing of an airplane, and may contribute significantly to our knowledge of many fundamental scientific problems, e.g. the impact of hydrodynamics on the morphology of biological growth forms. Although the basic equations for describing the motion of fluids are known for a long time a general solution to flow phenomena does still not exist.

The Lattice Boltzmann method (LBM) is a relatively new approach for the numerical simulation of fluid flow. In this method fluid is modeled by particles moving on a regular lattice. At each time step the particles propagate to neighboring lattice points and re-distribute their velocities in a local collision phase. This inherent spatial and temporal locality of the update rules makes it ideal for parallel processing. The main objective of this thesis is to study realistic fluid dynamical problems by means of the lattice Boltzmann method on parallel systems. The thesis focusses on computational aspects and new physical insights related to fluid flow in porous media.

In chapter 3 the accuracy of the bounce-back scheme for stair-cased geometries is studied by simulating fluid flow in an inclined tube. Similar to the case of flat walls, a first-order dependence of the relative error on the grid spacing has been found due to the shift of the boundaries. For a specific inclination angle of 45 degrees, the relative error is second-order convergent in lattice spacing when the location of the wall is assumed to lie half-way between the solid nodes and the last fluid nodes. Besides the study related to the bounce-back boundary condition, boundaries for driving a flow between the inlet and outlet of the system are considered. In this context a comparison is made between the well-known body-force approach and pressure boundaries. For low Reynolds numbers and simple geometries a good agreement between these approaches has been found. Apart from the evaluation of the boundary conditions, two common implementations of the lattice-Boltzmann model for $3D$ simulations are studied, the D_3Q_{15} and the D_3Q_{19} models. It is shown that within the D_3Q_{15} model, an unphysical checkerboard effect can be found, which generates spurious conservation of mo-

mentum and mass within two distinct populations of particles. For some stationary flows, this checkerboarding effect generates unphysical patterns in the hydrodynamic fields. However, in the test cases the overall effect of these artifacts is negligible.

Next, parallelization of LBM simulations is revisited. The need for studying this issue, is that often implementation of LBM simulations on parallel systems, is based on decomposition of the computational grid in equal sub volumes (slice and box decomposition). However, it is known that the computational cost of LBM simulations scales linearly with the number of fluid nodes. The obstacle points do not contribute significantly to the total computation time. It is thus obvious that efficient parallelization for a wide range of applications can only be obtained by using appropriate load balancing methods. In this context load balancing of LBM simulations by means of the Orthogonal Recursive Bisection method is studied. For fluid flow in a centrifugal elutriation chamber, a 12 to 60% increase in speed has been gained compared to the slice and box decompositions.

Furthermore, a detailed validation of LBM and traditional finite element methods (FEM) for fluid flow in complex geometries is performed. As a realistic test case fluid flow in a static mixer reactor has been considered. In this validation study the numerical results for the velocity and the pressure of LBM are compared rigorously with FEM calculations and experimental data. A good agreement between both methods and experimental data has been found. It appears that the LBM is less memory consuming and uses computational times comparable to the FEM for the same level of accuracy of the simulations. However, there may be cases where the FEM method is more efficient, e.g. due to the uniform nature of the LBM grids. LBM yields similar accuracy between pressure and velocity fields, whereas the FEM could exhibit a rather good estimate of the velocity field combined with a bad estimate of the pressure field due to mesh coarseness. LBM can therefore be considered as a simple alternative for simulating laminar flow in complex geometries. However, the execution times of the LBM methods show a sharp increase on very fine meshes.

To cope with this shortcoming two refinements on the LBM method are proposed, namely an iterative momentum relaxation (IMR) technique to decrease the number of time steps that are required to reach a steady-state and LBM simulations on nested grids. The IMR technique is based on an iterative adjustment of the local body-force. It has been validated on three test cases, namely fluid flow around a spherical obstacle, flow in random fiber mats and flow in a static mixer reactor. In the first test case the IMR method appears to be around 35 times faster, whereas for the more complicated benchmarks, the IMR method is approximately 3 times faster. Notice that for realistic runs the benefit gained by IMR is still significant. In the second refinement the LBM method has been extended to computational grids consisting of multiple nested grids with increasing spatial resolution. Basically, the discrete velocity Boltzmann equation is solved numerically on each sub-lattice and interpolation between the interfaces is carried out in order to couple the sub-grids consistently. This approach has been validated on the simple Taylor vortex flow benchmark. Although this work is still quite preliminary the first results are promising. In the near future our aim is to apply this technique to more complicated problems.

In the last chapter, a study on the hydrodynamic properties of fibrous media is presented. Despite the numerous experimental and theoretical studies, the hydrodynamic properties of disordered fibrous porous media are still poorly understood. The existing numerical studies are only valid for dilute systems or they completely neglect the typical disorder of real 3D fibrous media. The behavior of the hydraulic permeability as a function of the fiber volume fraction for many ordered and disordered models of fibrous media for a large range of fiber volume fractions has been calculated and compared rigorously with existing theoretical, numerical and experimental data. For the ordered media, namely SC and BCC configurations, a good agreement is found between our simulations and existing theoretical and numerical data for the complete range of fiber volume fractions. For disordered fibrous media a good agreement between LBM, the analytical results of Jackson and James and the empirical Kozeny-Carman equation is found in the dilute limit, as expected. Moreover, the results suggest an exponential dependence of permeability on fiber volume fraction in a wide range and this functionality seems to be a generic feature of fibrous porous materials, independent of whether they are random or not.

Using simple scaling arguments, it is argued that there is a strong correlation between the hydraulic permeability and the distance between the fibers. This correlation is further explored and used as a possible explanation of the behavior of the hydraulic permeability as a function of the fiber volume fraction.

Finally, the effect of wall boundaries on the hydraulic permeability has been studied by simulating fluid flow in fibrous media placed between two parallel plates (the so-called bounded media). Although many realistic fibrous media are bounded there are not many theoretical studies reported on this topic. This is mainly due to singularities introduced by the parallel plates. For various wall separation distances the hydraulic permeability is computed for a bi-periodic array of cylinders and a disordered medium as a function of the fiber volume fraction. These results are compared with the effective medium theory of Tsay and Weinbaum. For bounded ordered media a reasonably good agreement is found in the dilute limit. For higher fiber volume fraction the effective medium theory of Tsay and Weinbaum overpredicts the permeability. From the strong correlation between the average fiber-fiber distance and the hydraulic permeability, a phenomenological expression is derived based on the effective medium theory of Tsay and Weinbaum. This correlation appears to be valid for a larger range of fiber volume fractions and can be used for a rapid prediction of the hydraulic permeability of bounded fibrous media.

Samenvatting

Een grote verscheidenheid aan natuurwetenschappelijke en technische problemen hebben te maken met vloeistofstromingen. Enkele typische voorbeelden zijn luchtcirculatie in de atmosfeer, stroming rondom vliegtuigvleugels, bloedstroming door complexe vatenstelsels, grondwatervervuiling en vele andere problemen die zeer relevant zijn voor de wetenschap en industrie. Een goed begrip van vloeistofdynamica kan daarom uitermate belangrijk zijn voor de optimalisatie van diverse industriële processen en kan een belangrijke bijdrage leveren aan onze kennis van vele fundamentele wetenschappelijke vragen. Ondanks het feit dat de vergelijkingen voor het beschrijven van vloeistofstromingen al vrij lang bekend zijn, bestaat er nog geen algemene oplossing voor dit probleem.

Een veel gebruikte aanpak om enigszins inzicht te verkrijgen is via numerieke simulaties. De rooster-Boltzmann methode is een vrij nieuwe benadering voor de numerieke simulatie van vloeistofstromingen. In deze methode wordt een vloeistof gemodelleerd d.m.v. deeltjes die zich in een beperkt aantal richtingen bewegen op een regelmatig rooster. In elke tijdstap bewegen de deeltjes zich eerst naar een naburige roosterpunt waarna vervolgens botsingen plaatsvinden, waarin de deeltjes hun snelheden op een bepaalde manier herverdelen. De inherente lokaliteit in tijd en ruimte van deze regels heeft als gevolg dat deze methode uitermate geschikt is voor de berekening op geavanceerde parallelle computerarchitecturen. In dit proefschrift wordt de rooster-Boltzmann methode gebruikt om diverse realistische toepassingen te simuleren op parallelle computers. De nadruk ligt op computationele aspecten en op het verkrijgen van nieuwe fysische inzichten voor de transporteigenschappen van poreuze media opgebouwd uit vezels.

In hoofdstuk 3 wordt de nauwkeurigheid van de *bounce-back* methode in onregelmatige geometrieën bestudeerd. Dit wordt gedaan d.m.v. stroming in een geroteerde pijp als testprobleem. De *bounce-back* methode is een simpele en generieke methode voor het specificeren van de condities op de wand van een obstakel. Het blijkt dat de methode eerste-orde nauwkeurig is, indien in de analyse de locatie van de *non-slip* wand (de positie waarop de snelheid precies nul is) verondersteld wordt op het roosterpunt waar de *bounce-back* wordt uitgevoerd. Het is namelijk zo dat de effectieve locatie van de *non-slip* wand enigszins verschoven is. Voor het specifieke geval waarbij de rotatiehoek gelijk is aan 45 graden, blijkt de methode tweede-orde nauwkeurig te zijn, indien in de analyse rekening wordt gehouden met de verschuiving van de effectieve locatie

van de *non-slip* wand. Deze bevindingen zijn consistent met die van een vlakke pijp. Naast de *bounce-back* methode zijn randcondities bekeken waarmee men een stroming kan aandrijven. Hierbij is een vergelijking gemaakt tussen de veel gebruikte *body-force* methode en drukranden. Voor stromingen in het lage Reynoldsgetal-regime is er een goede overeenstemming tussen beide methoden. Verder zijn de meest gangbare driedimensionale rooster-Boltzmann modellen, de D_3Q_{15} en de D_3Q_{19} modellen, bestudeerd. Er wordt geïllustreerd dat in het D_3Q_{15} model een artefact aanwezig is, waardoor het gesimuleerde vloeistof in feite opgesplitst is in twee afzonderlijke gedeelten volgens het zwart-wit schaakbordpatroon. Voor een aantal testgevallen kan dit leiden tot onfysische resultaten welke in het algemeen verwaarloosbaar zijn.
Hierna is de implementatie van de rooster-Boltzmann methode op parallelle systemen bekeken. Ten eerste is gekeken naar het gedrag van de rekentijd als functie van het aantal processoren en voor variërende probleemgrootte. Parallellisatie van de meeste rooster-Boltzmann simulaties is vaak gebaseerd op het opsplitsen van het rooster in volumes met een ongeveer gelijk aantal roosterpunten. Hierbij wordt geen rekening gehouden met het feit dat er gebieden kunnen zijn waar helemaal niet hoeft te worden gerekend. In onze aanpak gebruiken wij de Orthogonale Recursieve Bisectie methode om het domein op te splitsen in stukken met min of meer gebalanceerd rekenwerk. Het gevolg is dat de communicatiestructuur tussen de verschillende processoren onregelmatig kan zijn. Voor stroming in een centrifugale elutriatorgeometrie is deze strategie twaalf tot zestig procent efficiënter ten opzichte van de bovengenoemde naïeve parallellisatiestrategiëen.
Vervolgens is een gedetailleerd validatie-experiment uitgevoerd, waarbij de resultaten van de rooster-Boltzmann methode werden vergeleken met die van de wereldwijd geaccepteerde eindige-elementen methode en experimentele data. Als testprobleem is vloeistofstroming in de complexe SMRX statische mixer reactor genomen. De overeenstemming tussen de beide simulatiemethoden en de experimentele data was verrassend goed. Voor het verkrijgen van een redelijke nauwkeurigheid bleek de rooster-Boltzmann methode minder geheugen en een vergelijkbare computertijd dan de eindige-elementen methode, nodig te hebben. Verder bleek de rooster-Boltzmann methode voor zowel de snelheids- als de drukprofielen een vergelijkbare nauwkeurigheid te hebben. De eindige-elementen methode kan echter resulteren in een vrij goede voorspelling van de snelheidsprofielen terwijl de drukval vrij incorrect kan zijn wanneer lineaire elementen gebruikt worden. De rooster-Boltzmann methode daarentegen blijkt vrij inefficiënt te zijn voor heel fijne gridresoluties.
Om deze tekortkoming enigszins tegemoet te komen, zijn twee verfijningen aangebracht op de methode, namelijk de Iteratieve Momentum Relaxatie (IMR) methode om het aantal tijdstappen te reduceren die nodig zijn voor de convergentie naar een stationair toestand, en de uitbreiding van de rooster-Boltzmann methode naar geneste grids. De IMR methode is gebaseerd op een iteratief proces waarin de *body-force* wordt aangepast, zodat eerder een stationair toestand wordt bereikt. Voor stroming rondom een bol bleek het ongeveer 35 keer minder iteraties nodig te hebben, terwijl voor de complexe toepassingen als stroming

in een SMRX reactor en andere poreuze media het gemiddeld gezien ongeveer 3 maal efficiënter is, hetgeen voor realistische simulaties significant is. In de tweede verfijning, worden rooster-Boltzmann simulaties bekeken die gebaseerd zijn op geneste computationele grids. Deze geneste grids zijn hiërarchisch opgebouwd uit verschillende subgrids die een ander resolutie kunnen hebben. De Boltzmann vergelijking voor een discrete verzameling van snelheden (continue tijd en ruimte) wordt numeriek opgelost en de verschillende subgrids worden consistent aan elkaar gekoppeld. Deze methode is gevalideerd op het Taylor-Vortex probleem en de eerste resultaten zijn positief. In de nabije toekomst willen wij deze techniek toepassen op een aantal veel complexere problemen.
In het laatste hoofdstuk zijn de transporteigenschappen van poreuze fibermedia bestudeerd. De doorlaatbaarheid van verschillende modellen van fibermedia is berekend als functie van de volumefractie en de resultaten zijn vergeleken met bestaande theoretische, numerieke en experimentele data. Voor de geordende media, namelijk SC en BCC configuraties is er een goede overeenstemming tussen de rooster-Boltzmann berekeningen en de beschikbare theoretische en numerieke data. De resultaten voor de doorlaatbaarheid van ongeordende fibermedia zijn ook eveneens in overeenstemming met de analytische oplossing van Jackson en James en de empirische Kozeny-Carman vergelijking. Over een vrij groot bereik van volumefracties blijkt de doorlaatbaarheid van 3D fibermedia exponentieel afhankelijk te zijn van de volumefractie.
Via dimensie-analyse is beredeneerd dat de gemiddelde afstand tussen de vezels de bepalende factor is voor de doorlaatbaarheid. Dit verband is bestudeerd voor de diverse fibermedia en verschaft inzicht in het exponentieel verband van de doorlaatbaarheid als functie van de volumefractie.
Tenslotte is de doorlaatbaarheid van fibermedia bestudeerd die geplaatst worden tussen twee vlakke platen (de zogenaamde *bounded* media). Ondanks het feit dat veel realistische fibermedia *bounded* zijn, zijn weinig theoretische oplossingen van dergelijke systemen in de literatuur te vinden. Voor zowel geordende als ongeordende fibermedia hebben wij de doorlaatbaarheid bepaald als functie van de afstand tussen de platen. In de limiet van kleine volumefracties zijn de resultaten goed in overeenstemming met de theorie van Tsay en Weinbaum. Door in de theoretische oplossing van Tsay en Weinbaum expliciet een afhankelijkheid op te nemen van de gemiddelde afstand (dominante factor van de doorlaatbaarheid) is een fenomenologische uitdrukking afgeleid die in een groter bereik van fibervolume fracties geldig is.

Nawoord

Het schrijven van het nawoord voor dit proefschrift ervaar ik als een moment van bezinning; een terugblik op wat er in de afgelopen decennium allemaal heeft plaatsgevonden. Inderdaad, een serie momenten van vallen en opstaan! Het is allemaal ongeveer 9 jaar geleden begonnen toen ik, nadat ik het VWO in Suriname had afgemaakt, in Nederland aankwam voor studie. Ik koos voor de studie informatica aan de Universiteit van Amsterdam. Vraag me niet waarom ik dat gedaan heb, want dat weet ik nog steeds niet. Waar ik inmiddels wel van overtuigd ben, is dat ik het vak natuurkunde veel leuker vind.

Nadat ik de propedeuse had afgerond ben ik in mijn tweede studiejaar wat vakken bij natuurkunde gaan volgen. Dit deed ik in de hoop om deze vakken later als vrije keuze op te nemen in mijn afstudeerplan. Aan het eind van het tweede studiejaar werd het pas echt moeilijk; ik moest toen een keuze maken uit de diverse specialisatierichtingen. Na een blik in de studiegids informatica was de afstudeerrichting voor mij al snel duidelijk, namelijk fysische informatica. Tijdens het inwinnen van nadere informatie bij de studieadviseur bleek dat die afstudeerrichting zoals in de studiegids vermeld, eigenlijk opgeheven zou worden. Aan mij werd verteld dat er wel iemand in de vakgroep bezig was met het opzetten van een soortgelijk afstudeerrichting. Ik zou kontakt moeten opnemen met de desbetreffende docent om de mogelijkheden verder te bespreken.

Ik heb toen een afspraak gemaakt met die docent en na ongeveer een half uur gesproken te hebben, begreep ik dat hij werkte aan computersimulaties van het macroscopisch gedrag van complexe natuurwetenschappelijke systemen op parallelle computers. Hij noemde het een multidisciplinair vakgebied dat zich bevindt tussen de informatica, natuurkunde en numerieke wiskunde. Zijn onderzoek bestond uit twee hoofdrichtingen, de een meer gericht op de informatica aspecten terwijl de ander een meer natuurwetenschappelijk karakter had. Velen onder u zullen dit vakgebied tegenwoordig kennen onder de naam computational science. Ik wilde mij meer richten op de natuurwetenschappen. Tijdens ons gesprek wees hij mij uitdrukkelijk op het feit dat het hiervoor handig zou zijn als ik een aantal vakken bij natuurkunde en bij numerieke wiskunde zou volgen. Dit was precies wat ik zocht en we hebben toen afgesproken om later nog eens *uitgebreid* met elkaar te praten, nadat ik de vereiste vakken (ongeveer anderhalf jaar studielast) achter de rug had.

Om een lang verhaal kort te maken...
We hebben toen inderdaad voor de tweede keer met elkaar gesproken en dit keer ging het om een afstudeerstage bij Estec in Noordwijk. Het onderwerp was pa-

rallellisatie van een klimaatmodel. Dit was mijn eerste kennismaking met het vakgebied vloeistofdynamica. Ik ben toen na een jaar afgestudeerd en een aantal weken voor mijn afstuderen had ik weer een gesprek met die docent. Dit keer spraken we over wat ik na mijn afstuderen wilde doen. Ik had al eerder aangegeven dat ik wetenschappelijk onderzoek ambieerde en bij het gesprek kwam de vraag naar voren of ik interesse had voor een promotie-onderzoek over vloeistofstromingen met de rooster-Boltzmann methode. Dat was volgens hem een veelbelovende methode om het macroscopisch gedrag van vloeistofstromingen zeer efficiënt op parallelle systemen na te bootsen. Ik hoefde niet lang na te denken! Het resultaat van wat hierna is gebeurd staat beschreven in dit proefschrift.
U zult het wel geraden hebben wie ik steeds met 'die docent' eigenlijk bedoeld heb. Peter, ik wil jou bij deze van harte bedanken voor het vertrouwen dat jij in mij hebt gesteld en de mogelijkheden die je mij hebt geboden voor het doen van promotieonderzoek in een multidisciplinair vakgebied als de Computational Science. Jouw frisse kijk op wat wetenschappelijk gezien interessant is en de vele adviezen stel ik bijzonder op prijs.
Een ander persoon die een zeer belangrijke rol heeft gespeeld bij dit onderzoek is Alfons Hoekstra. Van hem heb ik veel geleerd over uiteenlopende onderwerpen, variërend van het maken van nette plaatjes tot het redeneren over fysische systemen. Uitspraken als: 'gebruik grotere captions voor de figuren...', 'laten we even alles opnieuw op het bord schrijven', 'zo gaat het niet goed', 'Nou, nou, mag je dit wel zo zeggen...', 'zullen we vrijdag om 10.00 uur onze wekelijkse werkbespreking houden?', en vele anderen zullen mij lang bijblijven! Alfons, jouw kritische kijk op dingen en brede kennis was zeer nuttig bij de totstandkoming van dit proefschrift.
In this thesis there has been a strong cooperation with other groups. I would like to thank Antti Koponen for the very succesful cooperation. In fact it all started in a workshop where after having a few beers we realized that we could make fast progress if we would stay in touch with each other. I am not sure whether at that time this was due to our joint interest in beer or due to our scientific interest. After having email discussions for some time, we finally decided to cooperate more actively. I would also like to thank Antti's thesis advisors, Jussi Timonen and Marku Kataja for stimulating the cooperation.
Verder wil ik David Vidal, Huub Hoefsloot en Piet Iedema bij deze bedanken voor de goede samenwerking welke geresulteerd heeft in hoofdstuk 6 van dit proefschrift.
During the last year of the research I got the opportunity to visit the Los Alamos National Laboratory, one of the top research institutes with an active research program on the Lattice-Boltzmann method (the *mekka* of Lattice-Boltzmann). I am very thankfull to Wendy Soll and Shiyi Chen for their cooperation on the nested grid work. For me it was a very intriguing experience to visit the Los Alamos Laboratory. Unfortunately our cooperation was during the last period of my PhD project and the work is still in a preliminary stage. Hopefully this work can get more body in the future.
I would also like to thank David Clague. Our joint interest in fluid flow in fi-

brous media has resulted in much of the material presented in chapter 7.
Naast het wetenschappelijk onderzoek, is het vooral belangrijk om een werkplek te hebben waar je een goed gevoel bij hebt. Bij deze wil ik al mijn collega's en de afstudeerstudenten (in het bijzonder Robbel, Jaap, Jan, Martin, David Dubbeldam, David de Kanter, Jeroen, Diederik, Arjen, Roeland, Piero, Dick, Berry, Zeger, Frank, Ronald, Edwin, Judhi, Maria, Zhi-min, Artoli, Walter, Benno, Andy, Marcel Beemster, Joep, Robbert, Jan Wortelboer, Gert, Mashad en Wouter Haak) noemen. De wetenschappelijke discussies en vooral de borrels tijdens conferenties en de survivaltochten hebben de promotietijd bijzonder aangenaam gemaakt.
Een speciale woord van dank gaat uit naar Martin Bergman, David Dubbeldam, Arjen Schoneveld, Wouter Haak en Dinesh Bisai. Martin is in mijn oog een bijzonder persoon die eigenlijk op alles, zowel technisch, wiskundig als het sociale vlak, iets weet. Martin je bent een fijne kamergenoot. David, de conversaties die wij hebben gevoerd over muziek, wetenschap en andere zaken en de vele kopjes koffie, waren uiterst plezierig. Arjen, de gesprekken die wij over allerlei zaken hebben gevoerd waren heel stimulerend vooral in de mindere periodes van het promotieonderzoek. Wouter, voor jouw inspanningen aan het gridrefinement onderzoek, dat jij zijdelings even tussendoor hebt uitgevoerd, heb ik veel respect. Ik vind het jammer dat wij niet langer hebben samengewerkt. En, Dinesh, ik hoef niks te zeggen!
De altijd vriendelijke medewerkers van het secretariaat (Erik, Hugo, wijlen Ina, Jacqueline, Laura, Moniek, Virginie) en P&O (Joyce en Willem) wil ik graag bedanken voor hun bereidwilligheid om al mijn vragen (zelfs de stomme over de werking van het fax apparaat) te beantwoorden en voor de vriendelijke en grappige conversaties die wij altijd hebben mogen voeren.
Als laatste wil ik mijn familie, in het bijzonder mijn moeder, broer, zuster en zusje, en mijn oom Sieuw, tante Louise en kinderen, en al mijn andere familieleden, vrienden en kennissen (een opsomming zou dit nawoord gemakkelijk een aantal keer langer maken) van harte bedanken voor de bijdrage die ze op welke manier dan ook hebben geleverd.

Dit nawoord sluit ik af met het volgend gebed,

God, geef mij de sereniteit
Om dat wat ik niet kan veranderen te aanvaarden,
De moed om dat wat ik kan veranderen te veranderen,
En de wijsheid om het onderscheid te kunnen maken.

Uit: Mansukh Patel en John Jones, Oog in oog met het leven - van strijd naar vrijheid (samengesteld door Sally Langford en Andrew Wells)

Publications

1. D. Kandhai, A. Koponen, A. Hoekstra, M. Kataja, J. Timonen, and P. Sloot, 'Implementation Aspects of 3D Lattice-BGK: Boundaries, Accuracy and a New Fast Relaxation Method', *J. Comp. Phys.*, **150**, 482-501 (1999).

2. D. Kandhai, A. Koponen, A. Hoekstra, and P.M.A. Sloot, 'Iterative Momentum Relaxation for Fast LBM Simulations' *High-Performance Computing and Networking 1999* , **LNCS 1593**, Springer-Verlag, 311-319 (1999)

3. D. Kandhai, D. Dubbeldam, A. Hoekstra, and P. M. A. Sloot, 'Parallel Lattice-Boltzmann simulation of fluid flow in a centrifugal elutriation chamber', in High-Performance Computing and Networking (P. Sloot, M. Bubak, B. Hertzberger. eds.), no. 1401 in Lecture Notes in Computer Science, (Amsterdam, The Netherlands), pp. 173-182, Springer-Verslag, 1998. ISBN 3-540-64443-1.

4. D. Kandhai, A. Koponen, A. Hoekstra, M. Kataja, J. Timonen, and P. Sloot, 'Lattice-Boltzmann Hydrodynamics on Parallel Systems', *Comput. Phys. Commun.*, **111**, 14-26 (1998).

5. D. Kandhai, D.J.-E. Vidal, A.G. Hoekstra, H. Hoefsloot, P. Iedema, and P.M.A. Sloot, 'A Comparison between Lattice-Boltzmann and Finite-Element Simulations of Fluid Flow in Static Mixer Reactors', *Int. J. Mod. Phys. C*, 9 (8), 1123 (1998).

6. D. Kandhai, D. Vidal, A. Hoekstra, H. Hoefsloot, P. Iedema, and P. Sloot, 'Lattice-Boltzmann and Finite-Element Simulations of fluid flow in a SMRX Static Mixer', *Int. J. Num. Meth. Fluids*, In press.

7. A. Koponen, D. Kandhai, M. Kataja, and J. Timonen, 'Simulations of single-fluid flow in porous media', *Int. J. Mod. Phys. C*, 9 (8), (1998).

8. A. Koponen, D. Kandhai, E. Hellen, M. Alava, A. Hoekstra, M. Kataja, K. Niskanen, P. Sloot, and J. Timonen, 'Permeability of Three-Dimensional Random Fiber Webs', *Phys. Rev. Lett.*, **80**, 716-719 (1998).

9. D.S. Clague, D. Kandhai, R. Zhang, and P.M.A. Sloot, 'Hydraulic Permeability of (Un)Bounded Fibrous Media Using the Lattice-Boltzmann Method', *Phys. Rev. E*, Accepted.

10. D. Kandhai, W. Soll, S. Chen, A. Hoekstra, and P.Sloot, 'Finite-Difference Lattice-BGK Methods on Nested Grids', *Comp. Phys. Comm.*, Accepted.